



**STRUCTURAL RESPONSE OF THE SLOTTED WAVEGUIDE ANTENNA
STIFFENED STRUCTURE COMPONENTS UNDER COMPRESSION**

THESIS

Joseph W. Sabat Jr, Second Lieutenant, USAF

AFIT/GAE/ENY/10-M19

**DEPARTMENT OF THE AIR FORCE
AIR UNIVERSITY**

AIR FORCE INSTITUTE OF TECHNOLOGY

Wright-Patterson Air Force Base, Ohio

APPROVED FOR PUBLIC RELEASE; DISTRIBUTION UNLIMITED

The views expressed in this thesis are those of the author and do not reflect the official policy or position of the United States Air Force, Department of Defense, or the United States Government.

This material is declared a work of the U.S. Government and is not subject to copyright protection in the United States.

AFIT/GAE/ENY/10-M19

STRUCTURAL RESPONSE OF THE SLOTTED WAVEGUIDE ANTENNA STIFFENED
STRUCTURE COMPONENTS UNDER COMPRESSION

THESIS

Presented to the Faculty

Department of Aeronautics and Astronautics

Graduate School of Engineering and Management

Air Force Institute of Technology

Air University

Air Education and Training Command

In Partial Fulfillment of the Requirements for the
Degree of Master of Science in Aeronautical Engineering

Joseph W. Sabat Jr, B.S.

Second Lieutenant, USAF

March, 2010

APPROVED FOR PUBLIC RELEASE; DISTRIBUTION UNLIMITED

AFIT/GAE/ENY/10-M19

STRUCTURAL RESPONSE OF THE SLOTTED WAVEGUIDE ANTENNA STIFFENED
STRUCTURE COMPONENTS UNDER COMPRESSION

Joseph W. Sabat Jr, B.S.

Second Lieutenant, USAF

Approved:

Anthony Palazotto
Thesis Advisor

Date

Lt Col Eric Swenson
Committee Member

Date

Rashid Abu Al-Rub
Committee Member

Date

Abstract

The Slotted Waveguide Antenna Stiffened Structure (SWASS) is an aircraft system that can provide the capabilities of a stiffened panel skin structure and a slotted waveguide radar antenna simultaneously. The system made from carbon fiber reinforced polymers is designed around a 10 GHz radar frequency in the X-band range and uses a WR-90 waveguide as a baseline for design. The system is designed for integration into fuselage or wing sections of intelligence, surveillance, and reconnaissance (ISR) aircraft and would increase the system performance through the availability of increased area and decreased system weight. Elemental parts of the SWASS structure were tested in compression after preliminary testing was completed for material characterization of a resin reinforced plain woven carbon fiber fabric made from Grafil 34-700 fibers and a Tencate RS-36 resin with a resin mass ratio of 30%. Testing included finite element stress and strain field characterization of seven single slot configurations, and results showed the longitudinal 90° slot was the best structural slot by about 30% in terms of maximum von Mises stress. Single waveguides were tested in the non-slotted configuration and a configuration including a five longitudinal slot array in one waveguide wall. Finite element results were compared with experimental results and showed good comparisons in all areas. The slot array was determined to have a decrease in nonlinear limit load of 8% from the finite element simulations and 12% from the experimental results. All waveguides showed the characteristics of local wall buckling as the initial failure mechanism and had significant buckling features before ultimate material failure occurred. Nonlinear limit load values were only slightly lower than linear bifurcation values, by less than 1% for both the slotted and non-slotted configurations. The imperfections from laboratory preparation caused a drop in the predicted limit load by about 30% showing the need for extreme care in advanced composite construction. Overall, results proved meaningful and the degradation in compressive performance due to the slot array is acceptable and promising. Future research is encouraged in the form of material tailoring, panel integration, and system optimization among others.

Acknowledgements

I would like to thank anyone who helped in this thesis in any way. First, my advisor Dr. Palazotto helped tremendously and was always very patient in helping me understand the concepts. Dr. Abu Al-Rub helped very much with some of the Abaqus problems and the extra time he spent helping me is greatly appreciated. I would also like to thank Lt Col Swenson for taking the time and making the effort to be a part of my committee. Most importantly I would like to thank my friends and girlfriend for reminding me that there is more to life than a thesis and helping me to relax enough to not go crazy during the process. Ben, Mike, Mike, and Rob from the Linux lab helped to make the day to day more enjoyable and helped to share in the misery. Thanks to my parents and family for understanding when I didn't call for weeks on end and their constant support and love. Bill Kaval, Bill Baron, Jim Tuss, Brian Smyers, Todd Bussey, Richard Wiggins, Larry Mack, and everyone else from AFRL thank you for your help and guidance. 20 years of schooling culminating in this document...Enjoy.

Joseph W. Sabat Jr

Table of Contents

	Page
Abstract	iv
Acknowledgements	v
Nomenclature	ix
List of Tables	xi
List of Figures	xii
 I. Introduction	 1
1.1 Motivation for Research	2
1.2 Overview of SWASS Concept	3
1.3 History of SWASS Research	4
1.4 History of CLAS	5
1.4.1 SAR	5
1.4.2 ISIS	7
1.4.3 Hawkeye Embedded Antenna	8
1.4.4 MUSTRAP	8
1.4.5 Microstrip Embedded Antenna	9
1.5 Current Aircraft Radar	11
1.6 Multifunctional Aircraft Components	12
1.7 Waveguide Theory Overview	14
1.8 Aircraft Structures	18
1.9 Previous Work in CFRP Compression	19
1.10 Research Approach	20
1.11 Chapter Outline	21

	Page
II. Theory	23
2.1 Instability Analysis	23
2.1.1 Linear Bifurcation Analysis by the Lanczos Method	23
2.1.2 Nonlinear Limit Load Calculations by the Riks Technique	27
2.2 Element Theory	30
2.3 Overview of Abaqus FE Model	31
2.4 Mesh Refinement for Mesh Independence	36
2.5 Riks Increment and Imperfection Refinement	40
2.6 Loading and Boundary Conditions	42
2.7 Slot Characterization	45
2.8 Processor Details	49
III. Experimental Setup	50
3.1 Determination of Carbon Fiber Material Properties	50
3.1.1 Specimen Processing Details for Compression Tests	52
3.1.2 Test Setup for Compression Tests	55
3.1.3 Compression Test Results	58
3.1.4 Specimen Processing Details for Shear Tests	61
3.1.5 Shear Test Setup	63
3.1.6 Shear Test Results	65
3.1.7 Material Property Data	67
3.2 Waveguide Specimen Preparation	70
3.2.1 Description of Waveguide Test Article	70
3.2.2 Waveguide Layup and Machining	70
3.2.3 Strain Gages for Waveguides	74
3.2.4 Waveguide Compression Test Setup	76

	Page
IV. Results and Discussion	79
4.1 Single Slot Finite Element Results	79
4.2 Linear Bifurcation Results	87
4.2.1 Non-Slotted Waveguide Bifurcation	87
4.2.2 Slotted Waveguide Bifurcation	88
4.3 Nonlinear Instability Results	94
4.3.1 Non-Slotted Waveguide Nonlinear Instability Results .	94
4.3.2 Slotted Waveguide Nonlinear Instability Results	98
4.4 Experimental Results	105
4.5 Summary of Results	118
V. Conclusions	119
5.1 Conclusions	119
5.2 Recommendations and Suggestions for Future Research	121
Appendices	124
Appendix A. Finite Element Model Creation and Analysis	124
Appendix B. D3410 Compression Specimen Failure Images	137
Appendix C. D7078 Shear Specimen Failure Images	138
Appendix D. Experimental Waveguide Raw Strain Gage Data	139
Appendix E. Experimental Waveguide Failure Images	144
Bibliography	148
Vita	151

Nomenclature

Symbols

R	Radar range – Pg. 2
P_s	Transmitter power
A	Area of antenna
P_e	Receiver power
P_{cr}	Critical buckling load
E	Modulus of elasticity
I	Moment of inertia
L_{eff}	Effective length
D	Plate stiffness
b	Plate width
t	Plate thickness
\mathbf{K}	Stiffness matrix
\mathbf{M}	Mass matrix
q	Displacement
$F(q)$	Equilibrium equations
l	Arc length
A	Amplifier gain
V_O	Output voltage
V_{Ex}	Excitation voltage
k	Gage factor

Greek

σ	Scattering coefficient, stress
λ	Wavelength, eigenvalue, load proportionality factor
λ_g	Waveguide wavelength
ν	Poisson's ratio

ϕ	Eigenvector
Δ	Incremental change
ϵ	Strain
τ	Shear stress
γ	Shear strain

Abbreviations

AFIT	Air Force Institute of Technology
AFRL	Air Force Research Laboratory
ASTM	American Society for Testing and Materials
AWACS	Airborne Warning and Control System
CFRP	Carbon Fiber Reinforced Plastics
CLAS	Conformal Load-Bearing Antenna Structure
CNI	Communications, Navigation, and Identification
DARPA	Defense Advanced Research Projects Agency
ERS	European Remote Sensing
FIRST	Facility for Innovative Research in Structures Technology
ISIS	Integrated Sensor Is Structure
ISR	Intelligence, Surveillance, and Reconnaissance
MUSTRAP	Multi Structural Aperture Program
NASA	National Aeronautics and Space Administration
RF	Radio Frequency
SAR	Synthetic Aperture Radar
SATCOM	Satellite Communication
SWASS	Slotted Waveguide Antenna Stiffened Structure
UAS	Unmanned Aerial System

List of Tables

Table		Page
1.	Shape Functions for Eight Noded Isoparametric Hexahedron Element	30
2.	Critical Values for Four Levels of Mesh Refinement	38
3.	Riks Refinement Study Data	40
4.	Riks Imperfection Convergence Study Data	42
5.	Compression Specimen Gage Section Dimensions Before Testing . . .	54
6.	Compression Test Results and Averages Used for FE Material Properties	60
7.	Shear Test Results and Averages Used for FE Material Properties . .	68
8.	Final Carbon Fiber Reinforced Polymer Material Properties at Waveguide Fiber Orientation	68
9.	Waveguide Specimen Cross Section Dimensions (All Dimensions in Inches)[mm]	72
10.	Results from Slot Configuration Tests	80
11.	Non-Slotted Waveguide Bifurcation Results	88
12.	Slotted Waveguide Bifurcation Results	89
13.	Plain Waveguide Riks Results	97
14.	Slotted Waveguide Riks Results	101
15.	Results from Waveguide Laboratory Tests	105

List of Figures

Figure		Page
1.	Typical Slotted Waveguide and Hat Stiffened Panel	3
2.	SWASS Panel Model with Longitudinal Broad Wall Slot Array	4
3.	Close Up of Metalized CFRP Waveguide Used in ERS-1	6
4.	SAR Array for ENVISAT	7
5.	ERS-2 Satellite with SAR Array Deployed	7
6.	Bathtub Type CLAS Arrangement	9
7.	NASA F-18 Fitted with MUSTRAP Vertical Tail Cap Antenna	9
8.	E-3 AWACS Aircraft with Large Radome Structure	11
9.	Saab 2000 Aircraft with Airborne Early Warning Radar System	12
10.	NASA Boeing 737 with Radar System Exposed in Nose Cone Radome	12
11.	Schematic of Typical Slotted Waveguide	14
12.	Waveguide with Visual Representation of Radar Pattern from Slots on Top Face of Waveguide	15
13.	Current Field of RF Energy Inside Waveguide (Top View)	16
14.	Slot Spacing Parameters for a Slotted Waveguide	17
15.	Metalized CFRP Slotted Waveguide Array from ERS-1	17
16.	Typical Top Hat Stiffened Panel for Aircraft Structure	18
17.	Bead Stiffened Panel for Use in Fuselage of Mid-Sized Transport	19
18.	Representative Comparison of Bifurcation analysis with Limit Load Calculation	24
19.	Visualization of Arc Length Parameter Used for Incrementation in Riks Analysis	29
20.	Eight Noded Continuum Shell Element	30
21.	Finite Element Model Assembly Used for Waveguide Analysis	32
22.	Principal Fiber Orientations of Fabric and FE Model Input Directions	33
23.	Problematic Square Corner with Curved Transition Solution	34

Figure		Page
24.	Layup Detail Showing Five Integration Point Locations	35
25.	Spurious Hourglass Mode from Course Mesh of Linear Elements . . .	36
26.	Path Used for Extraction of von Mises Stress Values for Mesh Refinement	37
27.	Three Meshes on Undeformed Shape of Slotted Waveguide (Global Seed values 0.044, 0.022, and 0.011 Top to Bottom)	38
28.	Von Mises Stress Plot along Path of Three Meshes (Global Seed values 0.044, 0.022, and 0.011 in)	39
29.	Von Mises Stress Contour Plot of Three Meshes (Global Seed values 0.044, 0.022, and 0.011 from Top to Bottom)	39
30.	Riks Increment Refinement Plots Showing Arc Length Increments of 10, 100, and 1E6	41
31.	Loads and Boundary Conditions Applied Directly to End Surface in Early Attempts	43
32.	Loads and Boundary Conditions Applied to Steel Plates in Intermediate Attempts	44
33.	Potted Waveguide Specimen	45
34.	Seven Slot Configurations and Representative Figures	47
35.	Longitudinal Slot with Interacting Stress Field and Boundary Conditions on Top and Independent Condition on Bottom	48
36.	Compression Fixture Attached to MTS Machine with Specimen Placed and Preloaded	52
37.	Compression Specimen for ASTM Test D3410 with White Tabbings Material	53
38.	Resin Paper Cut to Size for Shear Specimen Ply Debulking	54
39.	Debulked Resin/Fabric Sheets for Shear Specimen Layup	55
40.	Compression Specimen for ASTM Test D3410 with Strain Gages . . .	56
41.	Compression Fixture Attached to MTS Machine	57
42.	Schematic of Three Wire Strain Gage Setup	58
43.	Compression Curves for Five Specimens from ASTM D3410	59

Figure		Page
44.	1000-3000 $\mu\epsilon$ Strain Range Compression Curves for Four Specimens with Linear Fits	61
45.	Shear Specimen Drawing for ASTM Test D7078	63
46.	Shear Specimen Drawing with Perpendicular Strain Gages at Center Location	64
47.	Shear Fixture Parts Displayed	65
48.	Empty Shear Fixture Loaded into Test Frame	66
49.	Shear Specimen Loaded into One Half of the Shear Fixture with White Polymer Spacers	67
50.	Raw Shear Test Stress Strain Data	68
51.	2000-6000 $\mu\epsilon$ Strain Range Stress Strain Curves for Five Shear Specimens with Linear Fits	69
52.	Representative Figure of Zig-Zag Shear Failure from Shear Tests . . .	69
53.	Mechanical Drawing of Slotted Waveguide with Potting Material . . .	71
54.	Aluminum Mandrel with Two Layers of Woven Carbon Fiber Tubing Stretched Over Top	73
55.	Fabric Wrapped Mandrel on Resin Sheet Ready for Wrapping	74
56.	Fabric and Resin Wrapped Mandrel Before Outer Mandrels are Applied	75
57.	Full Fabric, Resin, and Mandrel Assembly	76
58.	Strain Gage Locations for Eight Waveguide Specimens	77
59.	Waveguide Compression Test Setup	78
60.	Seven Slot Configurations and Representative Figures	82
61.	Von Mises Stress Field and Overall Strain Magnitude Field for 0° Slot	83
62.	Von Mises Stress Field and Overall Strain Magnitude Field for 15° Slot	83
63.	Von Mises Stress Field and Overall Strain Magnitude Field for 30° Slot	84
64.	Von Mises Stress Field and Overall Strain Magnitude Field for 45° Slot	84
65.	Von Mises Stress Field and Overall Strain Magnitude Field for 90° Slot	85
66.	Von Mises Stress Field and Overall Strain Magnitude Field for H Slot on Broad Wall	85

Figure		Page
67.	Von Mises Stress Field and Overall Strain Magnitude Field for H Sloton Narrow Wall	86
68.	Stress vs Slot Angle Plot Showing Failure Limits and Slot Tip Stresses for 1000lb (4.45 kN) Load	86
69.	Bifurcation Eigenvectors for the First Five Eigenmodes of the Non-Slotted Waveguide	91
70.	Comparison of Single Broad Wall Plate Buckling Mode with Plain Waveguide	92
71.	Buckling Eigenvectors for the First Five Eigenmodes of the Slotted Waveguide	93
72.	Node Location for Extraction of Stress and Displacement Data	95
73.	Nonlinear Riks Stress Displacement Curve for Plain Waveguide with Imperfection	96
74.	Von Mises Contour Plot on Deformed Waveguide Before Buckling (Load=102 lb[453 N])	97
75.	Von Mises Contour Plot on Deformed Waveguide at Point of Buckling (Load=930 lb[4136 N])	98
76.	Von Mises Contour Plot on Deformed Waveguide After Significant Buckling (Load=2010 lb[8940 N])	99
77.	Out of Plane Displacement Curves Showing Large Deformations During Instability	100
78.	Nonlinear Riks Stress Displacement Curve for Slotted Waveguide . . .	101
79.	Von Mises Contour Plot on Deformed Waveguide Before Buckling (Load=102 lb[453 N])	102
80.	Von Mises Contour Plot on Deformed Waveguide at Point of Buckling (Load=875 lb[3892 N])	103
81.	Von Mises Contour Plot on Deformed Waveguide After Significant Buckling (Load=2000 lb[8896 N])	103
82.	Nonlinear Riks Analysis Curves for Plain and Slotted Waveguide . . .	104
83.	Plain Waveguide in Compression Fixture Showing Wall Buckling . . .	106

Figure		Page
84.	Plain Waveguide Close Up Showing Out of Plane Displacement of Broad Wall	107
85.	Slotted Waveguide in Compression Fixture with Slot Wall Buckling .	108
86.	Two Slot Close Up Showing Alternating Concavity of Buckling	109
87.	Close Up of Single Gaged Slot with Concave Buckling	110
88.	Strain and Load Data from Specimen Seven	112
89.	Strain and Load Data from Specimen Three	113
90.	Strain and Load Data from Specimen Five	114
91.	Strain and Load Data from Specimen Six	115
92.	Lab Photo of Specimen Six Showing Out of Plane Wall Displacement	116
93.	Shear Plane Side Wall Failure and Transverse Broad Wall Failure Cracks on Specimen Three	117
94.	Waveguide Model with Rounded Edges Highlighted	125
95.	Close Up of Datum Plane Positioning	126
96.	Close Up of Face Partition for Sweep Path	126
97.	Datum Coordinate Systems for Layup Sections	127
98.	Detail Showing Sweep Path of Corner Cells	131
99.	Node Selection for XY Data	135
100.	Compression Specimen Failure Images	137
101.	Shear Specimen Failure Images	138
102.	Strain Gage Locations for Eight Waveguide Specimens	139
103.	Raw Strain Gage Data for Specimen 1	140
104.	Raw Strain Gage Data for Specimen 3	140
105.	Raw Strain Gage Data for Specimen 4	141
106.	Raw Strain Gage Data for Specimen 5	141
107.	Raw Strain Gage Data for Specimen 6	142
108.	Raw Strain Gage Data for Specimen 7	142
109.	Raw Strain Gage Data for Specimen 8	143

Figure		Page
110.	Specimen 1 Waveguide Failure Image	144
111.	Specimen 3 Waveguide Failure Image	145
112.	Specimen 4 Waveguide Failure Image	145
113.	Specimen 5 Waveguide Failure Image	146
114.	Specimen 6 Waveguide Failure Image	146
115.	Specimen 7 Waveguide Failure Image	147
116.	Specimen 8 Waveguide Failure Image	147

STRUCTURAL RESPONSE OF THE SLOTTED WAVEGUIDE ANTENNA STIFFENED STRUCTURE COMPONENTS UNDER COMPRESSION

I. Introduction

Throughout history, warfare has been shaped by advances in technology. From the development of the rifle to the advancement of current fighter aircraft, technology has always played a role in war fighting strategy and tactics. The current aerospace market is on the cutting edge of technology development and within aerospace technology, there has been some focus on multifunctional aircraft components. One such concept is the combined functionality of an aircraft skin for both structural integrity and a radar antenna. In general this concept is referred to as conformal load-bearing antenna structure (CLAS). A specific use of CLAS has been proposed by the Air Force Research Laboratories (AFRL) with a focus on incorporating the top hat or square tube shaped stiffeners of a typical aircraft skin panel into use as radar waveguides. This concept is called the Slotted Waveguide Antenna Stiffened Structure (SWASS). The objective of this thesis is to consider compressive loading, a possible scenario, on the utilized waveguide in a structural situation. The investigation of carbon fiber slotted waveguide members will include stress/strain field characterization of seven slot configurations and finite element/experimental comparison of slotted and unslotted waveguide members.

1.1 Motivation for Research

Secretary of Defense Robert Gates expressed a need for persistent intelligence, surveillance, and reconnaissance (ISR) in his speech to Congress in April, 2009 when stating the direction of the current defense budget[1]. The development of new and improved systems for ISR is crucial and SWASS can provide a significant benefit to current radar systems. Multiple types of airborne radar systems are available and employed today, but almost all of the systems require the radar components to be stored inside of a radome feature to give the system structural capacity and less of an aerodynamic signature. The use of an array of slotted waveguides as the radar antenna is one common system. The unique features of this system is that it has high efficiency and the ability to be compacted into a smaller area[2]. With possible integration into the skin structure, the system could eliminate the need for a radome housing and allow for significant weight savings on the aircraft. There is also the possibility for significantly increased radar performance due to a larger antenna size. From the radar range equation [Eq. (1)], doubling the frontal area of the antenna (A) would produce a 41% increase in range (R) as opposed to a doubling of the power of the system (P_s) which would only increase range by 19%.

$$R = \sqrt[4]{\frac{P_s \pi^2 A^2 \sigma}{4\pi^3 P_e \lambda^2}} \quad (1)$$

The United States will always need high power radar systems for monitoring battlefield situations and surveillance. The systems at work right now such as the Airborne Warning and Control System (AWACS) aircraft do the job, but there is room for improvement. By integrating the large radar waveguide array into the structure of the aircraft, one can save

significant drag and weight penalties which can help the aircraft to perform better and have longer endurance. With these greater performance measures, persistent ISR is more attainable and more economical to achieve for the US government and military. The SWASS concept can greatly improve the performance of current systems or be designed around in future systems for the next generation of high power radar capabilities.

1.2 Overview of SWASS Concept

The basis of the SWASS concept is the incorporation of radar systems into the stiffened skin of a typical aircraft structure. Waveguides typically work by directing radar energy down the length of the tube and slots cut in one side of the tube allow that energy to escape. The selected slot pattern will direct the energy in a certain configuration. The waveguide members strongly resemble the typical top hat stiffeners of a stiffened panel and so the natural progression would be the combination of the waveguide and a hat stiffened panel (Figure 1) into a fully integrated SWASS concept of a slotted waveguide stiffened panel (Figure 2).

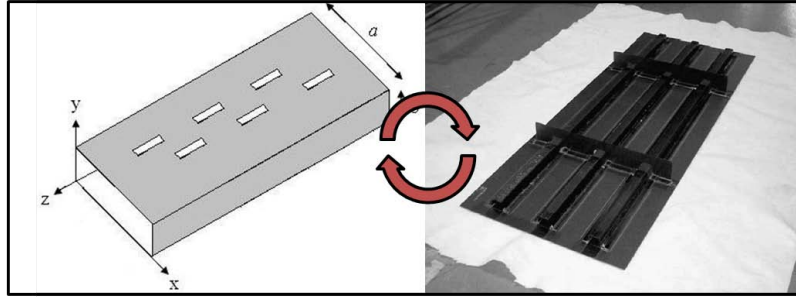


Figure 1 Typical Slotted Waveguide and Hat Stiffened Panel

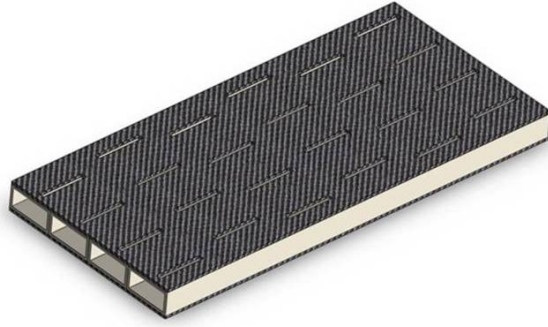


Figure 2 SWASS Panel Model with Longitudinal Broad Wall Slot Array

1.3 History of SWASS Research

To date, no structural research has been performed on SWASS components. This is due to the project being in its infant stages. Callus describes in detail the history of the SWASS project and the overview of his radio frequency research completed while an exchange fellow at the Air Vehicles Directorate, AFRL[3]. Some of the electrical characteristic studies that were completed include the characterization of slot shapes, sizes, and orientations as well as studies into the effect of different waveguide lining materials as they pertain to insertion loss and the radar energy propagation inside the tube. A detailed plan was given for introduction into the Aerosonde Unmanned Aerial System (UAS) and a mechanical test plan was also proposed[3]. The mechanical test plan included characterization of the unslotted waveguide as a baseline, the effect of different single slots in that waveguide and the axial compression of a slotted waveguide panel array similar to Figure 2. This thesis will complete the single slot characterization as well as an added step of multi-slotted single waveguide performance for a more detailed elemental analysis. This elemental data can then be compared to future research in the panel configuration.

1.4 History of CLAS

Some research has been conducted in the area of CLAS systems and some working antennas have been deployed. The only significant application of a structural antenna utilizing slotted waveguides is the Synthetic Aperture Radar (SAR) antenna developed by Ericsson and Dornier[4]. The SAR made from carbon fiber reinforced plastics (CFRP) was flown on three European imaging satellites and proved successful beyond the goals. Due to the nature of the satellite mission in space, the antenna did not see any significant structural loads beyond its own weight and vibrations during launch when it was in a folded configuration for smaller storage. Although these may not be as strong as aerodynamic loads, this does provide a platform of feasibility for the SWASS concept. Other CLAS programs that have been reported include Integrated Sensor Is Structure (ISIS) by the Defense Advanced Research Projects Agency (DARPA), an embedded antenna for the Navy E-2D Advanced Hawkeye aircraft by Northrop Grumman, the Multi Structural Aperture Program (MUSTRAP) by AFRL, and an integrated microstrip antenna in CFRP.

1.4.1 SAR. The SAR system was developed for the European Space Agency as part of European Remote Sensing (ERS) satellite number one (ERS-1). This satellite was launched in 1991 with a mission of collecting earth environmental data to include ocean temperatures and wind speeds[5]. The SAR radar system was developed out of CFRP in order to save weight for the launch of the satellite, but it was also made to hold its own weight while in a fully deployed flight configuration. There are some additional truss members required, but the overall panel is 10 meters x 1 meter[2]. This large panel is comprised of five smaller panels of 2m x 1m size. The thin walls and overall light weight

of the CFRP made this a very desirable configuration for weight savings and even with a metalization of the lining for better radio frequency (RF) performance, the entire panel had a final mass of only 7.75kg[2]. Figure 3 shows a close up of the metalized CFRP waveguide used for the ERS-1 array.

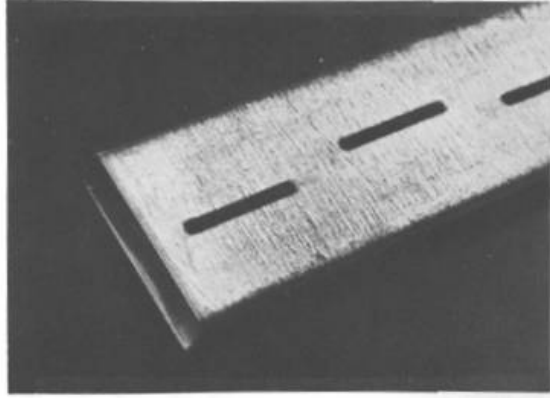


Figure 3 Close Up of Metalized CFRP Waveguide Used in ERS-1

This array was put through a series of mechanical tests and it was shown that all criteria were met while the overall cost of manufacturing was comparable to an aluminum array. Results for mechanical tests were not reported, but the requirements for launch and space flight were met. The weight savings were approximately 40% even with the metallization[6].

An even more advanced version of the SAR was also created for the successor to the ERS satellites, known as ENVISAT. This array was again made from CFRP and had a size of 1.3m x 10m in the fully deployed position. Figure 4 shows the full array in the lab while Figure 5 shows the full ERS-2 satellite with the attached SAR antenna. The success of these satellites has been greater than expected and the original ERS-1 lasted for almost nine years before a computer failure ended its operation while the ERS-2 launched in 1995 is still

continuing its orbit and providing clear and meaningful images. ENVISAT was launched in 2002 and is equipped with more advanced instruments as well as the advanced SAR to replace ERS-2 when it is no longer in service.

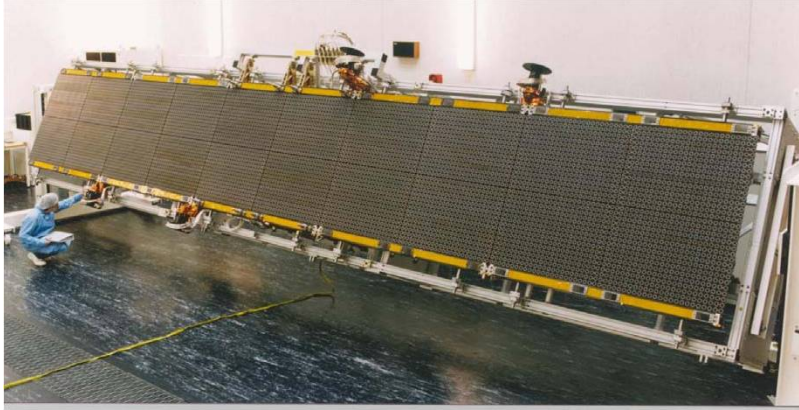


Figure 4 SAR Array for ENVISAT

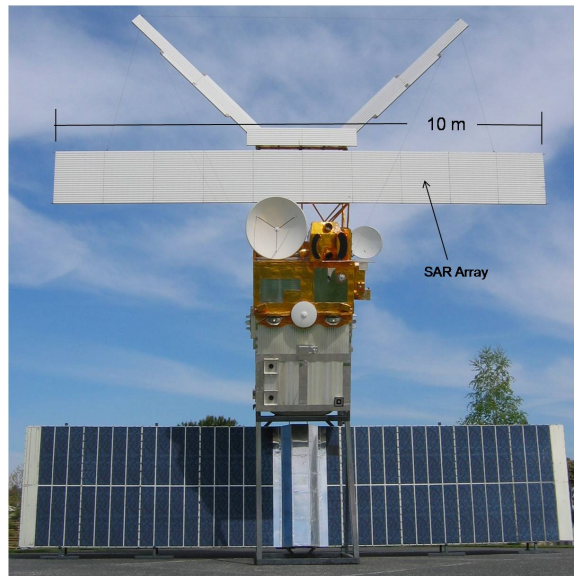


Figure 5 ERS-2 Satellite with SAR Array Deployed

1.4.2 ISIS. One other CLAS program is the ISIS program being researched by DARPA. Since the program is most likely classified in nature there is not much information available, but DARPA describes the project as such, “The ISIS program will develop the

technologies that enable extremely large lightweight phased-array radar antennas to be integrated into an airship platform.”[7]. This is clearly a CLAS concept but no further information is available.

1.4.3 Hawkeye Embedded Antenna. A news release from Northrop Grumman details a major breakthrough in technology allowing for the use of an embedded antenna for the Navy E-2D Hawkeye that could replace the current SATCOM antennas. The details are left out, but the article describes this as the, “...most significant progress to date in developing cost-effective ways to embed antennas in the load-bearing, composite structures of next-generation aircraft and ships”[8]. It is not known whether implementation of the system ever occurred.

1.4.4 MUSTRAP. Some early CLAS research by the Australian Defense Science and Technology Organisation (DSTO) showed a sandwich type CLAS concept that used a microstrip coil radiating element housed inside of a dielectric material[9]. This would then be integrated into the aircraft using a sort of bathtub structure to keep the antenna inside of the aircraft skin surface to avoid any unnecessary drag and the bathtub structure would have a component layer built in to carry the structural loads. A similar structure was used for the MUSTRAP program through AFRL as well as a vertical tail cap antenna with unknown construction. The sandwich panel as seen in Figure 6 shows the typical bathtub arrangement. Although the panel passed all structural tests, it was never flight tested. A similar system was developed and deployed by Ball Aerospace for use on ground vehicles called the Silhouette system[10]. This system does not seem to carry any structural loads however since it is fixed to the vehicle by some structural connection and not integrated.

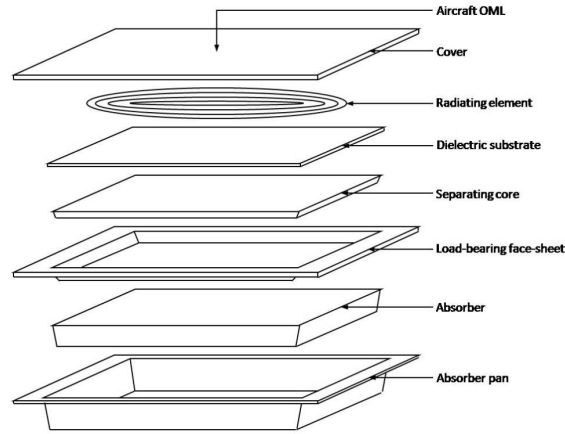


Figure 6 Bathtub Type CLAS Arrangement

The vertical tail cap was another structurally embedded antenna of the MUSTRAP program that was placed on the tip of the vertical tail of a NASA F-18. The antenna increased radar performance by 15 to 25 dB as compared to the original antenna, mostly due to the fact that the CFRP tail acted as an extra conductor and greatly increased the size of the antenna[9]. Figure 7 shows the tail cap antenna being fixtured and during a flight test. The cap successfully completed the flight test but no detailed structural information or implementation data was available.

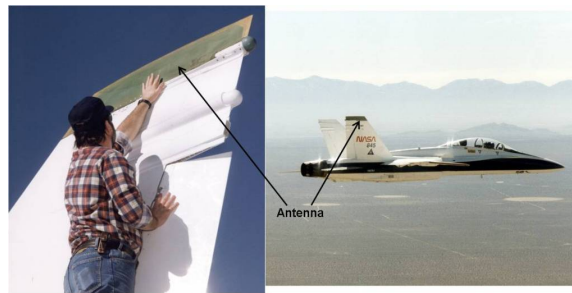


Figure 7 NASA F-18 Fitted with MUSTRAP Vertical Tail Cap Antenna

1.4.5 Microstrip Embedded Antenna. Yao and Qiu describe research into a microstrip antenna array that is embedded into a carbon fiber plate structure[11]. This

concept utilizes a three dimensional woven carbon fiber fabric and integrates the microstrip antenna by weaving it into the fibers. This provides some benefits in the fact that the antenna has incredibly low volume and so can be almost seamlessly integrated into any current woven structure[11]. The antenna was successfully integrated into a CFRP panel and the RF characteristics were measured. The performance compared reasonably well with traditional microstrip antennas. The most successful part of this research was the fact that the copper wires for the antenna were woven into the fabric which allows for a much higher damage tolerant panel since there are no interfaces between sensors and structural fibers for easy damage sites[11]. This configuration could be integrated into almost any CFRP wingskin with a three dimensional weave construction.

Although some of these CLAS examples perform similar functions to SWASS, and the SAR antenna is of similar construction, no CLAS concept has been tested and built that uses slotted waveguides and carries significant structural loads in an aircraft such as the SWASS project aims to. It is possible that some newer applications that do not have published details could have accomplished this, such as the communications, navigation, and identification (CNI) integrated body aperture for the F-35, but this is purely speculation since no external antennas are visible[12]. Again it will be the goal of this thesis to perform compression tests in both FE and lab settings of CFRP waveguides of the WR-90 configuration to determine the buckling and limit load performance as well as single slot stress/strain field characterization.

1.5 Current Aircraft Radar

Current high power radar systems are mounted on the exterior of an aircraft by some supporting structure and a radome housing. Probably the most famous of these aircraft is the AWACS shown in Figure 8. The circular structure on the top of the aircraft is the radome that houses the radar systems. One can imagine the increase in aerodynamic drag that such a structure imposes. Since the radome rotates to steer the radar energy, it may not be the best option for a CLAS concept. Other aircraft house stationary radar antennas outside of the normal fuselage lines, such as the Saab 2000 shown in Figure 9 that is used by Sweden and other countries, where the radar energy is steered electronically. It is not a stretch of the imagination to see this structure being integrated as part of the fuselage skin and being able to carry the structural loads for a CLAS.



Figure 8 E-3 AWACS Aircraft with Large Radome Structure

More common on aircraft that do not require a high performance radar system is to have the nose of the aircraft be the radome. Figure 10 shows an open nose cone with the radar system exposed from a NASA Boeing 737. The radar system is a planar array of slotted waveguides arranged in a circular plane. The challenge now becomes the integration of these components into the structure to serve multiple functions.



Figure 9 Saab 2000 Aircraft with Airborne Early Warning Radar System

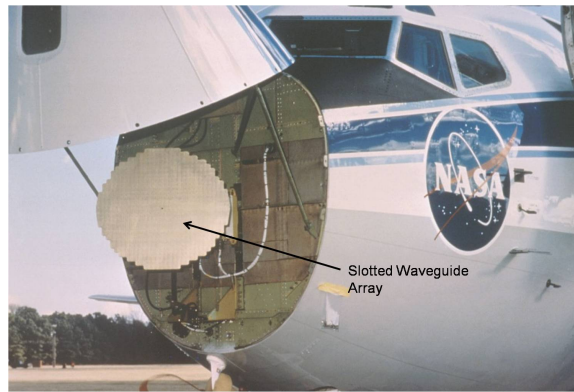


Figure 10 NASA Boeing 737 with Radar System Exposed in Nose Cone Radome

1.6 *Multifunctional Aircraft Components*

The idea of using aircraft components for multiple purposes is not a new idea, but one that is just beginning to take root. Typical aircraft have separate systems designed specifically to perform its own function to include structure, electrical wiring, propulsion, fuel, etc. This approach greatly reduces complexity and also allows for quick troubleshooting since each system has a specific purpose. The advantage of weight savings comes with multifunctional components which can increase aircraft performance and energy efficiency. This may become more important in the future as the world's petroleum reserves become more depleted and efficiency becomes of greater concern. In fact studies have shown that a

decrease in one unit of weight on an aircraft can lead to a subsequent decrease of 2 extra units of weight in the support structures and mechanical drive systems[6]. Some multifunctional systems that are currently being researched or implemented include structural health monitoring, shape control, battery structures and CLAS. Each of these take some form of the structure of the aircraft and incorporate a different system into the structure. Hayward et al. describes the embedding of ultrasonic sensors into a CFRP panel for use as a structural health monitoring system and describes some of the traditional complexities as the integration of the wiring to communicate with the sensors[13]. Shaikh takes the structural health monitoring one step further and successfully creates coated carbon fibers that can monitor structural health rather than embedding sensors[14]. The direction of multifunctional components will continue to become more integrated and less intrusive in the embedded structure. Thomas et al. provides research data into three different types of structural power systems such as structural batteries, structural consumed fuel, and solar aircraft skins and how they can affect small UAS flight endurance[15]. Structural combination with functional systems seems to be the typical direction as all materials in the aircraft could theoretically hold at least some small structural loads. If the system could be made out of advanced aircraft composites such as carbon fiber, then the potential for structural integration increases due to the tailorable nature of CFRP construction as described earlier and shown in Uozumi and Kito[16]. This is the question that is raised for SWASS; can slotted waveguide arrays be constructed from CFRP and still perform both structural and RF functions successfully? The focus of all SWASS research including this thesis will be to answer this question and prove the concept feasibility.

1.7 Waveguide Theory Overview

Slotted waveguides are one of many types of radio frequency RF antennas used to direct and amplify signals. These include traditional parabolic dish antennas, microstrip antennas, omnidirectional antennas, and of course slotted waveguides[17]. The advantages of slotted waveguides are simplicity, efficiency, reliability, and light weight[18]. A representative figure of a slotted waveguide is shown in Figure 11.

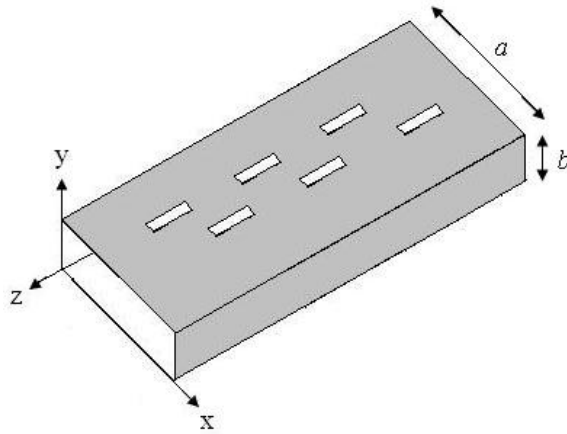


Figure 11 Schematic of Typical Slotted Waveguide

This waveguide contains radar energy that would be fed from one open end of the waveguide or from a hole in the bottom side (x-z plane). The slots are cut in only one face to allow for interruption of the electrical current inside the waveguide and the RF energy to escape in a pattern that is determined by the slots. The RF field inside the waveguide is shown in Figure 13. In order to agitate this field to produce a protruding radar energy lobe, a slot must be cut in the face of the waveguide. This slot cannot be symmetric about the longitudinal centerline of the waveguide since the RF field is symmetric about this line. A symmetric slot would allow for all energy to be canceled across the centerline and no protruding lobes would be produced. This is the reason that the slots are created offset

from the centerline as shown in Fig. 11 and the alternating nature across the centerline allows for additive interference between slots and a stronger main lobe. The typical radar pattern will include one large lobe of radar energy protruding perpendicular to the slot face with some side lobes which are undesirable but not feasible to eliminate (see Figure 12). A resonant waveguide with longitudinal slots will not minimize side lobes, but gives the best overall performance based on the power consumption and so this configuration will be used in the structural testing[18]. The slot spacing off the centerline and in the longitudinal direction is based on the design frequency of the waveguide. The design frequency for this project is 10 GHz, which is the center of the X-band radar range. This corresponds with a traditional WR-90 waveguide, which dictates the inner dimensions of the waveguide cross section. The standard WR-90 inner dimensions are 0.4"(0.010m) x 0.9"(0.023m) which will be the nominal dimensions of the waveguides tested in this thesis. The slot spacings will be according to Figure 14 with an end fed arrangement.

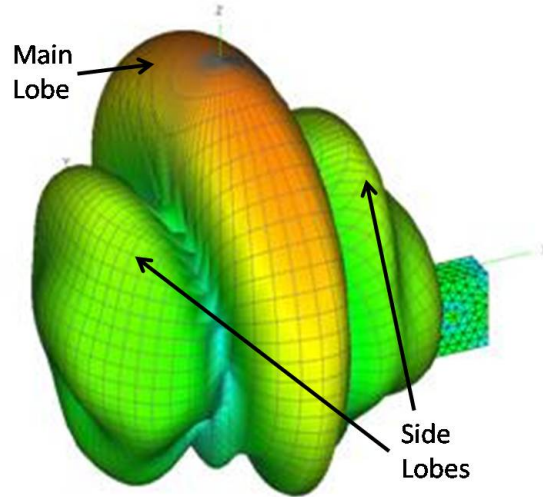


Figure 12 Waveguide with Visual Representation of Radar Pattern from Slots on Top Face of Waveguide

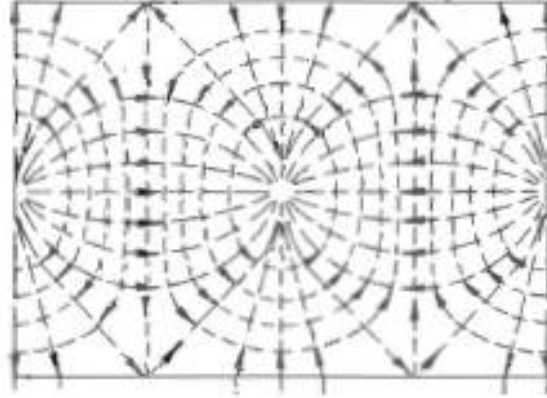


Figure 13 Current Field of RF Energy Inside Waveguide (Top View)[18]

To form a full antenna these waveguides are configured in a parallel arrangement to form a planar array with slots all facing the same direction (see Figure 15). Then this plane can be shaped in almost any configuration only limited by the required radar signature and the geometric space available. Integration into the structure allows for much greater space available as opposed to a housing inside the aircraft where space is limited or a separate structure outside the aircraft which increases aerodynamic drag.

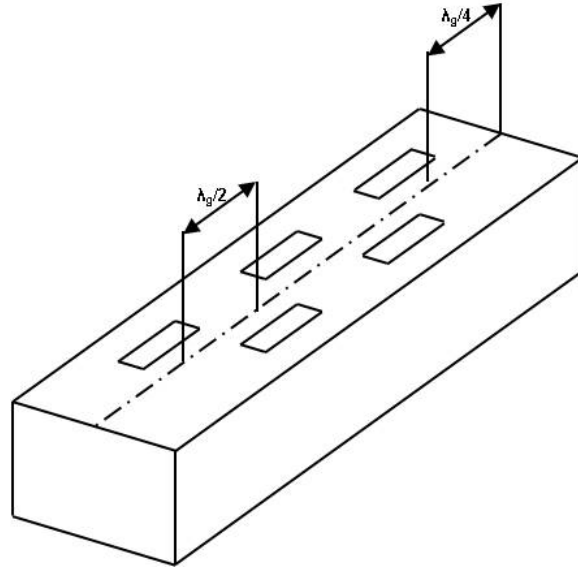


Figure 14 Slot Spacing Parameters for a Slotted Waveguide[18]

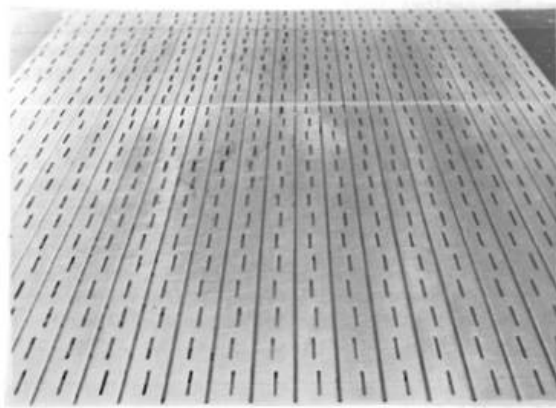


Figure 15 Metalized CFRP Slotted Waveguide Array from ERS-1

1.8 Aircraft Structures

Since the Wright Flyer, aircraft have used stringers and stiffeners in its structures along with a skin covering to allow for directional strength and to decrease weight by not having to keep a solid load bearing member throughout the design. These stiffeners come in many different shapes to include “T”, “L”, “Z”, blades, and top hats. The stiffeners are used to provide bending strength to the plain panel. The typical top hat stiffened panel may look similar to Figure 16. This specific panel is one designed by Toi et al. with the goal of creating an affordable composite panel for use in primary wing structures[19]. Stiffened panels are common in both metal and composite construction, but the advantage of composites is that the structure can be much lighter and involve less fastening devices. For example, the goal of the Toi et al. design was to create a wing structure with 15% lighter weight and 50% less parts in comparison with typical aluminum wing box structures[19]. Composite structures are also very tailorable to many applications, especially in a woven or braided nature. The complex structure shown in Uozumi and Kito shows the dynamic and broad nature of the application of CFRP woven structures and the ability for complex structures to be seamlessly woven into a single piece[16].

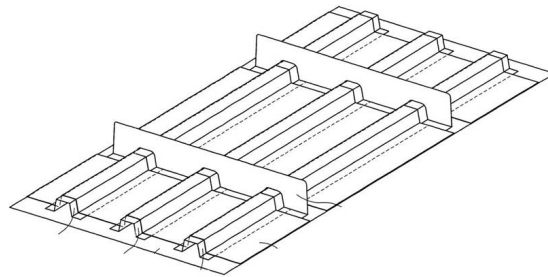


Figure 16 Typical Top Hat Stiffened Panel for Aircraft Structure

Another example of the use of CFRP stiffened panels is shown by Bucci and Mercurio[20]. For both flat and curved configurations, it was shown that a bead stiffened panel of the form of Figure 17 could resist limit loads of the aft fuselage section of a medium sized transport aircraft. It is easy to see the resemblance of a SWASS structure. This has direct application to the earlier examples of the AWACS and Saab 2000 since these are mid-sized aircraft that could possibly already have panels of this type integrated. With some slight modifications, these panels could easily be turned into SWASS components. This is the promising nature of the SWASS research. The fact that aircraft already carry structures that resemble SWASS components allows for relatively easy integration if SWASS panels can be proven structurally sound.

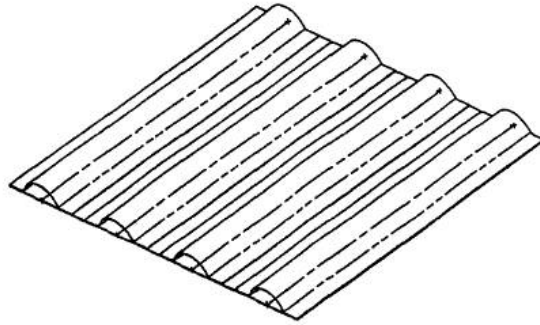


Figure 17 Bead Stiffened Panel for Use in Fuselage of Mid-Sized Transport

1.9 Previous Work in CFRP Compression

CFRP structures have been tested and designed since the 1970s and much work has been done in the area of compression. Fibrous materials are inherently better performing in tension so compressive properties are of great interest. Of specific interest to this thesis is work that has compared FE modeling to experimental results as this is the goal of

compressive testing of SWASS components. Mamalis et al. provides a great report detailing the axial compression of CFRP square tubes in both FE and lab tests[21]. Research showed that numerical simulations proved valid and held to within a maximum of 4.5% error in three different modes of collapse. The data became more scattered in impact energy absorption tests, but this thesis will concentrate on static loading and so the comparison proves promising.

Ochoa, Roschke, and Bafrali also showed good numerical simulation with the use of the program Abaqus[22]. This is the same program that will be used in this thesis so the results are encouraging. Ochoa et al. dealt with the compressive performance of circular tubes with varying degrees of damage, which can be correlated to the slots being cut in the waveguides. The results showed that any type of damage dramatically decreased the limit loads of the specimens. Specifically, the three types of specimens were all 12 inch(0.305m) long, 4 inch(0.102m) outer diameter tubes: one with no damage, one with a 0.5 inch(0.013m) diameter hole, and one with a 2 inch(0.051m) diameter hole. With the non-damaged tube as the control (100%), the second two tubes showed compressive limit loads of 48% and 22% respectively. These are much larger holes than expected in the slotted waveguides, but the results are a good baseline for comparison. No specific research could be found on the effect of multiple holes in CFRP tubes or holes in square tube configurations. The slotted waveguide research will be unique and relevant.

1.10 Research Approach

The multifunctional nature of SWASS lends the research approach to a multi variable optimization problem to balance the RF and structural performances. Since this

is a new concept with very little testing complete, the research will focus on elemental characterization of some of the smallest elements of the SWASS system to allow for further development from the basic data in the future. This research is being sponsored by the advanced structures division of the air vehicles directorate of AFRL. AFRL will complete all of the research in the RF areas while the initial structural research will be the topic of this thesis.

The RF research will focus on developing the ideal material for the inner lining of the waveguides, deciding on a slot design and array configuration, and characterizing the electrical performance of each configuration. It has been previously determined that plain carbon fiber inner linings of the waveguide do not present a detrimental decrease in performance as compared to metal linings and so the structural research will be performed with no inner lining.

The research will follow three distinct steps with many tasks associated with each step. The first step includes material characterization since no data on the specific CFRP is available. The second step includes FE analysis of the specimens in compression. The third step is a laboratory compression test of the waveguide tubes. The primary goal of the lab tests is to validate the FE model. The overall objective will be to produce FE compressive performance verified experimentally for single waveguides with longitudinal slot arrays as well as stress/strain field data for seven individual slot configurations.

1.11 Chapter Outline

The introduction provided a brief background of research and components. Chapter 2 will provide the theory required for finite element simulations. Chapter 3 will detail the

experimental work completed before testing and the setup of all tests. Chapter 4 will provide the results of the tests and comparisons. Chapter 5 will conclude the research and provide insight into future directions of the program.

II. Theory

The finite element modeling required for numerical analysis will take advantage of many pre-developed concepts. These include the use of an eigenvalue solution for buckling mode calculation, the use of Abaqus continuum shell elements in a converged method, and the Riks method for the solution of nonlinear equilibrium points and limit load calculation. This chapter will cover the necessary background required and an overview of the finite element modeling considerations specific to this model.

2.1 Instability Analysis

Since the waveguide is a structural system that contains the characteristics of both thin walled plates on its side walls and a beam overall, it is a structure at risk for buckling and instability. The critical load calculation for the waveguides was accomplished with an instability analysis. In general linear (bifurcation), and nonlinear (limit load) solutions are the two types of instability. A typical solution will have the characteristics of Figure 18. The linear analysis usually overshoots the actual performance when nonlinear equilibrium is considered.

2.1.1 Linear Bifurcation Analysis by the Lanczos Method. The buckling, or bifurcation, characteristics of a model are governed by linear behavior since the equations are linear. Finite element formulations are typically defined by a stiffness and mass matrix. When the eigenvalues of this system are found, these are the buckling loads of the structure. The system is limited to be linear in nature because the displacements of the structure are linearly related to the loads by the stiffness matrix. In plates and beams, the buckling load

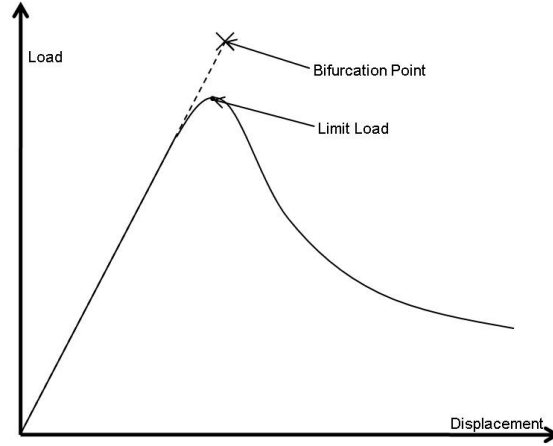


Figure 18 Representative Comparison of Bifurcation analysis with Limit Load Calculation

is reached when there is an equilibrium point between the strain energy being absorbed by the structural deformation on a small scale and the energy that could be dissipated if the structure could take on a new configuration with larger deformations. Until the buckling load is reached, the energy absorbed by this large out of plane deformation would not be sufficient to keep the structure in its lowest energy state, which is the state always preferred in nature. Euler buckling theory is a proven method of bifurcation load calculation for beams and takes the form of Eq. (2), where the L_{eff} is based on the boundary conditions. A simply supported beam has an L_{eff} equal to the actual length of the beam and a beam that is clamped on both ends has an L_{eff} equal to half of the beam length. The P_{cr} value is the critical load where the beam buckling is reached. Classical plate buckling theory also allows for a critical buckling load calculation of a square plate given by Eq. (3) where σ_{cr} is the critical buckling stress per unit length, b is the length or width dimension, and D is a stiffness term defined by Eq. (4).

$$P_{cr} = \frac{\pi^2 EI}{L_{eff}^2} \quad (2)$$

$$\sigma_{cr} = \frac{4\pi^2 D}{b^2} \quad (3)$$

where

$$D = \frac{Et^3}{12(1 - \nu^2)} \quad (4)$$

The specific method chosen to calculate eigenvalues for the FE simulations was a Lanczos solver. This method is proven effective for only the first and last few eigenvalues of a large, sparse matrix[23]. The stiffness matrix is usually large and sparse since each element's stiffness is only applied at the specific nodes it is composed of. In structural analysis, the first eigenvalue is of most concern since this will be the critical load to design against for buckling prevention. For this simulation, only the first five eigenvalues are requested so the limitations of Lanczos do not come into play. Lanczos can be used for the calculation of eigenvalues for any matrix, but the accuracy decreases significantly as the method is propagated due to roundoff errors. These buckling calculations then gives a first cut at a limit load considering only the linear behavior of the system.

The Lanczos method solves for the eigenvalues and eigenvectors of the typical finite element system shown in Eq. (5) where \mathbf{K} is the stiffness matrix, \mathbf{M} is the mass matrix, ϕ are the eigenvectors, and λ are the eigenvalues. The Lanczos method takes advantage of a matrix tridiagonalization and then the final eigenvalues and vectors are derived from

the tridiagonal matrix. The first step includes selecting an arbitrary starting vector \vec{x} and calculating \vec{x}_1 based on Eq. (6). The next steps include calculating a series of α and β values that will constitute the components of the tridiagonal matrix as can be seen in section 11.5.1 of Bathe[23]. Eq. (7) gives the representative tridiagonal matrix (T_n) where n is the order of the stiffness and mass matrices. Then the eigenvalues and vectors of the original system can be found by Eq. (8) defined by (9).

$$\mathbf{K}\phi = \lambda\mathbf{M}\phi \quad (5)$$

$$\vec{x}_1 = \frac{\vec{x}}{(\vec{x}^T \mathbf{M} \vec{x})^{1/2}} \quad (6)$$

$$T_n = \begin{bmatrix} \alpha_1 & \beta_1 & & & \\ \beta_1 & \alpha_2 & \beta_2 & & \\ & & \ddots & & \\ & & & \alpha_{n-1} & \beta_{n-1} \\ & & & \beta_{n-1} & \alpha_n \end{bmatrix} \quad (7)$$

$$T_n \tilde{\phi} = \frac{1}{\lambda} \tilde{\phi} \quad (8)$$

$$\phi = X_n \tilde{\phi} \quad (9)$$

This method so far has not produced orthonormal eigenvectors and so the Lanczos transformation must be used since using a traditional Gram-Schmidt orthogonalization method would be inefficient for such a large matrix. The Lanczos method takes advantage of a Rayleigh-Ritz transformation of the eigenvalue problem, which gives a new tridiagonal matrix (T_q) and the approximate Lanczos eigenvalues (ν) and eigenvectors ($\bar{\phi}$) are found from this new T_q . Eq (10) gives this new system where the Lanczos eigenvectors are found by Eq (11). These results can also be incremented and refined by substituting better initial estimates of the starting vector into Eq. (6).

$$T_q s = \nu s \quad (10)$$

$$\bar{\phi} = X_q s \quad (11)$$

2.1.2 Nonlinear Limit Load Calculations by the Riks Technique. The nonlinear analysis becomes very appropriate for this type of problem. In general, a model can have nonlinear effects coming into play through the material, the geometry, or the loading. The orthotropic nature of carbon fiber would typically cause nonlinear material effects and the nonlinear response should be followed in this case. The slot array that will be cut into one wall will certainly give a nonlinear geometry effect. Nonlinear effects can also be traced when large deformations occur and the full nonlinear stress-strain relations must be used. The solution of this new system of nonlinear equations then requires an advanced solution method. One such method is the Riks technique, or arc length method, which solves the

system in a piecewise fashion propagating towards a final solution[24]. One advantage of the Riks technique over other nonlinear solvers is that the Riks technique can trace the instability behavior past the limit load. Tracing beyond the limit load is not a necessary procedure for the requirements of limit load calculation, but the Riks technique is still accurate up to and including the point of instability and allows for a clear determination of the limit load from a load-displacement curve. The post limit load behavior can also be used for a check of realistic behavior and solutions.

The Riks method is based on the Newton-Raphson method for solving nonlinear equations. In general, the Newton-Raphson method is dominated by Eq. (12) where K_T is the stiffness matrix tangent to the current point on the loading curve, Δq is the increment of displacement, and $F(q)$ represents the equilibrium equations as a function of the displacement. The Riks approach adds an element of constraint to the equations by defining an arc length, (l) , that will control the incrementation of the solution.

$$K_T \Delta q = -F(q) \quad (12)$$

$$\Delta l^2 = \Delta q_j^T \Delta q_j + \Delta \lambda_j^2 \vec{P}^T \vec{P} \quad (13)$$

where Δl is the arc length, $\Delta \lambda$ is a load proportionality factor, and P is the load vector.

In a typical Newton solution, the load would be the control for the incrementation, but the nature of the equations is such that load and displacement are interrelated and the displacement must increase but load decrease after the limit point. This load control would

then not allow incrementation beyond the limit point, so the arc length as described in Eq. (13) is used as the control.

Figure 19 shows a representative Riks solution with arc length annotated. The first solution point on the curve where the tangent stiffness matrix will be evaluated and arc length controlled is point A; it will be assumed the solution has progressed to this point previously. The Newton-Raphson solution method will be applied with intermediate solutions along the arc length until the next solution point on the loading curve (point B) is reached. This process is repeated until a stopping condition has been reached, usually set to a maximum number of increments or a maximum displacement. The limit load then will be the maximum point reached during the analysis.

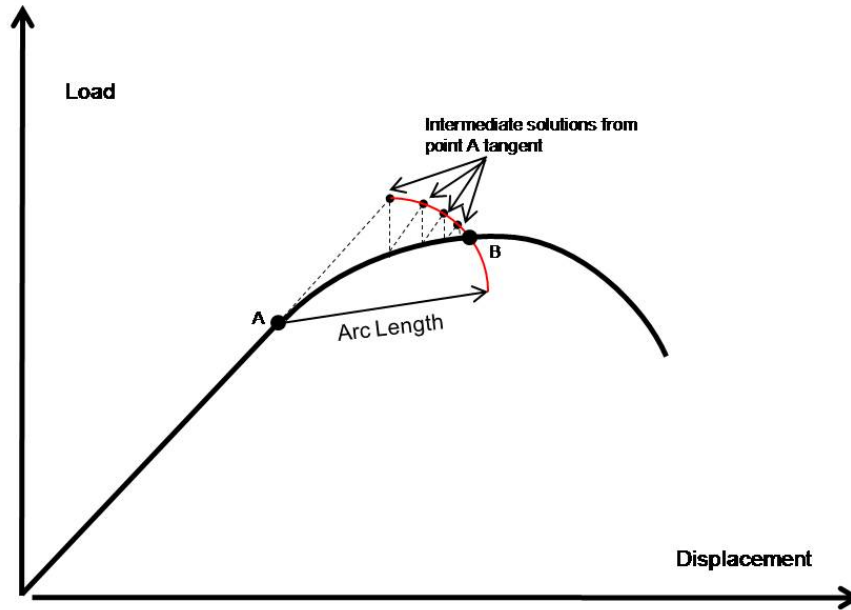


Figure 19 Visualization of Arc Length Parameter Used for Incrementation in Riks Analysis

2.2 Element Theory

The element used to represent the structure in the FE model is an eight-noded hexahedron element. Figure 20 shows a representative figure of the element and shape functions for isoparametric conversion can be seen in Table 1.

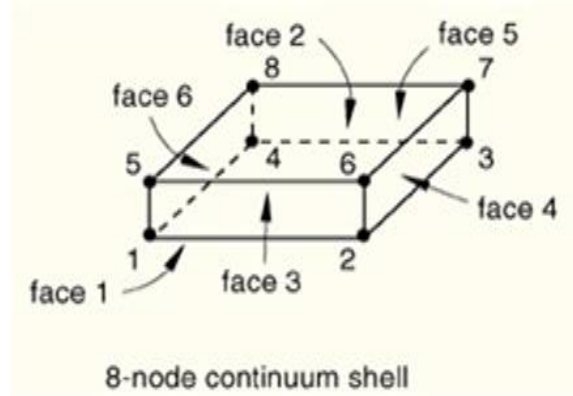


Figure 20 Eight Noded Continuum Shell Element

Table 1 Shape Functions
for Eight Noded
Isoparametric
Hexahedron
Element

N1	$\frac{1}{8}(1 - \xi)(1 - \eta)(1 + \zeta)$
N2	$\frac{1}{8}(1 - \xi)(1 - \eta)(1 - \zeta)$
N3	$\frac{1}{8}(1 - \xi)(1 + \eta)(1 - \zeta)$
N4	$\frac{1}{8}(1 - \xi)(1 + \eta)(1 + \zeta)$
N5	$\frac{1}{8}(1 + \xi)(1 - \eta)(1 + \zeta)$
N6	$\frac{1}{8}(1 + \xi)(1 - \eta)(1 - \zeta)$
N7	$\frac{1}{8}(1 + \xi)(1 + \eta)(1 - \zeta)$
N8	$\frac{1}{8}(1 + \xi)(1 + \eta)(1 + \zeta)$

The specific type of element is a continuum shell element which combines some of the advantages and properties of conventional solid and shell elements. The element is a three dimensional element and so it allows for through thickness mesh refinement as opposed to conventional shell elements which only define a reference surface and can only

have one thickness element. The continuum shell thickness direction is a defined parameter, unlike solid elements, and shear properties through the thickness direction are estimated by assuming a quadratic shear variation through the thickness and zero shear values at all free boundaries. This is done to save computational expense. The thickness direction can be any element direction, but must be specified before analysis. The thickness direction is not required to be the smallest dimension of the element, but this is usually the logical choice. The defined thickness direction must also correspond with the actual model's thickness direction. The continuum shell element is used to model three dimensional structures and has displacement degrees of freedom only at each node like a typical solid element. The displacement is allowed in all three principle directions, but no rotation degrees of freedom are present, so the element has linear interpolation between any two nodes. The element does allow for large rotations between nodes and elements and so should be a good choice for the nonlinear analysis of this model.

2.3 Overview of Abaqus FE Model

The FE model created for this thesis is a three dimensional model of the composite waveguide. Appendix A explains the details of the model construction and analysis in a step by step fashion. The basic model was created by an extrusion process for the desired shape and extruded cuts in appropriate places for slots. Figure 21 shows a basic representation of a waveguide with five slots placed in one face.

When modeling composite structures in Abaqus, there are a multitude of different methods of modeling. The graphical user interface of the program has a built in composite modeler called the composite layup editor. This editor can be used for any macroscopic

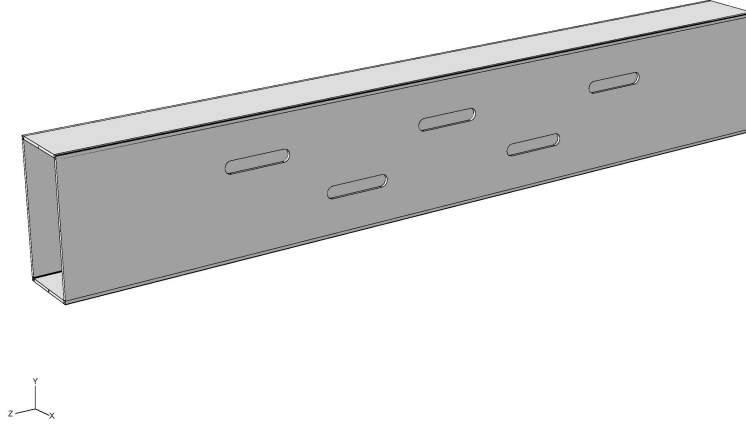


Figure 21 Finite Element Model Assembly Used for Waveguide Analysis

composite modeling type allowed in Abaqus. The layup editor allows the user to build a layup of different materials and specify orientations, the region of application, the stacking direction, how many integration points should be used through the thickness for shell elements, and other tools. Since the material properties for this specific woven fabric and resin layup were not known, the material was tested at the fiber orientation being used for the waveguide and so the properties were input as the principle properties in the one and two directions although these were not the orthogonal fiber directions. This allowed for a simpler symmetric layup of two plies at zero degree orientations and simpler testing for properties experimentally. Figure 22 shows the fiber orientations of the woven fabric as it is layed up into a waveguide configuration. The one and two directions for the layup will not be used, but the x and y directions shown will be input as the one and two directions for the layup and a zero degree orientation angle applied. In specifying the layer material properties in Abaqus, the user has a few options: a typical engineering lamina,

an orthotropic property designator, and a fully anisotropic material. Each makes some assumptions about the material symmetry except fully anisotropic which allows for full inputs of the stiffness matrix. For the case of simplicity in material property collection from the laboratory, an engineering lamina configuration was chosen. This type of layup assumes a plane stress type of configuration, which is a reasonable assumption due to the thin shell nature of this waveguide structure and the composite layers. Even on the short side of the waveguide, the thickness dimension is about 10% of the length, allowing for a plane stress assumption. This engineering lamina material requires the following properties for input: modulus of elasticity in the one and two directions (E_1, E_2), the in plane poisson ratio (ν_{12}), and the shear modulus of elasticity in the three major planes (G_{12}, G_{23} , and G_{13}). The experimental calculation of these material properties is explained in section 3.1 later. Once the material properties of each layer is specified, the layup editor is used to designate the layup that will be used; in this case a two layer layup of the carbon fiber fabric at zero degree orientations.



Figure 22 Principal Fiber Orientations of Fabric and FE Model Input Directions

Abaqus is limited in its use for square corners since the layup direction must be specified in the program and the square corner provides an inconsistency. To fix this problem, a rounded fillet must be created to allow for a smooth transition around the corner of the model. Figure 23 shows how there is a plane of discontinuity in the stacking direction due to a square corner and the application of a fillet to fix the problem. The stack was then nearly continuous around the waveguide and modeling much more accurate.

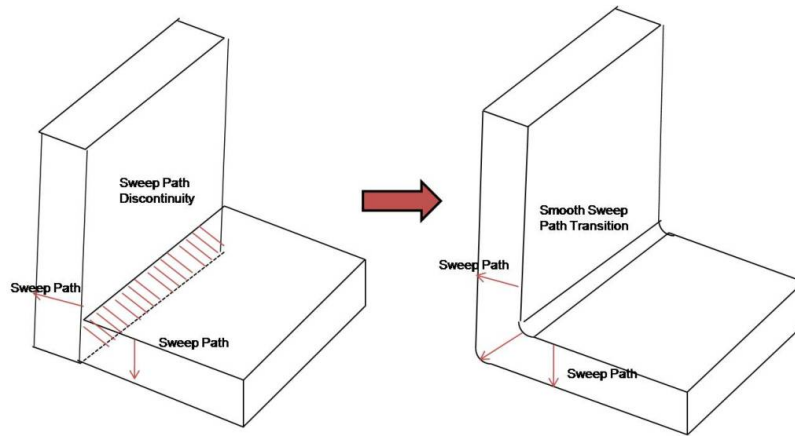


Figure 23 Problematic Square Corner with Curved Transition Solution

After the user has specified the layup, an element must be selected for meshing. The three composite element types available in Abaqus include shells, solids, and continuum shells. The use of solid elements is not recommended due to the nature of the solid elements only being able to vary through thickness shear stresses linearly[25]. Conventional shell elements do not provide any refinement in the through thickness direction since they model a thin shell only and only define a reference surface and calculate properties away from that reference surface based on some type of interpolation or extrapolation. The advantage of continuum shells is that they can be applied in a three dimensional model with multiple elements through the thickness while allowing for a quadratic transverse shear stress estimate

and reduced computation time as compared with solid elements. Refinement of the through thickness properties of a continuum shell can also be accomplished by means of integration points. In the composite layup editor, the user has the option of how many integration points to create through the thickness of each composite layer. This is independent of the number of elements through the thickness, but one should take care to create meaningful integration points that can tell the user behavior at composite layer interfaces and other areas of interest. The default is to have three integration points through each layer which would allow for the performance at the top and bottom surface of a ply as well as the middle surface. For more accuracy, five integration points were chosen for this model. Figure 24 shows the details of the integration points through the two layer composite layup.

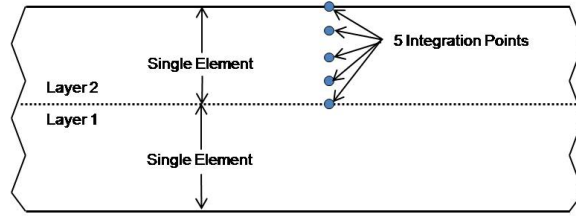


Figure 24 Layup Detail Showing Five Integration Point Locations

The SC8R element used is a reduced integration element. This helps to reduce computation time for the highly complex nonlinear analysis [26]. This reduced integration has a softening effect on the structure, which can help to combat the stiffening usually associated with linearly interpolated elements. Reduced integration can introduce a spurious deformation mode into the structure though and this must be checked for in the solution. Abaqus recommends that the user check the results of a model to see if “hourglassing” is occurring. This effect is one where the elements will take on alternating trapezoidal shapes

as shown in Figure 25. This is an undesirable and false result. If hourglassing is present, a finer mesh must be created.

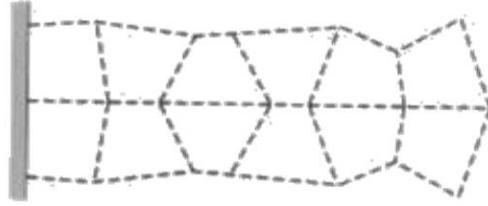


Figure 25 Spurious Hourglass Mode from Course Mesh of Linear Elements

Some details of the continuum shell element are left to the user to ensure accuracy. As mentioned earlier, the user has the option of defining the thickness direction of the continuum shell element. The default value would be the three direction of the element. The control of the thickness direction is applied in the composite layup editor. If the three direction is kept as the thickness direction, then the user must take care to define the orientation of the layup with a local coordinate system that has the three direction as the outward normal of the layup.

2.4 Mesh Refinement for Mesh Independence

It is crucial in any numerical simulation to ensure small enough discretization for an accurate solution. In FE analysis, this means creating small enough elements across the domain to ensure a converged solution. The refinement was accomplished through a comparison of the von Mises stress values along a path through the slotted waveguide face during a static loading condition of ten pounds (44.5 N). Figure 26 shows the path that was chosen to capture the most extreme stress changes in the model. Global seed values of 0.044, 0.022, and 0.011 inches were applied (0.0011, 0.0006, 0.0003 m). Figure 27 shows a

snapshot of the three meshes on the undeformed shapes. The pictures are enlarged to show the details around three of the slots since the finest mesh is too fine to print over the whole waveguide.

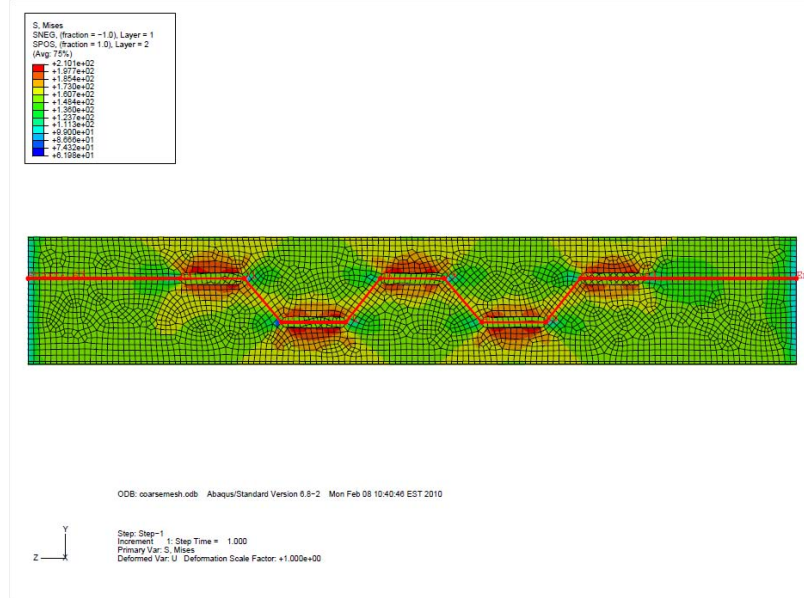


Figure 26 Path Used for Extraction of von Mises Stress Values for Mesh Refinement

The thickness value of the waveguide is 0.022 inches (0.0006 m) and so the three meshes represent 0.5, 1, and 2 elements through the thickness respectively. Figure 28 shows the von Mises stress values along the path. One can see the lower mesh has a few odd spikes and does not accurately represent the stress distribution in between the slots (the four round peaks in the center are the transition regions from one slot to the next). The stresses for each element are calculated and then the nodal stress values are the average of all of the elemental stresses around the node, so the smoothing out of the stress over an element is apparent in the coarse mesh. The finer two meshes are fairly similar and both show smooth plots in the slot transition areas. From the von Mises stress data, in the worst areas in between the slots (shown on the graph in black arrows), the percent difference of the is only

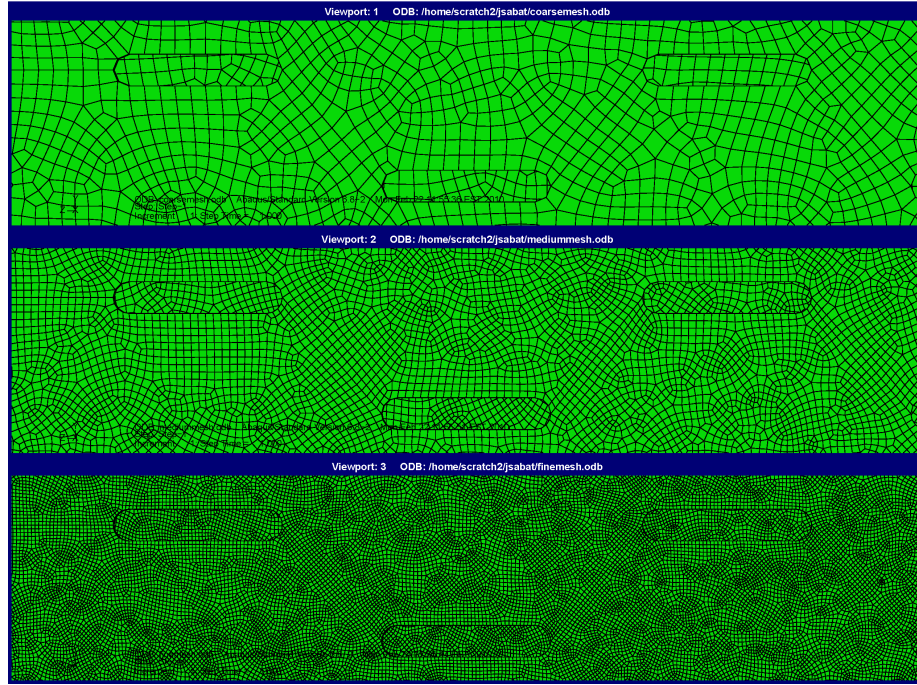


Figure 27 Three Meshes on Undeformed Shape of Slotted Waveguide (Global Seed values 0.044, 0.022, and 0.011 Top to Bottom)

1.3%. This means that the green line represents a refined mesh. In order to allow for better stress fields around the slots as seen in the bottom image of Figure 29, local seeds of 0.011 inches (0.0003 m) were applied around the slot edges, but 0.022 global seeds were applied to the rest of the part. Using 0.011 global seeds would be extremely computationally expensive and is not necessary. Table 2 gives the maximum von Mises stress at the slot tip for each mesh as well as computational times. One can see that the mixed mesh gives the accuracy of the von Mises stress while still allowing for computation times on the order of the 0.022 global seed mesh.

Table 2 Critical Values for Four Levels of Mesh Refinement

Global Seed Size (in)	Max von Mises Stress (psi)[Mpa]	Computation Time (s)
0.044	210.1 [1.449]	11.2
0.022	238.8 [1.646]	49.9
0.011	285.1 [1.966]	682.7
0.022 with 0.011 Slots	294.6 [2.031]	58.5

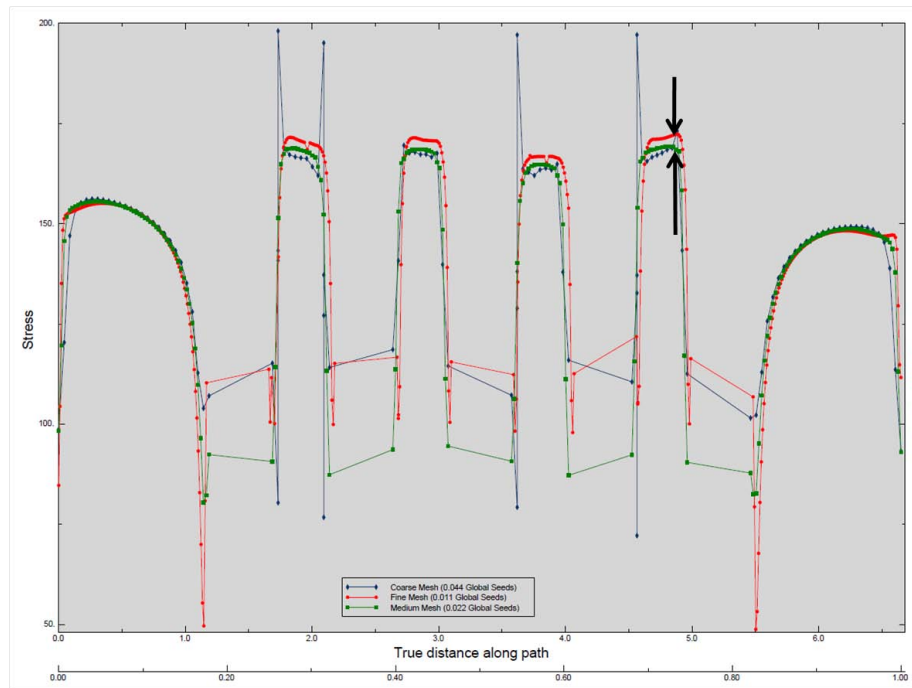


Figure 28 Von Mises Stress Plot along Path of Three Meshes (Global Seed values 0.044, 0.022, and 0.011 in)

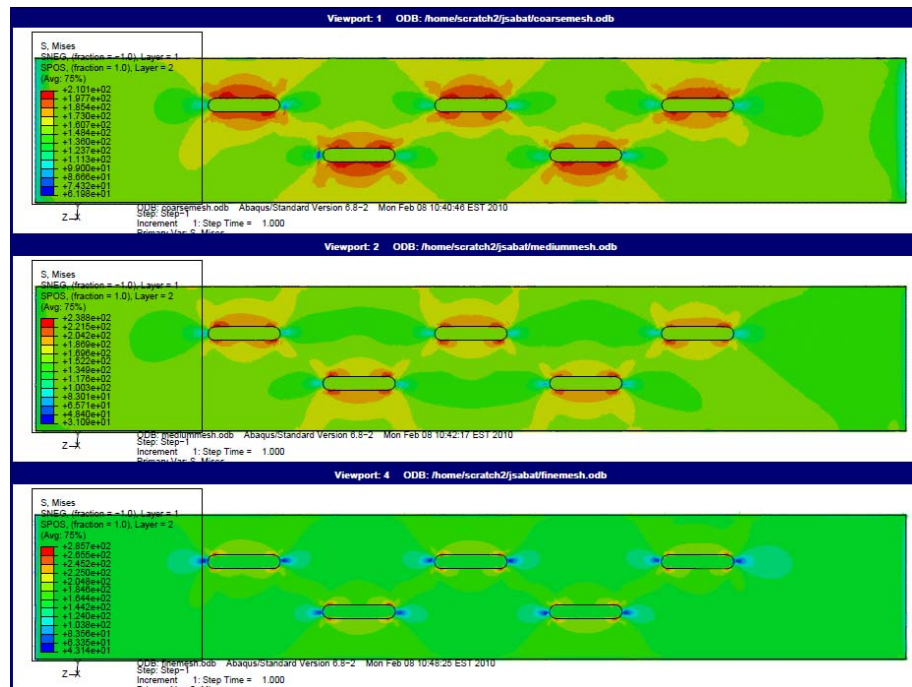


Figure 29 Von Mises Stress Contour Plot of Three Meshes (Global Seed values 0.044, 0.022, and 0.011 from Top to Bottom)

2.5 Riks Increment and Imperfection Refinement

The nonlinear analysis is critical upon user inputs. The system of nonlinear equations is solved in a piecewise fashion, which requires that the incrementation be low enough to keep the solution space stable. Since the loads and displacements both can change at any given time step, the incrementation of these through the analysis is controlled by an “arc length” parameter as opposed to load control in a Newton method. The arc length represents a radial distance from the initial point to a point tangent to the last point in the curve (see Figure 19).

This parameter is defaulted to begin at one then increase initially by one, then at an increasing increment until the total number of increments requested has been reached. The accuracy of the limit load is dependent upon having enough points to create an accurate representation of the behavior. The Abaqus defaults are sufficient for a quick initial estimate of the arc length where the limit load is reached, but in order to create fine enough data points, the maximum increment should be set to a lower value than the default of 1e6. For the purpose of this analysis, the maximum increment was set to equal 100 and provided excellent results. A refinement study on an early model is shown in Figure 30 and Table 3. One can see smooth results for both the 100 and 10 arc length increments. The 100 increment data is only 0.04% from the 10 increment and the computational expense of the increment of 10 is an order of magnitude greater so 100 is used.

Table 3 Riks Refinement Study Data

Max Increment	Limit Mises Stress at Node 10654 (ksi)[GPa]	Computation Time (s)
10	60381.1 [416.313]	26371
100	60352.4 [416.115]	4220
1E6	73732.7 [508.369]	2305

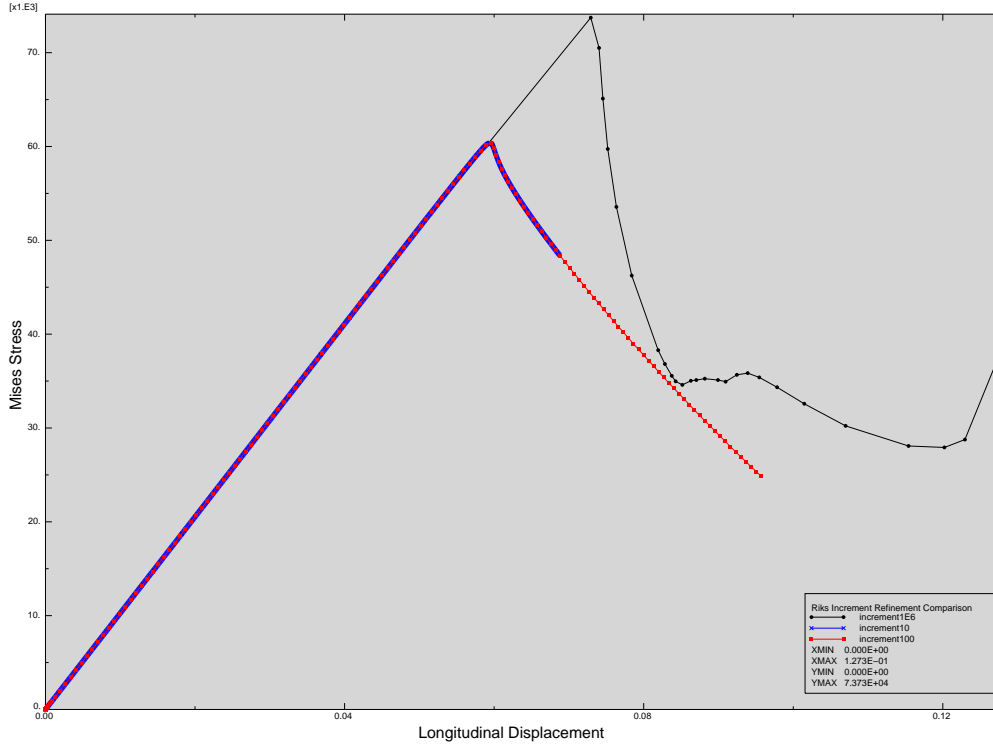


Figure 30 Riks Increment Refinement Plots Showing Arc Length Increments of 10, 100, and 1E6

The Riks analysis for the plain non-slotted waveguide also required a type of convergence study. Since the plain waveguide has little to no nonlinear features from the outset, an imperfection must be placed on the model to allow for instability and the application of a moment from the outset. This imperfection was applied in the form of a percentage of the displacement seen in one of the eigenvectors. This is done to help progress the plain waveguide solution towards the buckling shape that one would expect through experimentation. The imperfection applied specifically was a percentage of the first eigenvector. A study was completed with various amounts of imperfection until a small enough value was achieved so as to see convergence of the limit load values. Table 4 shows the details of the study. Since the one-thousandth percent imperfection increased the limit

load by only 1.3% the solution was assumed converged and a 0.00001 factor of the first eigenvector was applied as the waveguide imperfection before all plain waveguide analyses.

Table 4 Riks Imperfection Convergence Study Data

Imperfection Percentage	Normalized Limit Load	Percent Increase in Limit Load
1%	1	Reference
0.1%	1.0415	4.15%
0.01%	1.0954	3.94%
0.001%	1.0961	1.26%

2.6 Loading and Boundary Conditions

The goal of the loading and boundary conditions of this model was to effectively represent the conditions that the structure would encounter during experimental testing. The loading for the compression tests will be applied with an MTS machine by use of a six inch (0.152 m) diameter steel plate on the top and bottom of the waveguide. The bottom plate will be fixed and the top plate will have a displacement velocity applied to introduce the load. A variety of conditions was used until the final model was chosen and settled upon; first the waveguide ends were constrained and loads applied directly to the structure, next the waveguides were tied to steel plates and load and boundary conditions were applied to the plates, next a potting boundary condition was extended to the waveguide to follow the potting used for experimentation, and finally the steel plates and potting conditions were removed to allow for a simple enough model to run in efficient times.

At first, the simplest boundary condition to model the experiment was applied. The load was applied as a pressure directly to the edge of the waveguide walls and the boundary conditions were applied to the same surface (see Figure 31). The bottom surface was clamped to allow no displacements or rotations since the compressive force of the machine

would always hold the bottom surface to the bottom compression plate, which was fixed. The top surface was allowed to move only in the longitudinal direction since this is the direction the top plate will move. These conditions created excessive stress concentrations at the end surfaces. In actuality, the steel plates will have some give to them and allow for a smoother introduction of the force into the waveguide end walls and so the next boundary condition attempt added two steel plates to the model.

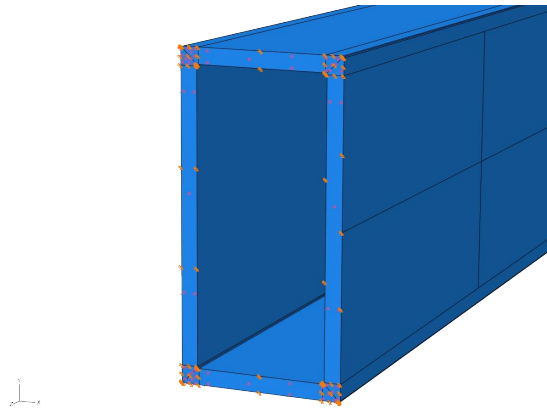


Figure 31 Loads and Boundary Conditions Applied Directly to End Surface in Early Attempts

Two steel plates were created with six inch (0.152 m) diameters to match the plates that were to be used in the lab setting. These were added to the model assembly by the use of a tie constraint between the edges of the waveguide and the steel plate surface. Since there would always be a compressive force on the waveguide, the tie constraint was thought to accurately represent the contact interaction. Since the waveguide was tied to the plates, the load was applied to the top of the steel plate and the boundary conditions were applied to the top and bottom plates only and not the waveguide (see Figure 32). This allowed for a much smoother introduction of the force and some stress was then held by the plate when loading the waveguide.

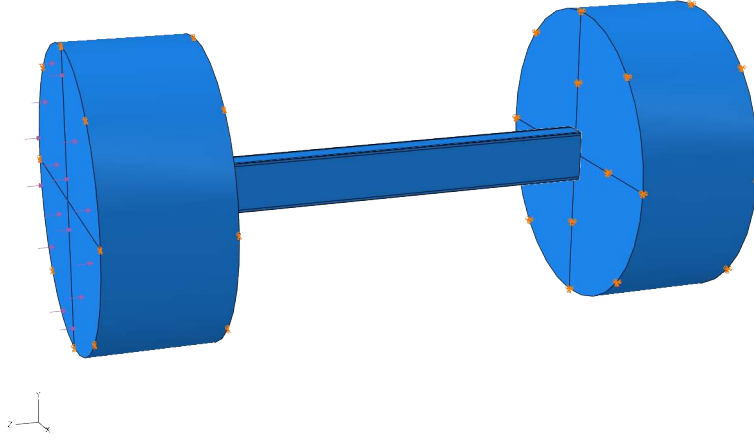


Figure 32 Loads and Boundary Conditions Applied to Steel Plates in Intermediate Attempts

The next adjustment of boundary conditions came due to the nature of the waveguide configuration during testing. In order to better stabilize the waveguide between the two plates in the lab, it was decided to pot the ends of the guide with a one inch (0.025 m) aluminum epoxy material on each end. Figure 33 shows this potting on one of the specimens. Since this potting would prevent the waveguide from moving out of the compression axis during the test, it was decided to extend the steel plate boundary conditions one inch (0.025 m) on each end of the waveguide. These potting pieces would effectively extend the steel plate conditions around and inside the waveguide, so extending the boundary conditions in the model is the reasonable answer.

The final configuration used for the models was back to the original model of a single waveguide, except the length of the waveguide was shortened to six inches (0.152 m) to reflect the potted boundary conditions. This change of model was driven out of necessity



Figure 33 Potted Waveguide Specimen

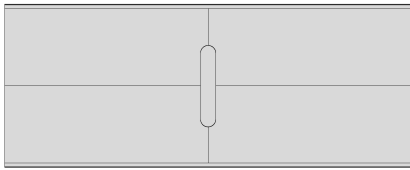
of creating a smaller domain to allow for reasonable simulation times. With the mesh refinement study complete, the size of the elements shrank tremendously and the model was simplified to allow for reasonable times. The stress concentrations seen initially were still present, but were accepted due to the advantage of computational efficiency.

2.7 Slot Characterization

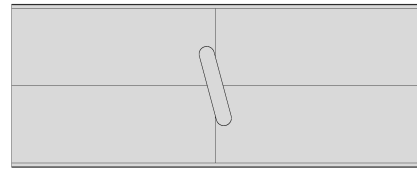
The slot orientation characterization was accomplished using a simple static analysis. The main goal of slot characterization was to determine the stress and strain fields and the flow of those values around a series of seven slot configurations. The different configurations are all possible configurations for SWASS employment with varying degrees of RF performance. The H slot is a novel slot concept that was developed to be fit into the narrow wall of the waveguide. This was given to allow for an alternate configuration in the case of poor structural performance in the broad wall. It is predicted that the orientation of the slot in the narrow wall will allow for a greater bending and buckling stiffness of the waveguide since the second moment of inertia is greater around the axis that bisects the broad walls. If a SWASS panel can be made with slots on the narrow wall, then the possibility for bending resistance may be greater. The other slots are variations that may be possible in a radar configuration. This elemental study should give good structural data for an optimization

study when deciding on a waveguide configuration. Figures 34 shows the seven different slot configurations and a representative figure.

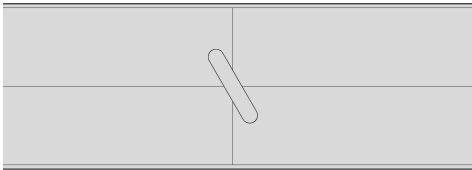
A 1000 pound (4.45 kN) load was applied to the end of each configuration and the stress fields analyzed. When viewing the von Mises stress outputs, the waveguides were lengthened until all stress interactions with the top and bottom boundaries were no longer apparent in the default contour view. Figure 35 shows an interacting condition on the top and the bottom shows a stress field that is not affected by end conditions. Since there will always be some sort of gradient between the boundary and the slot, the default contours were chosen since all slots would share similar stresses. This default view creates a separation of about 4 to 5 ksi (27.6 to 34.5 MPa) between contour lines, therefore in this case, the difference in farfield stresses and slot stress concentrations must be greater than 4 or 5 ksi (27.6 to 34.5 MPa) to allow for a non-interacting configuration. Interaction with the side boundaries is inherent in the waveguide models and cannot be avoided without redesigning of the waveguide, which would require frequency changes and other significant and unacceptable updates, therefore the side boundary interactions were accepted and left alone.



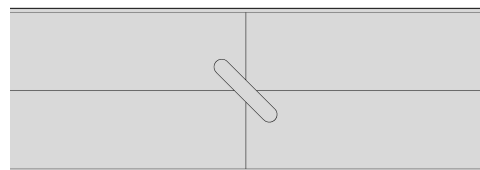
(a) Horizontal Slot



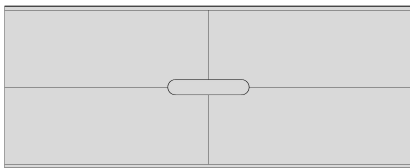
(b) 15° Slot



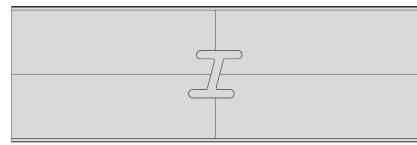
(c) 30° Slot



(d) 45° Slot



(e) Vertical Slot



(f) H Slot in Broad Wall



(g) H Slot in Narrow Wall

Figure 34 Seven Slot Configurations and Representative Figures

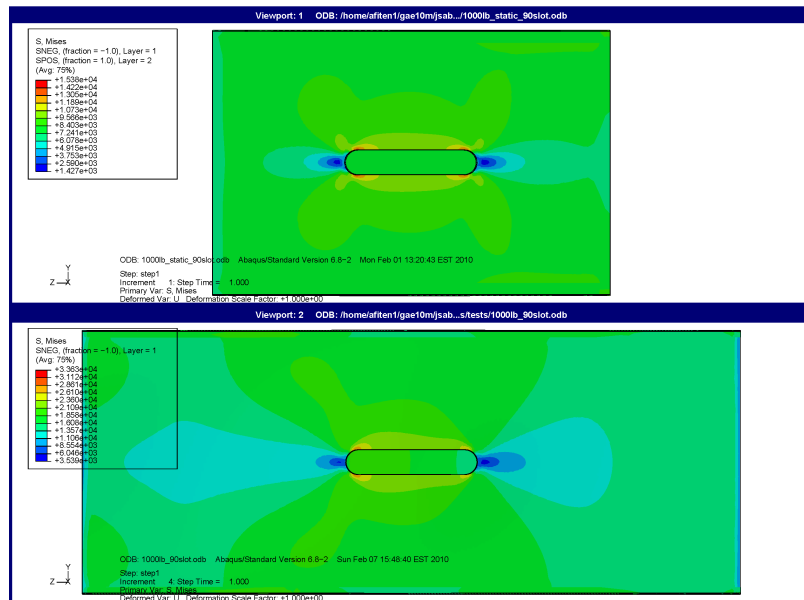


Figure 35 Longitudinal Slot with Interacting Stress Field and Boundary Conditions on Top and Independent Condition on Bottom

2.8 Processor Details

All simulations were run using Abaqus version 6.8-2 on the Linux operated machines at AFIT. Each machine has four parallel processors and these were utilized in the Riks simulations by dictating parallel process on four processors with four domains in the Abaqus job definitions.

III. Experimental Setup

The experimental methods for this thesis included two main categories: material property characterization as well as experimental compression tests of the waveguide members. This chapter will cover the preparation and testing for both procedures to include layup techniques, gaging details, and test setup.

3.1 Determination of Carbon Fiber Material Properties

The material chosen for experimental waveguide construction was a one inch (0.025 m) tube of woven carbon fiber fabric[27]. The manufacturing company does not provide detailed material properties for its woven tubes other than the fiber used for construction, which is a Grafil 34-700 fiber. The general properties of the fiber are a tensile strength of 700 ksi (4.826 GPa) and tensile modulus of 34 Msi (234 GPa) but no other fiber properties are published[28]. The resin used for layup was a Tencate RS-36 resin laminated onto paper at densities of 38 and 160 grams per square meter[29]. Each material was chosen to avoid difficulties present with previous layups relative to ease of the waveguide member construction. To start with, a unidirectional IM7 prepreg carbon fiber was used, but this material proved too brittle for the small radius corners of the waveguide mandrel and was prone to cracking and nonuniform construction. The use of the woven fabric tubes was a welcome change since they only needed to be stretched and tightened over the mandrel, however material properties were then needed.

The Abaqus material requirements for a lamina composite include modulus of elasticity in the one and two directions (E_1, E_2), the in plane Poisson ratio (ν_{12}), and the shear

modulus of elasticity in the three major planes (G_{12} , G_{23} , and G_{13}). A multitude of testing standards were browsed before deciding upon two tests for material characterization. Since timeliness was a large concern, only two tests could be accurately completed. These tests included one for compressive modulus and another for in plane shear modulus. The specific tests chosen were ASTM standards D3410[30] and D7078[31]. These tests were chosen because they applied to woven CFRP materials and had specimen sizes attainable from the woven fabric tubes. These tests would then directly give the properties of the elastic modulus and shear modulus. As mentioned in section 2.3, the principle orientations would not be used, but the material would be tested in the same configuration as it is on a standard waveguide layup. Since the material is a plain weave type of woven fabric, it would have identical elastic properties in the one and two directions. This fact will be taken advantage of and once the properly oriented elastic modulus is found from test D3410, then it can be assumed to be the same modulus for the x and y directions. Due to time and material costs, only shear properties in the 1 – 2 plane will be tested for. In order to test for properties out of plane, one must create a three inch (0.076 m) thick layup which is wasteful in time, material, and costs. The 1 – 3 and 2 – 3 shear moduli will be estimated based on a similar material's shear property ratios. The similar material is a plain weave carbon fiber/phenolic resin as detailed in Daniel and Ishai[32]. This material has G_{13} equal to 55.9% of G_{12} and G_{23} equal to 76.5% of G_{12} and these will be the ratios used to determine G_{13} and G_{23} from the G_{12} found during test D7078. The only other material property required then is the Poisson ratio. This will also be estimated from the carbon fiber/phenolic resin material[32].

3.1.1 Specimen Processing Details for Compression Tests. The specimens for the D3410 compression test were prepared in the composite layup room of the Facility for Innovative Research in Structures Technology (FIRST) lab of AFRL. The test uses a clamping fixture that fits inside of two steel holders (see Figure 36). When compressive force is applied between the steel holders, the clamping wedge provides an increasing clamping force on the specimen until extremely tight and compression is introduced. The specimen was chosen to have a one inch (0.025 m) width and a one inch (0.025 m) gage length, requiring a specimen thickness of 0.161 inches (0.004 m) according to the ASTM standard. Figure 37 shows the specimen with tabbing material attached.

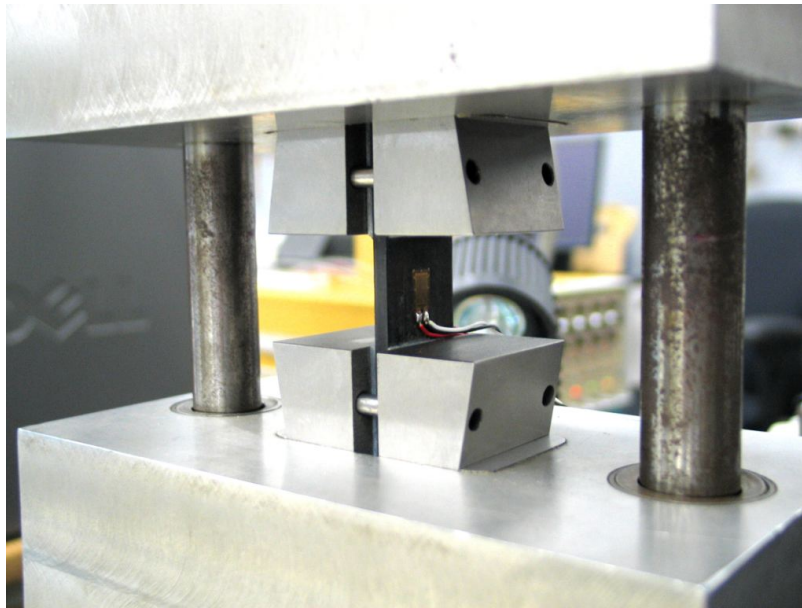


Figure 36 Compression Fixture Attached to MTS Machine with Specimen Placed and Preloaded

The one inch (0.025 m) width was recommended for a woven material and the one inch (0.025 m) gage length was chosen instead of 0.5 inches (0.013 m) for ease of gaging. Since the fabric layers had a nominal thickness of 0.011 inches (0.0003 m), 15 layers were stacked to create the appropriate specimen. The material was prepared with a 30% by mass ratio of

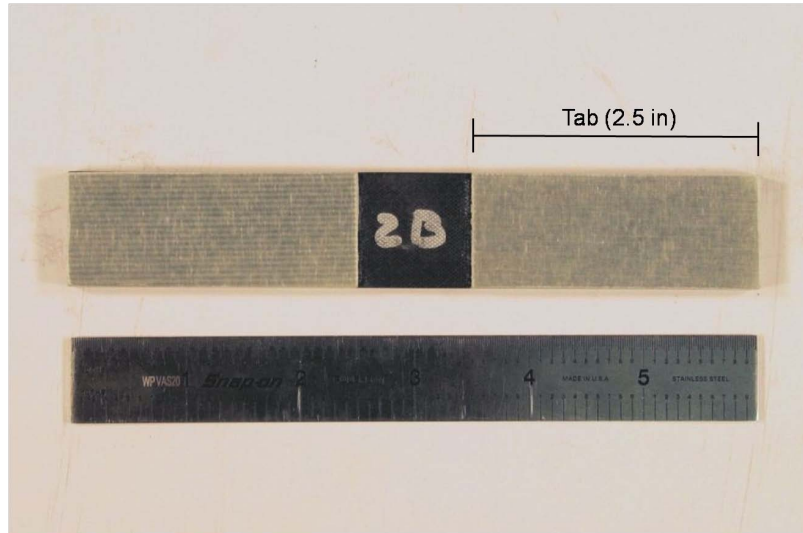


Figure 37 Compression Specimen for ASTM Test D3410 with White Tabbing Material resin. Although composite materials are typically mixed to a certain volume fraction, since the volume density of the resin was unknown, a mass fraction was used. The area density of the resin and fibers were both known and so the weight ratio was simple to calculate. The 30% mass ratio had been previously proven to give good results[32]. In order to produce a flat specimen, the cylindrical tube material was cut longitudinally and split open until flat then cut to appropriate length. Before cutting to length, the fibers were stretched to ensure proper orientation as when stretched tight over a waveguide mandrel as seen in Figure 22. Some extra length was layed up as well to allow for tolerance in the curing and machining.

As mentioned previously, a pre-measured resin density paper was used for resin application (see Figure 38). In order to transfer the resin material from the paper backing to the fiber layers, a debulking process was used. The fabric sheets were set on Teflon paper and the required sheet of resin was cut to the same size and layed on the fabric sheet. This was set into a debulking chamber that heated the resin to 160°F (344 K) and provided a vacuum to allow for resin flow into the woven fabric. After sitting in the heated

vacuum for ten minutes, the sheets were removed and allowed to cool to room temperature then the paper backing from the resin was easily removed. A similar process was used for shear specimens and Figure 39 shows a debulked fabric. These resin infused CF layers were then stacked to form the 15 ply layup and prepared for the autoclave with Teflon paper. The autoclave curing cycle was run according to guidelines for the RS-36 resin to include heating to 350°F (450 K) under pressure of 40-85 psi (0.276 - 0.586 MPa) then holding for 90 minutes then venting pressure and cooling at -5°F per minute (-4.21 K/s) until below 140°F (333 K). After curing the specimens were cut to size by use of a diamond saw and tabbed with appropriate tabbing materials to allow for smoother clamping of the material in the compression fixture. The final specimen gage section dimensions are shown in Table 5.

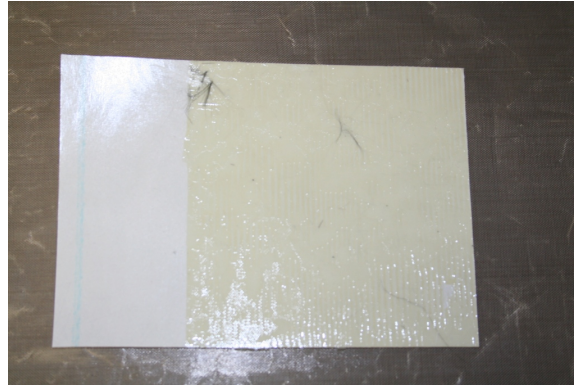


Figure 38 Resin Paper Cut to Size for Shear Specimen Ply Debulking

Table 5 Compression Specimen Gage Section Dimensions Before Testing

Specimen ID	Width (in)[mm]	Height (in)[mm]	Thickness (in)[mm]
1A	1.006 [25.55]	1.003 [25.48]	0.155 [3.94]
1B	1.007 [25.58]	1.003 [25.48]	0.150 [3.81]
2A	1.006 [25.55]	1.007 [25.58]	0.160 [4.06]
2B	1.008 [25.60]	1.005 [25.53]	0.157 [3.99]
3B	1.006 [25.55]	1.001 [25.43]	0.145 [3.68]

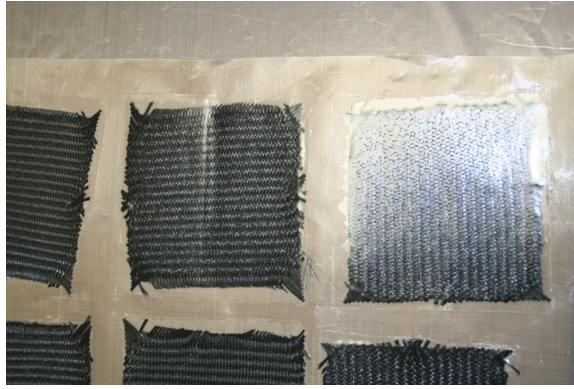


Figure 39 Debulk Resin/Fabric Sheets for Shear Specimen Layup

In order to collect the relevant data, strain gages were placed on both sides of the specimen at the center of the gage section. The gages used were Vishay Micro Measurements CEA-13-250UW-350 uniaxial strain gages. These had a gage length of one quarter of an inch (0.006 m), which was sufficient to cover more than one repeatable pattern of the woven fabric to allow for smooth strain averaging. A single gage was placed longitudinally on each side of the specimen at the center of the gage section (see Figure 40). Each gage would then display the same compressive strain to calculate the elastic compressive modulus. Any difference in strains would indicate bending in the specimen and depending on the severity, possibly an unsuccessful test. The specimen was prepared and strain gages applied according to Vishay Instruction Bulletin B-127-14[33]. The gage area was sanded to a 600 grit smoothness and marked for accurate gage placement. The gage was attached to the specimen using M-Bond 200 catalyst and adhesive then wire leads were soldered and prepared for attachment to the gage amplifier for lab use.

3.1.2 Test Setup for Compression Tests. The test setup was done according to the procedures layed out in ASTM D3410. The fixture was attached to a 20 kip (88.96

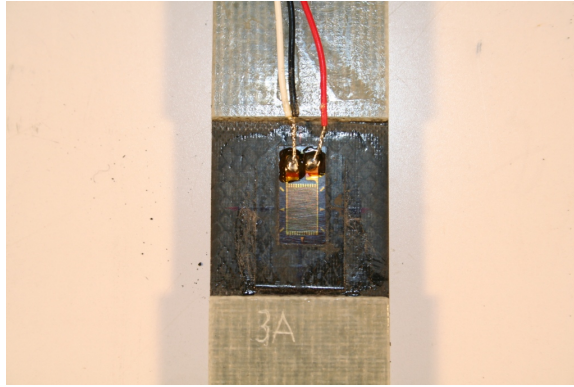


Figure 40 Compression Specimen for ASTM Test D3410 with Strain Gages

kN) capacity screw driven uniaxial testing fixture with a stationary bottom and a mobile top. The compression fixture used was attached to the machine and is seen in Figure 41. This fixture provides the clamping and compressive forces necessary for the test. Once the fixture is properly aligned, the specimen is placed in the clamping blocks and centered and fastened. One must take care to ensure the gaging wires are clear of the clamping fixtures and do not get bent or distorted or pull the gage from the specimen. Next the clamping fixture is centered and secured with a small force for steadiness (<50 pounds [222 N]) before the test is run (see Figure 36).

The strain gages are attached to a strain gage amplifier to produce the correct output and the voltage is read and displayed through a computer software program connected to the machine. The strain gages are attached to the amplifier using a three wire setup (see Figure 42), which helps to reduce the error associated with lead wire resistance changes from heating or other effects during the test[34]. The gages were introduced into a quarter bridge setup which allows for the strain gage to be the only changing resistance in the system. Each gage is connected to a separate amplifier channel with its own quarter bridge and

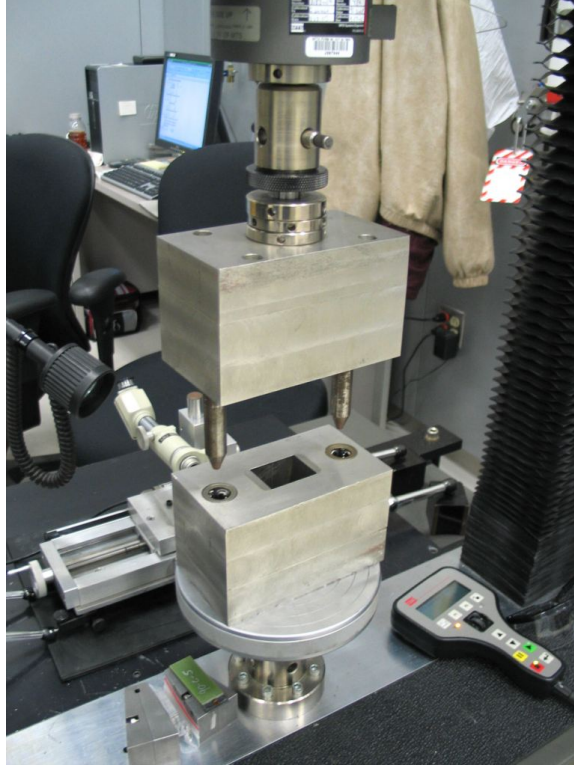


Figure 41 Compression Fixture Attached to MTS Machine

gain. The gain of each channel was set from the specifications for excitation voltage, output voltage, and active gage factor. Equation (14) shows the calculation for the gain (A).

$$A = \frac{4V_O 10^6}{V_{Ex} k \mu\epsilon} \quad (14)$$

Where V_O is the output voltage required for the computer of 10V, V_{Ex} is the excitation voltage of the quarter bridge of 5V, k is the active gage factor of the strain gage, and $\mu\epsilon$ is the maximum strain for the gage in microstrain. For one specific gage on this test, the gage factor was 2.115 with a maximum strain of 3% so the respective gain was 126.

The computer software is set up to record the time of the test, the load on the fixture, the displacement from initial, and the microstrain at each strain gage. The data acquisition

system collects a point of data every 0.2 seconds, or at a rate of 5 Hz. The test is run with a head speed of 0.05 inches per minute ($2.117\text{e-}5$ m/s). At a microstrain value of about 2000, the test was paused and the strains were checked for out of plane bending features. If the difference in strains was found to be outside of a value of 10% of the strain, then the test would be deemed invalid and the fixture readjusted to allow for a straighter configuration that would be less prone to bending. This was not necessary for any tests accomplished as all bending strains were in the allowable range (see Table 6). Tests were accomplished at room temperature with a test time reading of 70°F (294 K) and a relative humidity of 30%.

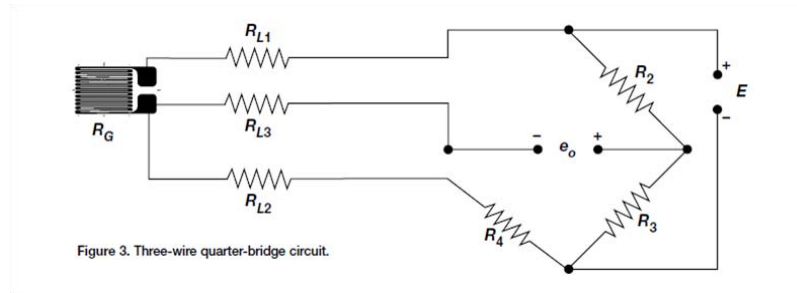


Figure 42 Schematic of Three Wire Strain Gage Setup

3.1.3 Compression Test Results. In total, five compression specimens were tested for redundancy and validation of results. The strain gage data was averaged between the two gages and plotted against the stress on the cross sectional area of the specimen in axial compression. Four of the tests proved to have very similar results and a fifth had a much softer curve but similar ultimate strength. It was decided to discard the data of the outlier. Since the other four agreed so well, it was decided this outlier most likely had bad clamping characteristics or possibly another flaw in the test. Figure 43 shows five plots of the compression specimens in their full strain range through the test. The end of these plots represents an ultimate failure point and one can see the data for specimen 3b is divergent

from the other data from the start. Compressive yield strengths were found by using a 0.2% offset elastic curve method. The average yield strength can be found in the final material properties in table 8.

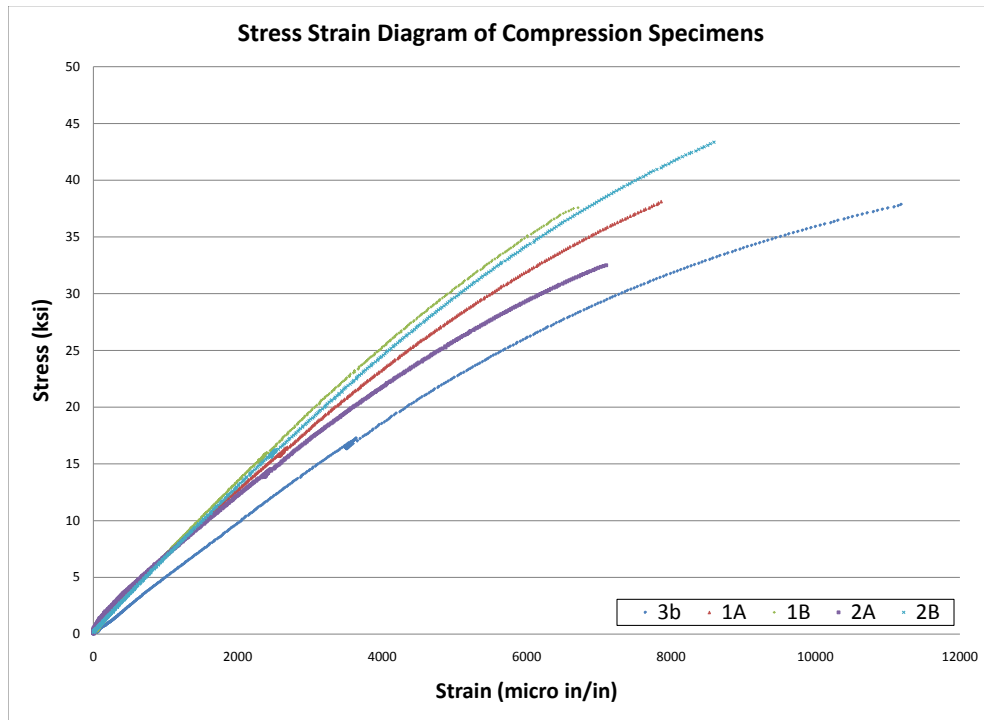


Figure 43 Compression Curves for Five Specimens from ASTM D3410

The parameter of interest from this test still remains to be the elastic modulus. To find the elastic modulus in the linear elastic region, a strain range of 1000 to 3000 microstrain was sampled as suggested in the ASTM standard. A line was fit to these data curves and the slope recorded. Figure 44 shows the four curves and the lines fit to the curves as well as equations and root mean squared deviation of the data from the linear fit. The color of the boxes around the equations dictate which equation corresponds with which curve.

All data showed excellent correlation to the linear fit. The non-zero intercept of the linear fits is acceptable since some preloading of the fixture was accomplished before a full clamp could be achieved, therefore the slope is the only relevant parameter. Table 6 shows the results of the tests and the average modulus and strength determined for the material from these tests. The average values from Table 6 are the values that will be input into the FE simulations. The fracture mechanisms of all tests were acceptable and the fractured specimens are shown in Appendix B. All fractures were due to transverse shear stresses and the shear planes were aligned with the fiber orientations across the diagonal of the material. These are classified as TMM failures according to the guidelines published at the end of the testing standard[30]. This means that the failures occurred due to transverse shear in multiple areas and through the middle of the specimen.

Table 6 Compression Test Results and Averages Used for FE Material Properties

Specimen ID	Elastic Modulus (Msi)[GPa]	Ultimate Compressive Strength (ksi)[MPa]	Bending at 2000 $\mu\epsilon$
1A	5.556 [38.31]	38.13 [262.9]	3.3%
1B	6.240 [43.02]	39.78 [274.27]	7.3%
2A	5.096 [35.14]	32.51 [224.15]	2.5%
2B	6.051 [41.72]	45.10 [310.95]	0.7%
Avg	5.736 [39.55]	38.88 [268.07]	3.4%

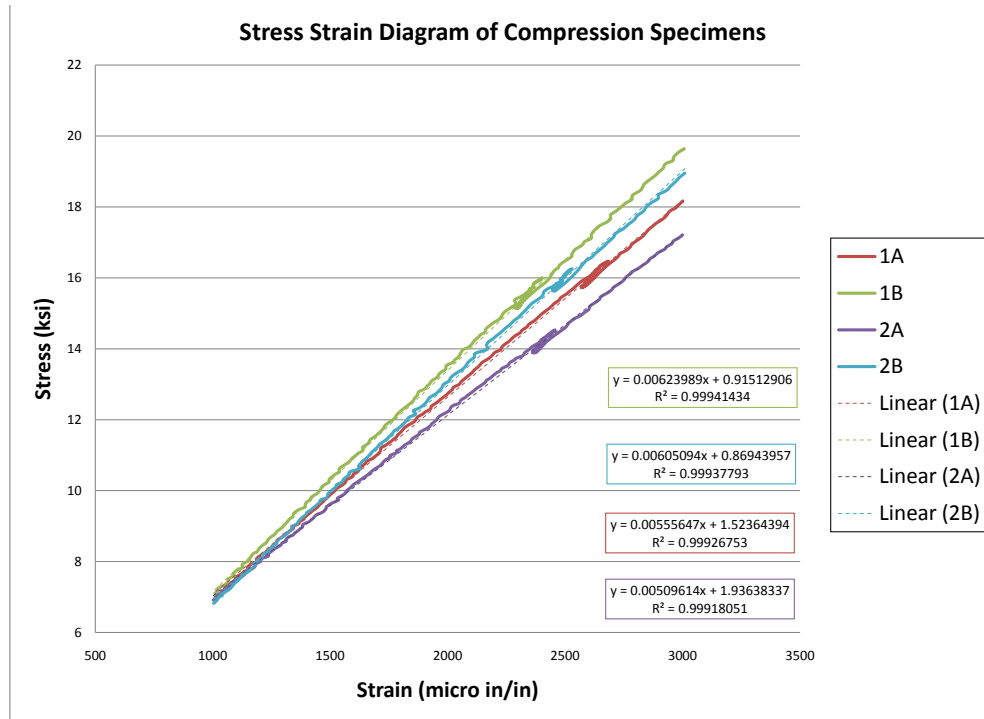


Figure 44 1000-3000 $\mu\epsilon$ Strain Range Compression Curves for Four Specimens with Linear Fits

3.1.4 Specimen Processing Details for Shear Tests. The shear test used to find the in-plane shear properties was ASTM D7078, known as the V-Notched Rail Shear test. It is a new compound test of both the original V-Notched and original Rail Shear tests. Due to large specimen sizes and limitations to non-woven fibers for the original tests, the new 7078 was chosen. This test uses bolts for a clamping force on the specimen and allows for shearing of the specimen through a simple tension force from the machine. Specimen processing for the shear tests were very similar to the processing for the compression test. The only difference in this case is that the specimen is a different shape and size. Figure 45 has the mechanical drawing of the specimen from the ASTM standard[31]. Specimen

thicknesses are not specifically required, but are recommended between 0.08 (0.002 m) and 0.2 (0.005 m) inches. There are also specific recommendations for woven fabric layups to not keep all of the layers in the same direction, but to have a $\pm 90^\circ$ layup. To keep this layup symmetric and meet the thickness requirements with minimal material, it was chosen to use twelve layers of fabric with a nominal thickness of 1.32 inches (0.034 m) in a $[0, 90]_{3S}$ layup. Again a 30% mass ratio of resin was used. The same debulking process was used with three inch (0.076 m) square fabric sheets since this was the maximum dimension attainable from the width of the splayed tube. Figure 38 shows a sheet of resin with a three inch square (0.076 m) resin section and Figure 39 shows a detail of a few debulked fabric layers on teflon paper. The specimens were run through the same debulking and layup procedures as the compression specimens, cured by autoclave, and machined by various methods from an outside contractor before being gaged.

The strain gages used for the shear tests were a special type of gage. The test procedures called for two strain gages mounted at $\pm 45^\circ$ orientations from the vertical centerline between the two notches. The gages were to be mounted at some point on that same vertical line as well as this is the region that will be experiencing the shear stresses of interest most directly. A special gage was found that has two gages pre-manufactured on top of one another in a perpendicular configuration. The gage designator is CEA-13-125WT-350. Mounting this gage in the center of the specimen at a 45° angle would accomplish both the required gages with only one adhesion process. This was a very desirable gage as it would save time in preparation as well as give strains at the same location on the specimen. One gage was mounted on each specimen at the center. Figure 46 shows a representative shear specimen with a gage mounted in its center point. One can see the

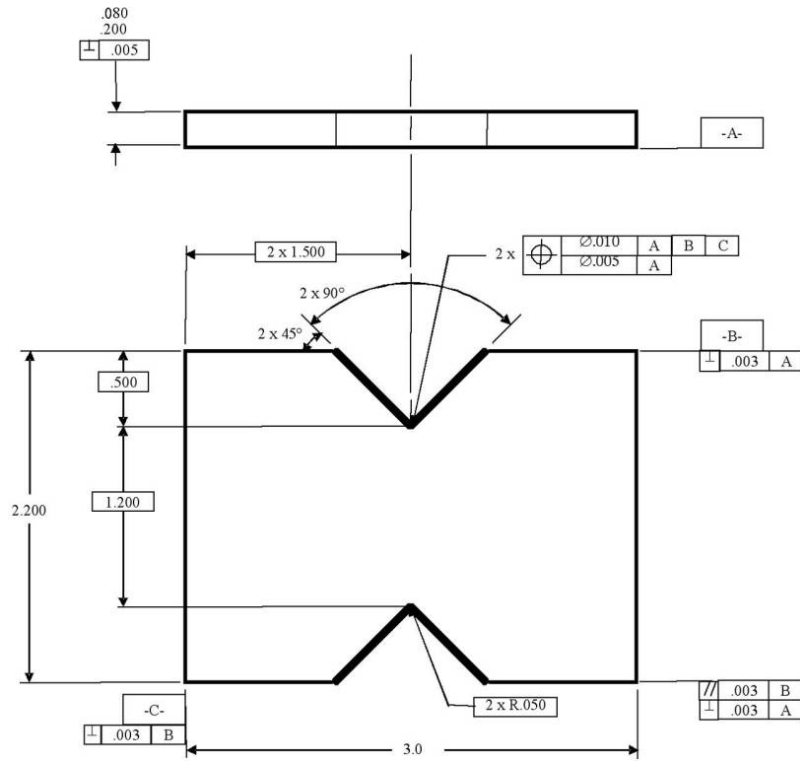


Figure 45 Shear Specimen Drawing for ASTM Test D7078

wire lead pads coming from the gage in the $\pm 45^\circ$ orientations and this is the location of each gage since the bottom one cannot be seen completely. Again the specimens were prepared by sanding to 600 grit smoothness and application of the gages achieved with M-Bond 200. The gages had wires soldered onto each lead and were connected to the same amplifier and data acquisition system as the compression specimens.

3.1.5 Shear Test Setup. The shear tests were setup as described in ASTM D7078. The shear tests were completed on an 11 kip (48.93 kN) capacity hydraulic MTS machine due to a malfunction in the previously used screw machine. The shear test fixture is comprised of two separate pieces that are not combined with each other until tightened onto a specimen. Figure 47 shows the shear fixture displayed and partially assembled. The fixtures were

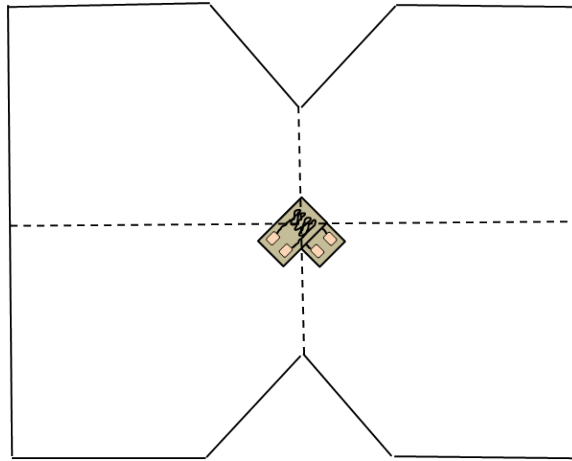


Figure 46 Shear Specimen Drawing with Perpendicular Strain Gages at Center Location

attached to the testing machine, one to the top movable head and the other to a fixed position at the bottom. Figure 48 shows the shear fixture in the testing rig without any specimen. To insert the specimen properly, one must take great care to ensure that the specimen is centered in all directions to get the desired shear stresses and not twisting that would warp the data. The fixture manufacturer provides polymer spacers that help to align the fixture in the left and right direction, but centering in the front to back direction (into and out of the page in Figure 48) can only be estimated at first then checked with some sort of measurement device. For this test, a set of digital calipers was used to check the spacing at each bolt location and the bolts on opposite sides of the fixture were loosened or tightened to adjust the spacing. Figure 49 shows a specimen that is loaded into one half of the fixture. The white polymer spacers are used to ensure spacing between the fixtures. On the top spacer, one can see the line drawn to estimate the initial bolt spacing and then the calipers are used from this point. After centering in both directions is achieved, the bolts are torqued to the appropriate value, in this case 45 foot pounds (61.01 Nm). This ensures enough clamping force to not allow the specimen to slip when testing.

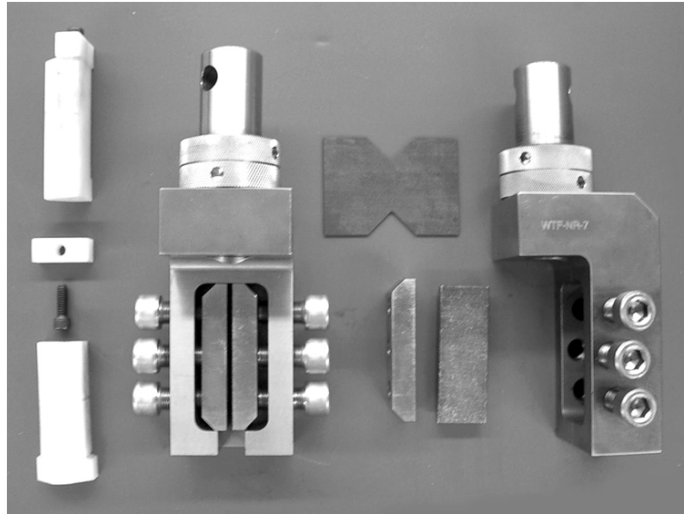


Figure 47 Shear Fixture Parts Displayed[31]

The test is accomplished by pulling the two halves of the shear fixture in tension. Each half pulling in the opposite direction will create a shearing stress at the center of the specimen in the plane of the specimen. The head speed was again set to 0.05 inches per minute ($2.117\text{e-}5$ m/s) and data collected at a rate of 5 Hz. Tests were accomplished at room temperature with a temperature of 69°F (294 K) and a relative humidity of 28%. Data recorded included the load applied, the test head displacement, the time, and the strain readings from each gage.

3.1.6 Shear Test Results. In total, five shear specimens were tested for redundancy and validation of results. The shear test data was recorded and manipulated to produce the shear stress and shear strain for easier shear modulus calculation. Since the strain gages were placed at perpendicular orientations, in order to get the shear strain, the absolute value of the two strain gage strains were summed. Figure 50 shows the entire shear data. One can see two interesting features of this data. First, specimen three breaks at a very low stress value. It was assumed that there was a possible internal flaw in the material that



Figure 48 Empty Shear Fixture Loaded into Test Frame

caused premature failure. Also, specimen five seems to double over itself. This was due to the specimen slipping in the fixture temporarily. Since the data returned to a very similar path, the slip data was removed and ignored for modulus calculations.

The shear data was not quite as tightly grouped as the compression data, but all five tests in this case agreed reasonably well. Going with the recommendations of the test procedure, the shear data for modulus calculation was taken from the 2000 to 6000 $\mu\gamma$ range. This data is shown in Figure 51 with linear curve fits to each of the specimen data. Again all data fit to the linear curve very well. Even though specimens three and five showed abnormal behavior, their shear moduli were both within the data ranges and so the data was used for shear modulus calculation. Table 7 shows the shear data and the average used

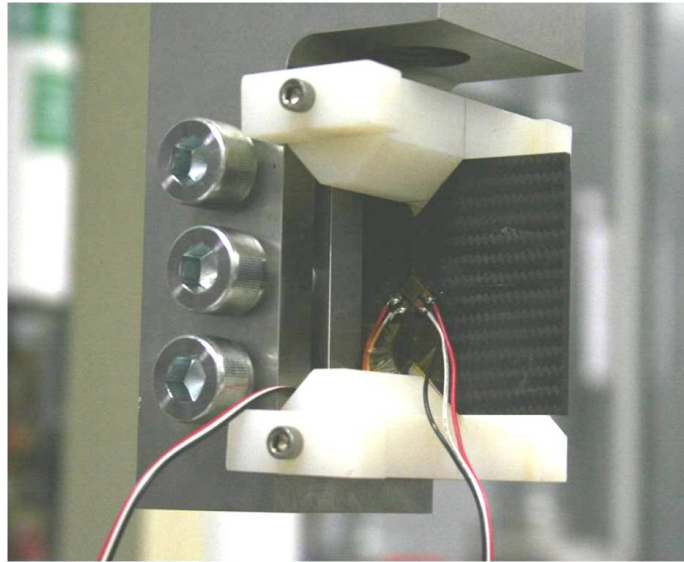


Figure 49 Shear Specimen Loaded into One Half of the Shear Fixture with White Polymer Spacers

for material property inputs in the FE models (note the (*) indicates this value was omitted from average calculations). The fracture mechanisms of all the specimens were similar in the fact that a zig-zag pattern of shear failure planes was present starting at or near the notches. In all cases but specimen 3, the failure started at one of the notch tips through shear and then a crack began to propagate through the specimen. The eccentricity caused by the crack moving to one side only then caused an asymmetric load and the crack tracked back along a similar shear plane in the opposite direction. This is an interesting result because multiple shear planes are shown for the failed specimens. Appendix C shows figures of each specimen failure and Figure 52 shows one representative failure from specimen 1.

3.1.7 Material Property Data. With all the testing complete for the material characterization, it was possible to calculate the properties for input into the FE model as described before. The final material properties are listed in Table 8.

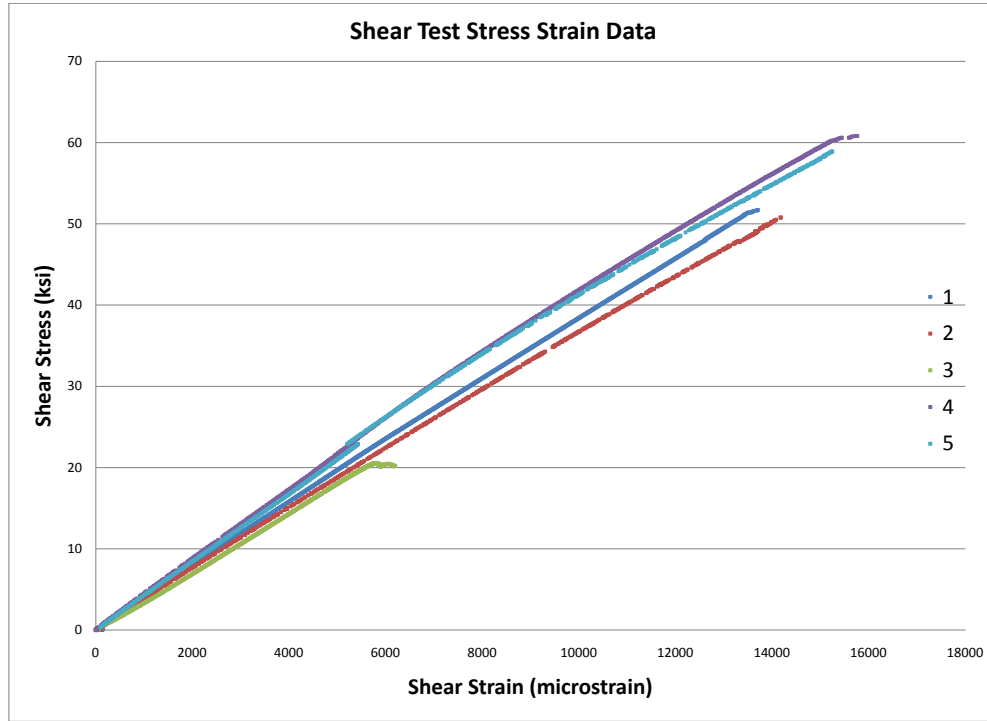


Figure 50 Raw Shear Test Stress Strain Data

Table 7 Shear Test Results and Averages Used for FE Material Properties

Specimen ID	Shear Modulus (Msi)[GPa]	Ultimate Shear Strength (ksi)[MPa]
1	3.877 [26.73]	51.71 [356]
2	3.684 [25.40]	50.79 [350]
3	3.673 [25.32]	20.57* [142*]
4	4.328 [29.84]	60.83 [419]
5	4.192 [28.90]	58.91 [406]
Avg	4.020 [27.72]	55.56 [383]

Table 8 Final Carbon Fiber Reinforced Polymer Material Properties at Waveguide Fiber Orientation

E_x	5.736 Msi [39.55 GPa]	G_{xz}	2.248 Msi [15.50 GPa]
E_y	5.736 Msi [39.55 GPa]	σ_{cy}	25.13 ksi [173 MPa]
ν_{xy}	0.06	σ_{cu}	38.88 ksi [268 MPa]
G_{xy}	4.020 Msi [27.72 GPa]	τ_u	55.56 ksi [383 MPa]
G_{yz}	3.075 Msi [21.20 GPa]		

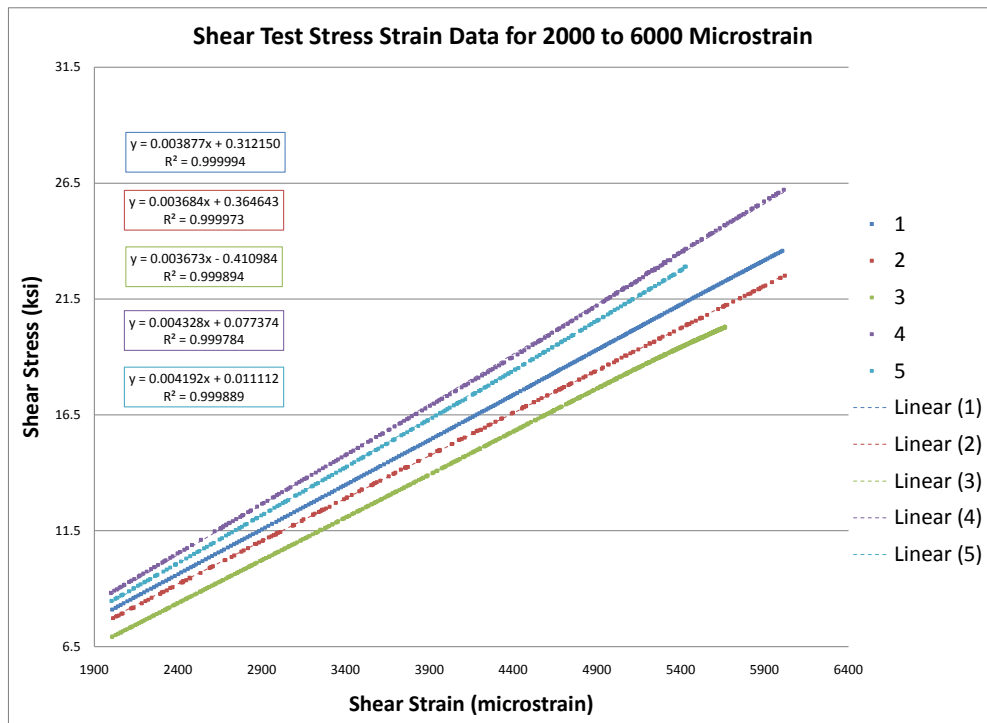


Figure 51 2000-6000 $\mu\epsilon$ Strain Range Stress Strain Curves for Five Shear Specimens with Linear Fits

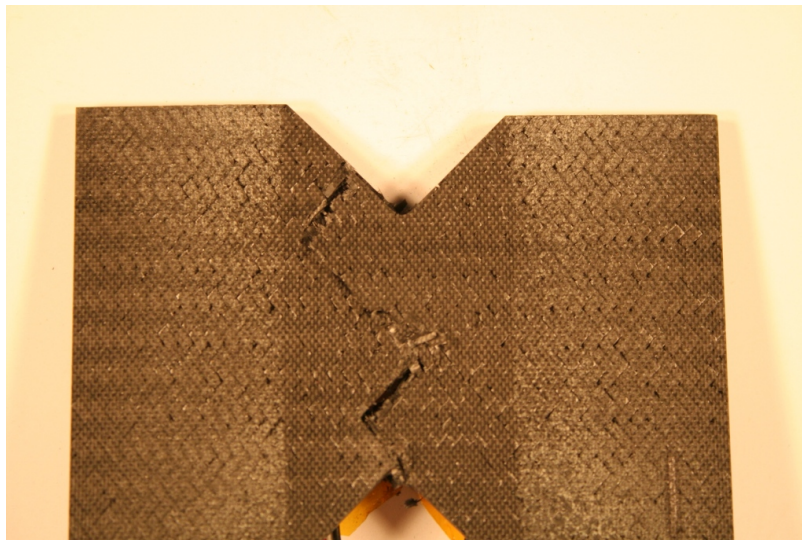


Figure 52 Representative Figure of Zig-Zag Shear Failure from Shear Tests

3.2 Waveguide Specimen Preparation

3.2.1 Description of Waveguide Test Article. The waveguide to be tested to failure in the laboratory has one of two configurations: a plain non-slotted waveguide or a waveguide with an array of five longitudinal slots cut in one wall. In this thesis the descriptions of “non-slotted” and “plain” will be used interchangeably to describe the baseline waveguide with no slots. Eight specimens were constructed with four slotted and four plain. The comparison of these two types of specimens along with comparison of the results of the finite element analysis will allow for a characterization of the change in performance caused by the slot array. In general each waveguide is an eight inch (0.203 m) long square tube made from carbon fiber reinforced plastic. The nominal inner cross sectional dimensions are 0.9 inches (0.023 m) long by 0.4 inches (0.010 m) wide with a wall thickness of 0.022 inches (0.0006 m). Each slot is one half inch (0.013 m) long at the center and is one eighth of an inch (0.003 m) wide with a rounded edge of one eighth inch (0.003 m) diameter. Figure 53 shows the waveguide drawing as sent out for the machining of the slotted waveguide. The potting material on the ends of the waveguide are for stability during the compression test. Since the waveguide will not be fixed to the compression plates of the machine at all, this potting material will provide lateral stability and a more stable platform to stand on since the walls of the waveguide are so thin. There are some inconsistencies in the actual waveguides built compared to the nominal dimensions, but all are fairly similar. Table 9 shows the cross sectional dimensions of the eight waveguide specimens.

3.2.2 Waveguide Layup and Machining. Waveguide preparation for the compression tests included layup and curing, cutting and potting, and gaging. The layup process

Table 9 Waveguide Specimen Cross Section Dimensions (All Dimensions in Inches)[mm]

Specimen ID	Inside Length	Inside Width	Broad Wall Thickness	Narrow Wall Thickness
1	0.887 [22.53]	0.380 [9.65]	0.021 [0.533]	0.027 [0.508]
3	0.885 [22.48]	0.378 [9.60]	0.025 [0.635]	0.023 [0.508]
4	0.885 [22.48]	0.384 [9.75]	0.020 [0.508]	0.022 [0.508]
5	0.886 [22.50]	0.381 [9.68]	0.022 [0.559]	0.022 [0.559]
6	0.886 [22.50]	0.383 [9.73]	0.020 [0.508]	0.023 [0.584]
7	0.885 [22.48]	0.384 [9.75]	0.020 [0.508]	0.022 [0.559]
8	0.887 [22.53]	0.385 [9.78]	0.020 [0.508]	0.022 [0.559]
9	0.885 [22.48]	0.385 [9.78]	0.021 [0.533]	0.023 [0.584]

the fabric. The inner mandrel with fabric assembly was wrapped with a sheet of resin with the desired area density then the outer mandrels were secured and this setup was placed in the debulker to transfer the resin. For the two layers of carbon fiber woven fabric, two sheets of 160 gram per square meter and one sheet of 38 gram per square meter resin were used. This left a 29.77% mass fraction of resin to fabric. The sheets were cut to the same size as the external area of the waveguide so that when wrapped around the fabric, no overlap or gaps would occur. Figures 55 and 56 show the mandrel before and after wrapping the resin sheet and Figure 57 shows the three mandrels with fabric and resin sheet wrapped, assembled, and ready for debulking. In order to smoothly transfer the resin to all four sides of the waveguide part, the assembly was set to debulk in a vacuumed state at 160°F (344 K) for five minutes on each of the four sides. If each side wasn't allowed to directly absorb heat from the bottom of the chamber (the heated portion), then the resin would not cleanly transfer to the waveguide. Once the waveguide part had been debulked with the proper amount of resin to create a 30% mass ratio of resin to fabric, the resin backing sheets were all removed and the mandrels replaced to the debulked waveguide and inner mandrel part. In order to prevent the aluminum mandrel from sticking to the resin and fabric, the

mandrels were coated in a Frekote mold release agent. This process was repeated for the desired number of waveguides, then the assemblies similar to Figure 57, but without the resin backing paper, were ready for curing in the autoclave. The same autoclave process as mentioned in section 3.1.1 was used for the waveguides as this is the standard cure cycle for the RS-36 resin.



Figure 54 Aluminum Mandrel with Two Layers of Woven Carbon Fiber Tubing Stretched Over Top

Once the waveguides were cured, they were machined to the proper specifications for testing. A total of eight waveguides were built to be tested with four being the plain non-slotted waveguides and four being waveguides with an array of five longitudinal slots. Machining included removing excess resin from the cure cycle, cutting the waveguides to length, machining slots, and applying the potting material. All work was contracted out to a local machine shop to ensure the proper tolerances required for accurate testing.



Figure 55 Fabric Wrapped Mandrel on Resin Sheet Ready for Wrapping

3.2.3 Strain Gages for Waveguides. Strain gages were again used for the data collection method for the waveguides. Two different size gages were used for this experiment since some of the areas of interest were very small and the slots would not allow for large gages. The two types of gages were CEA-06-062UW-350 and CEA-06-032UW-120. The first gage has a gage section size of one sixteenth of an inch (1.58 mm) and the second gage has a gage section of one thirty-second of an inch (0.794 mm). The smallest gages were only used at locations very close to the slot edges in order to capture stress concentrations at that location without the stress smearing across the gage section and causing false data. Gages were placed at different points on each specimen. Five specimens were gaged at first based on knowledge of FE simulation stress fields around holes and other interesting locations. The other three specimens were left to be gaged after the performance of the first batch had been noted for areas of interest. Figure 58 shows the gage locations for all eight specimens tested where the top is the front side and the bottom is the back side broad wall of the

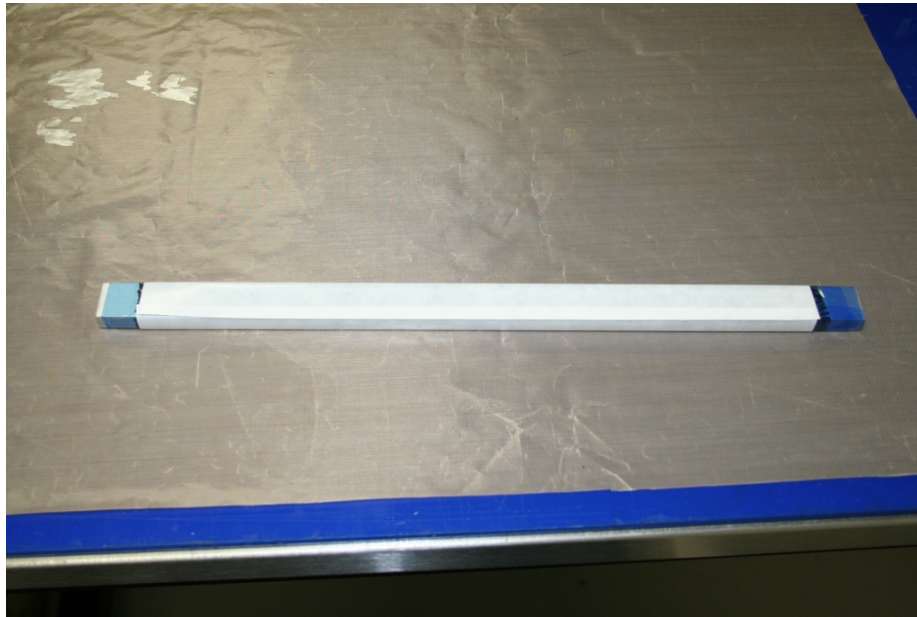


Figure 56 Fabric and Resin Wrapped Mandrel Before Outer Mandrels are Applied waveguide. Specimens three, six, and seven were the three waveguides gaged after the first round of testing. The gages are more toward the outside of the waveguide to capture some of the behavior noticed during the first round of testing.

Once the strain gages were mounted, the wire leads were attached and the specimens were ready for testing. In order to ensure that the gages were accurately attached to the specimen and the wire leads were soldered correctly, all gages were checked with a multimeter to ensure the correct resistance. The next step for strain validation was to ensure the amplifier and computer systems were reading the correct strains for a quarter bridge setup. To do this, a strain indicator calibrator was attached to the amplifier system. Strains were zeroed out based on the zero strain input from the calibrator, then the maximum strain for the gage (in all gage cases for this experiment $30000 \mu\epsilon$) was applied and the offset was changed on the software system until this was the value read on the computer. An intermediate strain reading of $10000 \mu\epsilon$ was also checked for additional accuracy. Once

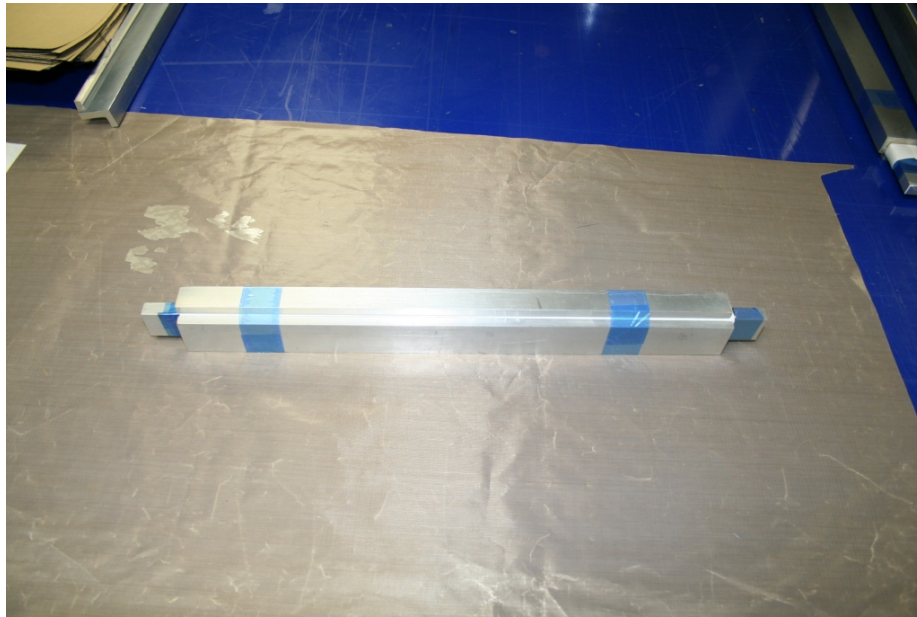


Figure 57 Full Fabric, Resin, and Mandrel Assembly

this was accomplished for each channel, then the actual strain gages were attached and the specimen was manually strained to ensure the gages were active and displaying strain on the screen. Once all strain indication values were sufficiently checked, the test was ready to run.

3.2.4 Waveguide Compression Test Setup. The waveguides were tested on the same 11 kip (48.93 kN) capacity MTS machine as the shear specimens. Two circular eight inch (0.203 m) radius compression plates were attached to the top and bottom of the machine. Again the bottom plate would be stationary while the top plate would have a velocity of 0.02 inches per minute ($8.47\text{e-}6$ m/s) applied. The speed of testing was slower for the waveguides to ensure the proper behavior was observed since the instability was so sensitive to loading. Figure 59 shows the entire test setup to include strain gage amplifier, MTS machine with compression plates and waveguide installed. The waveguide was centered

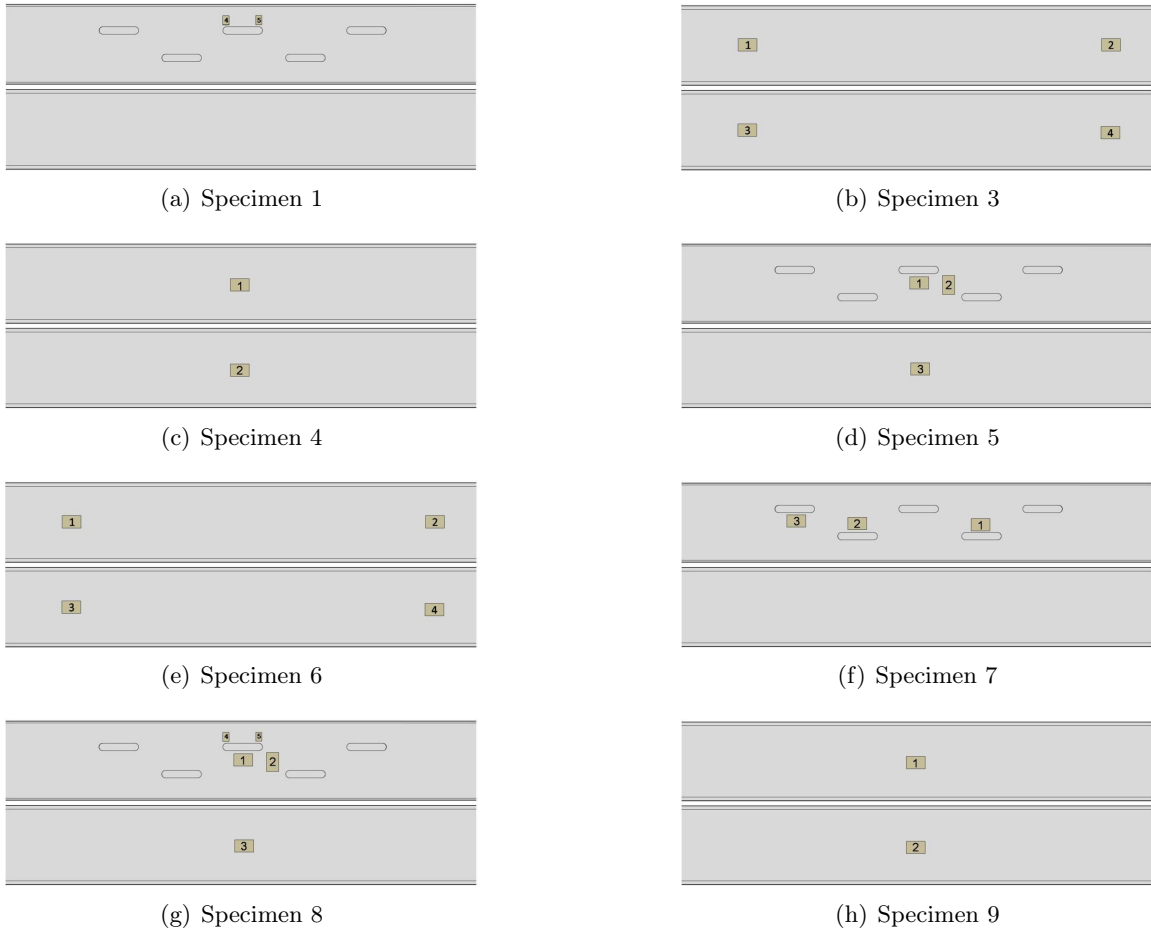


Figure 58 Strain Gage Locations for Eight Waveguide Specimens

on the plates by use of a set of rings installed on the compression plates for this purpose. The top plate did not have any rotational degrees of freedom however, so the centering of the waveguide was not critical. Once centered, a preload of about 50 pounds (222 N) was applied to hold the waveguide in place and the test was run until failure. Laboratory conditions at the time of testing were 68°F (293 K) and a relative humidity of 12%. Data recorded included the load applied, the test head displacement, the time, and the strain readings from each gage at a rate of 5 Hz.



Figure 59 Waveguide Compression Test Setup

IV. Results and Discussion

An extreme amount of data was produced from all of the experimental and finite element work that was completed. This section will present the relevant results in appropriate format and will link the experimental and numerical results together where needed. The finite element simulation results will be presented first, followed by the experimental results. Comparisons of data will follow.

4.1 Single Slot Finite Element Results

The most basic study for this waveguide system included a study of the stress and strain fields present around single slots of seven different orientations and configurations as seen in Figure 60. The angle of slots is taken from the horizontal centerline of the waveguide and so the 0° slot will be perpendicular across the waveguide. The von Mises stress fields and overall strain fields for each slot are presented in Figures 61 through 67. Table 10 shows the maximum von Mises stress and the maximum principle strain values for each slot and the length of the waveguide required for no boundary interactions as detailed in section 2.7. The stress values show the stress concentration comparisons for the slots since all waveguides have the same cross section and were submitted to the same load of 1000 pounds (4.45 kN). Results from a 2.5 inch (0.064 m) waveguide with no slots is given as well for comparison. Locations of the maximum stress and strain values can be seen in the representative figures.

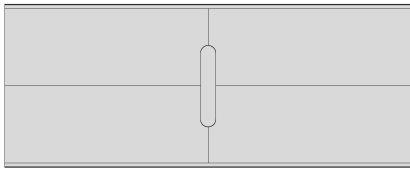
It must first be noted that some of the stress values found from the 1000 pound (4.45 kN) axial load are greater than the failure stresses of the material. What this would

Table 10 Results from Slot Configuration Tests

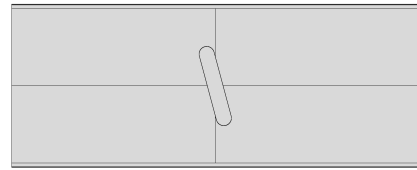
Slot	Max von Mises Stress (ksi)[MPa]	Max Strain ($\mu\epsilon$)	Length (in)[m]
0°	75.99 [524]	2864	2.5 [0.064]
15°	78.07 [538]	3345	2.5 [0.064]
30°	75.24 [519]	4311	4.5 [0.114]
45°	73.59 [507]	4272	4.5 [0.114]
90°	33.63 [232]	3289	2.5 [0.064]
H Narrow	52.76 [364]	4757	3 [0.076]
H Broad	47.26 [326]	8746	3 [0.076]
None	20.69 [143]	1174	2.5 [0.064]

indicate is that almost all of the single slotted samples would not be able to carry the 1000 pound (4.45 kN) load in a laboratory setting so the applied load would have to be decreased before any experimental testing. However, no failure criteria were implemented in the FE simulation, so the results are still meaningful from a comparison standpoint. Figure 68 shows a plot of the slot angles and the respective maximum von Mises stress with linear interpolation between the slots. This plot would seem to indicate that with a load of 1000 lb (4.45 kN), slots above 85° would allow for stresses below the ultimate failure point, but all slot angles are above the yield stress. All of the maximum stresses in the slot come at locations around the circular ends of the slot, which would indicate that the absence of material is creating a stress concentration from the necessity that the stress being carried in the wall of the waveguide must flow around the slot. The use of the rounded ends of the slot rather than sharp corners should help to alleviate this concentration. The H slots have highest stresses at the point where the slot transitions from straight walls to the round end, the same location as the longitudinal slot. The reason that the H slots have higher stress values at this point than the longitudinal slot is because the radius of the corner in the H slot is smaller. Even though the H slot has 63% of the area of the longitudinal slot, the smaller radius creates a higher maximum stress. The longitudinal 90° slot is clearly the best slot in

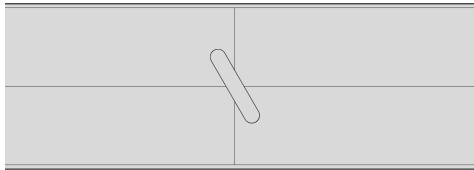
terms of stress and strain as it has the lowest values by far with the same load. In fact this slot is far greater than any other slot with only a 63% increase in stress over the non-slotted sample. The H slot in the broad wall is the only slot that comes close to the longitudinal slot in terms of stresses, but the strain values seen there may be discouraging. Since CFRP is not very damage tolerant, the strain values could cause small fiber failures which could then propagate to a whole waveguide failure. The H slot in the narrow wall also shows good stress values for a non-longitudinal slot, and the strains are of comparable value to some other slots. In terms of the influence of the stress field at a distance away from the slot, the longitudinal slot is by far the best performer, which is of prime concern when creating an array of slots in a waveguide. If another slot is used with further reaching influence in terms of stress fields, then the interaction of the stress fields from multiple slots could make the stresses even greater and of more concern. Since the longitudinal slot is the typical slot for radiating waveguides that do not carry structural loads and it is the best slot in terms of structural performance, it provides a “best of both worlds” result and should allow for great performance in a structural waveguide. One must keep in mind that this structural performance characterization only takes into account the static stress performance of the single slot in compression so much more structural testing must be completed before a final verdict can be achieved.



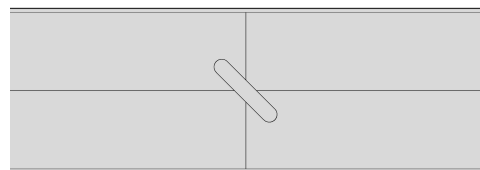
(a) Horizontal Slot



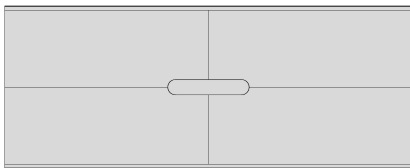
(b) 15° Slot



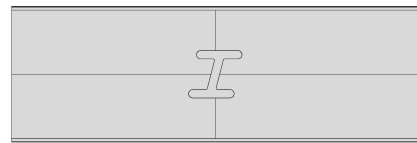
(c) 30° Slot



(d) 45° Slot



(e) Vertical Slot



(f) H Slot in Broad Wall



(g) H Slot in Narrow Wall

Figure 60 Seven Slot Configurations and Representative Figures

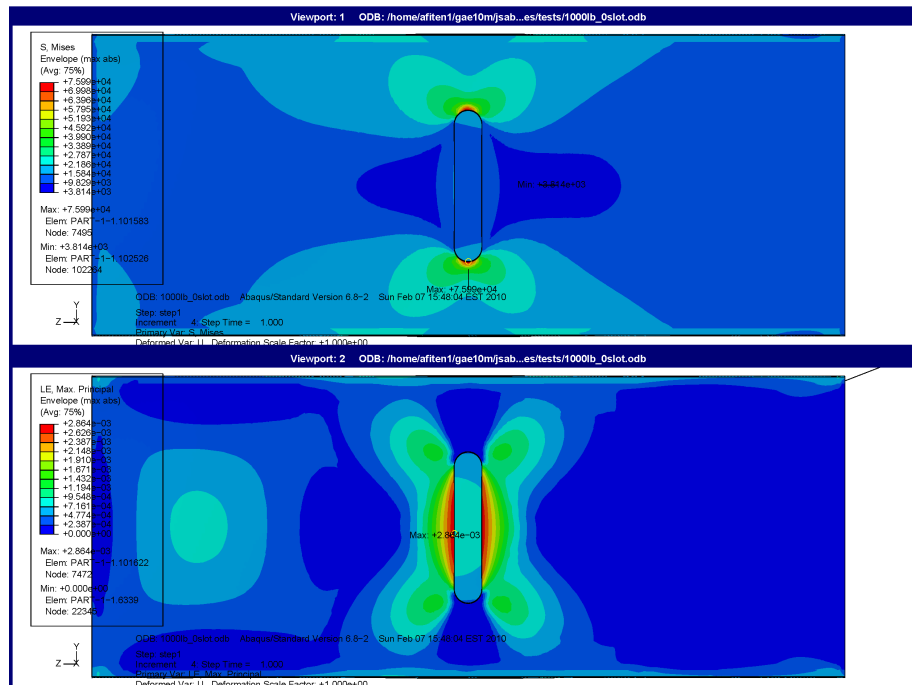


Figure 61 Von Mises Stress Field and Overall Strain Magnitude Field for 0° Slot

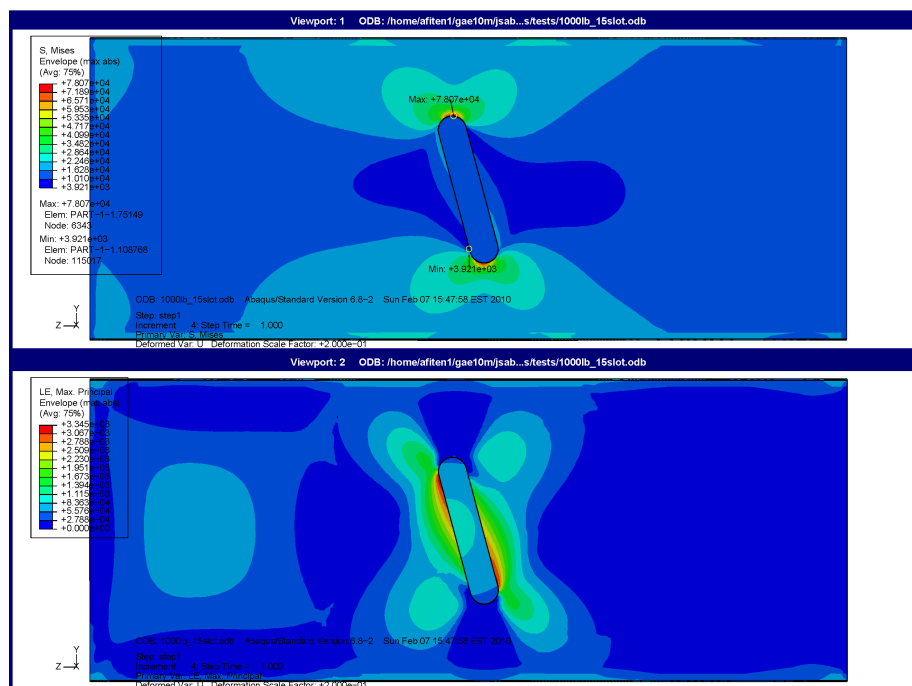


Figure 62 Von Mises Stress Field and Overall Strain Magnitude Field for 15° Slot

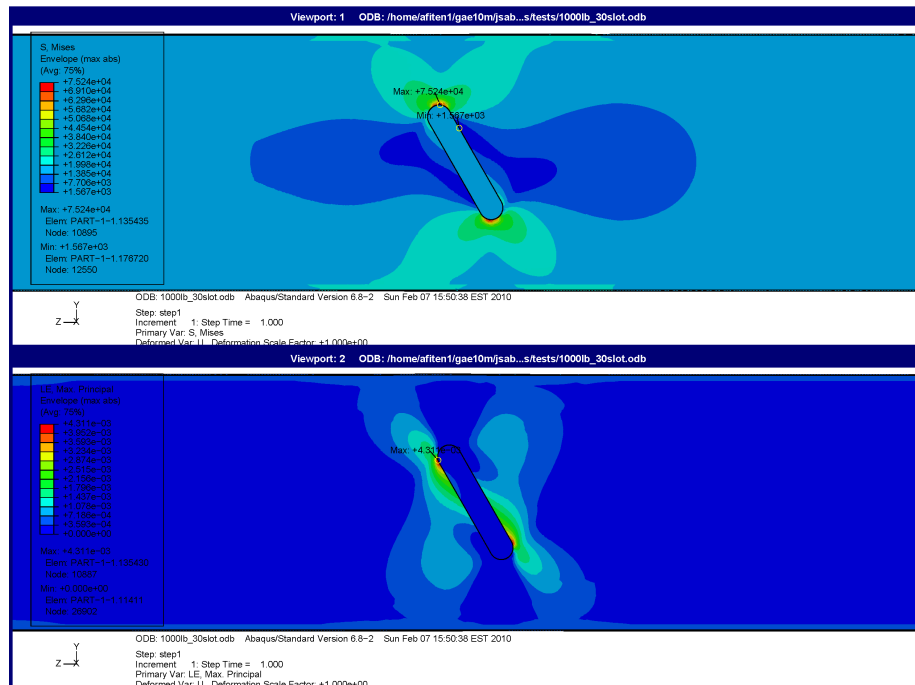


Figure 63 Von Mises Stress Field and Overall Strain Magnitude Field for 30° Slot

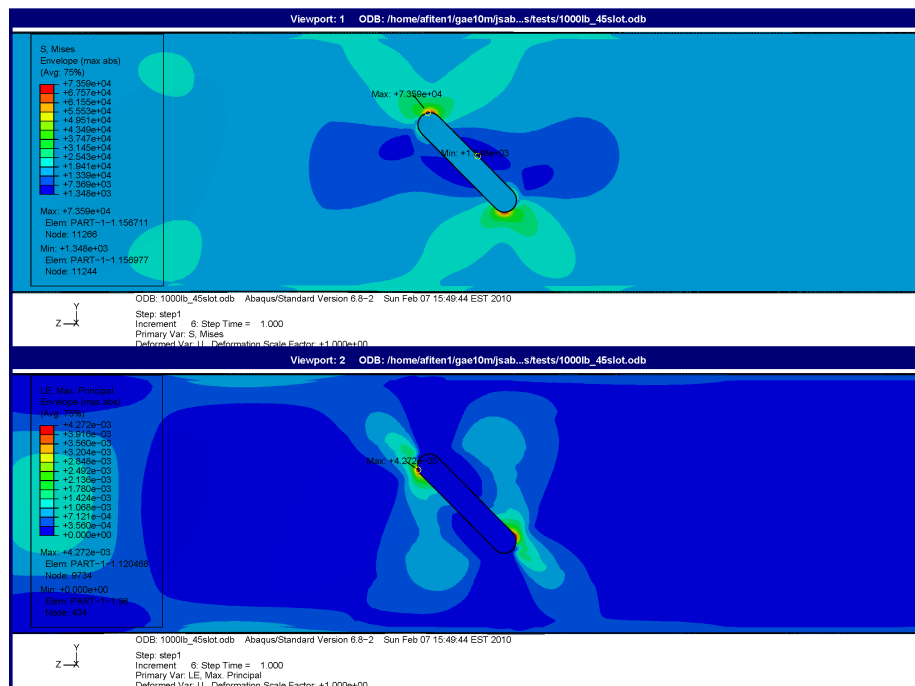


Figure 64 Von Mises Stress Field and Overall Strain Magnitude Field for 45° Slot

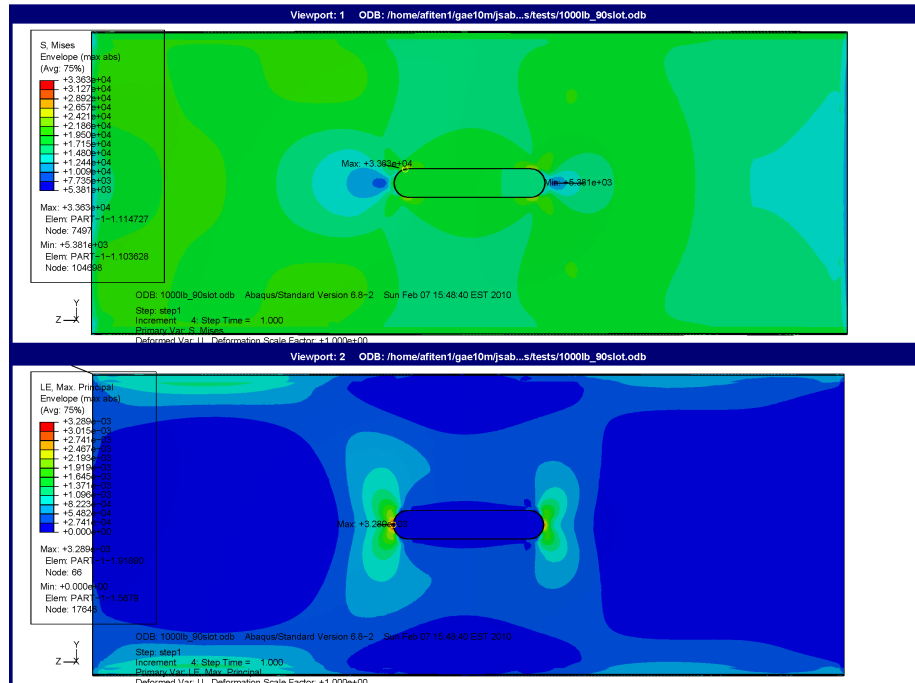


Figure 65 Von Mises Stress Field and Overall Strain Magnitude Field for 90° Slot

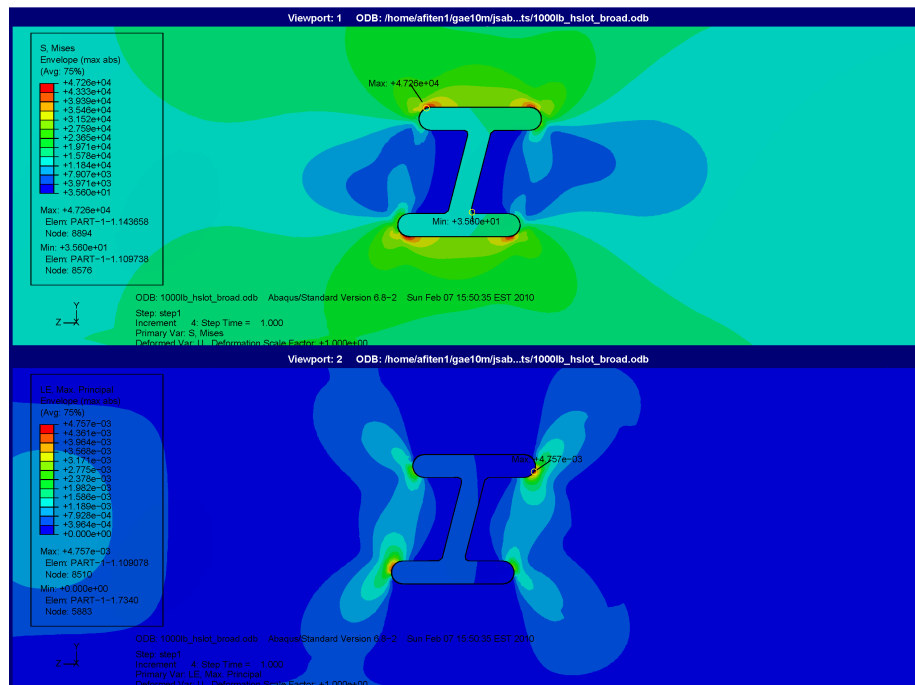


Figure 66 Von Mises Stress Field and Overall Strain Magnitude Field for H Slot on Broad Wall

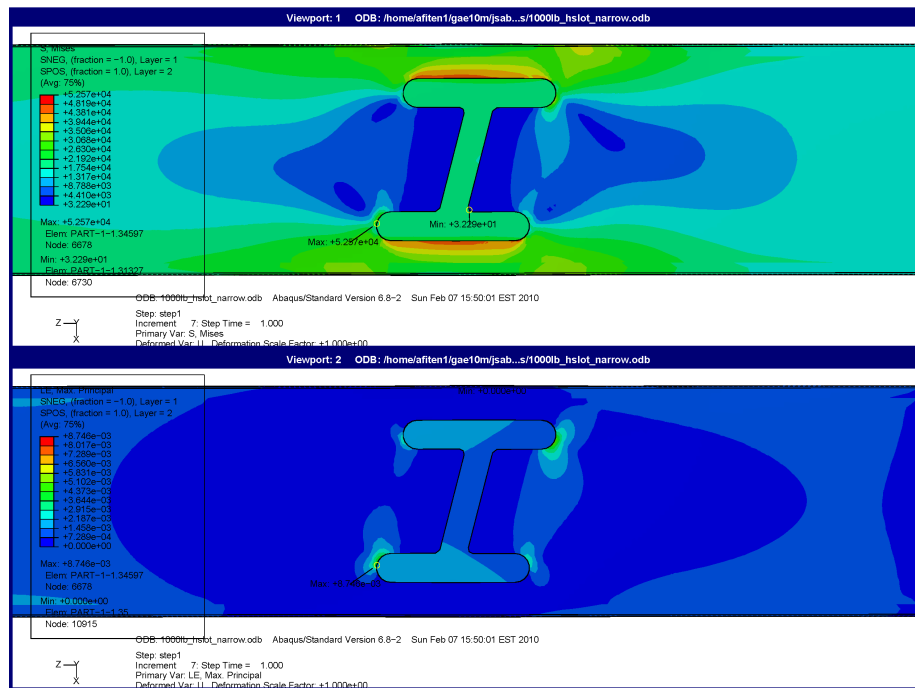


Figure 67 Von Mises Stress Field and Overall Strain Magnitude Field for H Sloton Narrow Wall

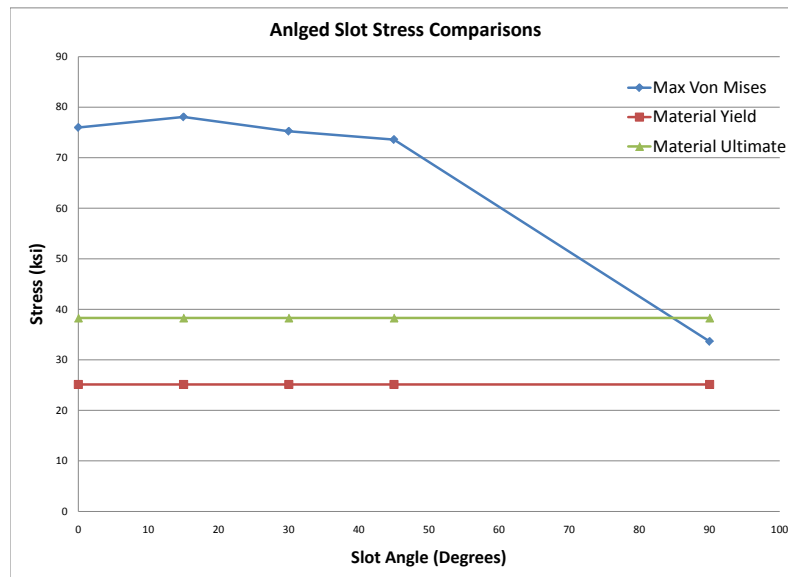


Figure 68 Stress vs Slot Angle Plot Showing Failure Limits and Slot Tip Stresses for 1000lb (4.45 kN) Load

4.2 Linear Bifurcation Results

A buckling analysis was completed on both the slotted and non-slotted waveguides. This section will present the results of each analysis completed and results will then be compared.

4.2.1 Non-Slotted Waveguide Bifurcation. The first five buckling modes of the plain, non-slotted waveguide are given in Figure 69. Each of these buckling modes was produced with a deformation scale factor of 0.3, which means that all of the displacements in the model are cut to 30% of the actual value before plotting. This was done in order to see the deformation more clearly. With higher factors, the opposite walls will protrude through each other and even with a scale factor of 0.3 some of this can be seen. In general the buckling deformations take on a form similar to a sinusoidal curve on each wall with the bulging features alternating in and out of the undeformed waveguide wall plane.

The first conclusion that must be observed from the results is the fact that no overall beam buckling is observed. The only buckling seen is local wall buckling in the form of plate buckling on each wall. When the buckling modes are compared with the buckling of a simple plate the size of one broad wall, the buckling characteristics are identical. Figure 70 shows the waveguide and the plate next to each other and it is nearly indistinguishable except for the difference in loads.

In the case that a designer would wish to increase the performance of these waveguides for stability, the most critical dimension would be the wall thickness. In the plate stiffness equation, Eq. (4), the thickness value is to the third power. By doubling the wall thickness, one can increase the initial buckling load by eight, which was confirmed by some models of

Table 11 Non-Slotted Waveguide Bifurcation Results

Model	Buckling Load (lb)[kN]
Waveguide Mode 1	938.7 [4.175]
Waveguide Mode 2	964.0 [4.288]
Waveguide Mode 3	977.2 [4.347]
Waveguide Mode 4	1009 [4.488]
Waveguide Mode 5	1032 [4.590]

0.044 inch (0.001 m) wall thickness. The buckling value of this thicker waveguide was 8.6 times the buckling value of the waveguide with 0.022 inch (0.0006 m) walls.

4.2.2 Slotted Waveguide Bifurcation. The results from the slotted waveguides will be presented similar to the results from the plain waveguides and then compared. Figure 71 shows the first five buckling modes of the slotted waveguides. Again the results show pure plate buckling locally on each wall. The slots do play a significant role in the buckling modes, however. The addition of the slot into the waveguide face essentially removes the simply supported boundary condition that the corners are enforcing on adjacent walls. Having the sides of the slot now as a free surface allows for decreased stability.

The addition of the slots clearly causes an influence on the buckling behavior. On the non-slotted waveguides, the bulging areas of the waveguide wall for the first eigenvector seemed to have arbitrary size and placement and dissipated further from the location of the load application. The first eigenvector for the slotted guide does not show this feature, but seems to have the strongest out of plane displacement at the center slot of the waveguide. This center slot is surrounded by other slots which create weak zones in the waveguide and allow for the maximum displacement to come at the center slot. The out of plane displacements for the slots are also not symmetrical about the longitudinal centerline. The

slots are all offset from the centerline and the side of the slot that has the broadest wall seems to be the side that bows the most. This is as expected since the plate buckling equation divides by the width of the plate to the second power. The slots show a similar pattern as the plain waveguides in that the slots alternate tensile and compressive out of plane displacements at each slot for the first eigenvector.

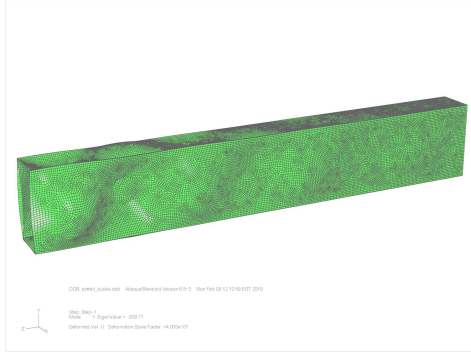
Table 12 shows the buckling values of the first five modes of the slotted waveguide and the percent decrease from the plain waveguide. For both the slotted and plain waveguides, the buckling values of the first five modes are all within a fairly tight range ($<141 \text{ lb [627 N]}$). This is an interesting result because if the waveguide can structurally support the loads experienced in the initial buckling mode, then the loading may continue to increase on the waveguide and multiple buckling modes may be experienced. In a rapid loading situation such as an aircraft maneuver, the snap-through of the different buckling modes would most likely cause poor performance structurally and electrically, if not overall failure.

Table 12 Slotted Waveguide Bifurcation Results

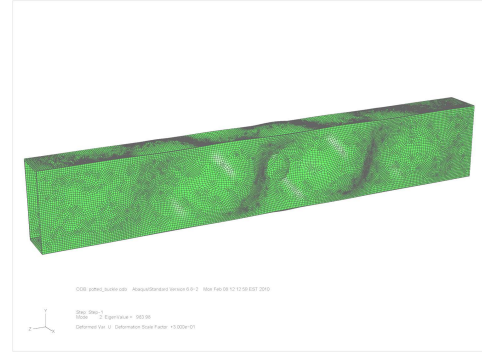
Model	Buckling Load (lb)[kN]	Percent Drop from Non-Slotted
Waveguide Mode 1	863.3 [3.840]	8.0%
Waveguide Mode 2	912.9 [4.060]	5.3%
Waveguide Mode 3	944.9 [4.203]	3.3%
Waveguide Mode 4	972.2 [4.325]	3.6%
Waveguide Mode 5	1004.7 [4.469]	2.6%

Overall, the bifurcation results of the slotted waveguides do not show a significant drop in the buckling loads. In fact the greatest decrease is the load for the first eigenvector of 8%. The slots seem to significantly affect the shapes that the buckling takes on, but the loads where the instability is experienced is not very far from the reference. The back walls of the waveguide resemble the non-slotted waveguide and also show out of plane

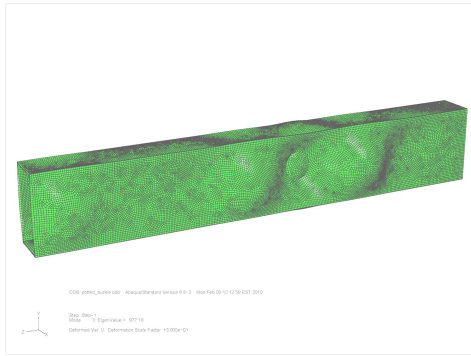
sinusoidal displacement. The removal of the material for the slots is a reduction of 5% of the area on the broad wall of the waveguide and the buckling values fall on the same order of magnitude, so it can be concluded that the buckling results of the FE analysis show favorable characteristics of the slot array.



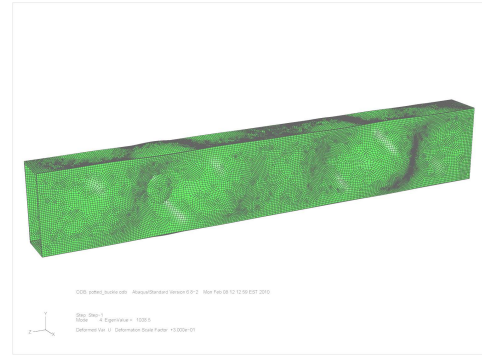
(a) Eigenmode 1



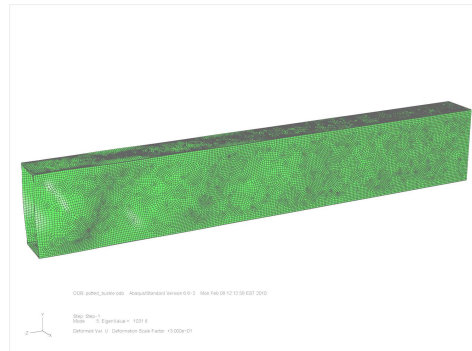
(b) Eigenmode 2



(c) Eigenmode 3



(d) Eigenmode 4



(e) Eigenmode 5

Figure 69 Bifurcation Eigenvectors for the First Five Eigenmodes of the Non-Slotted Waveguide

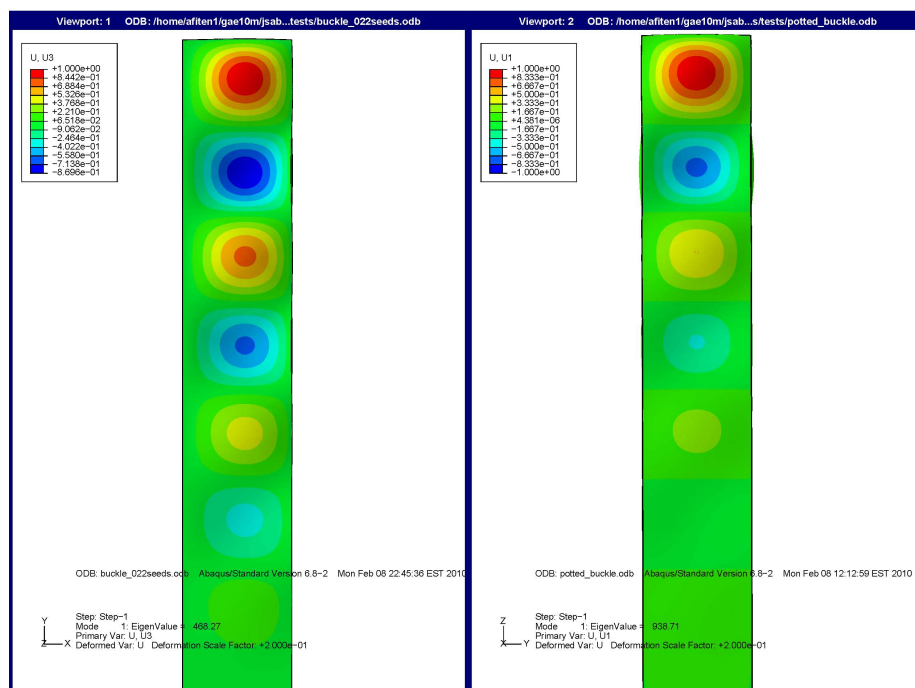
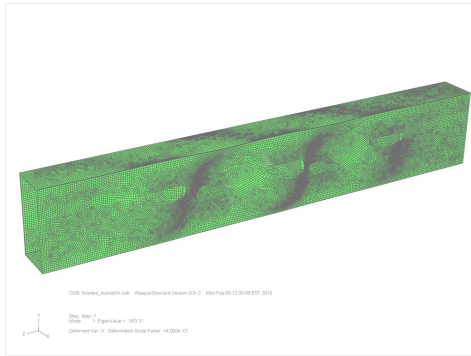
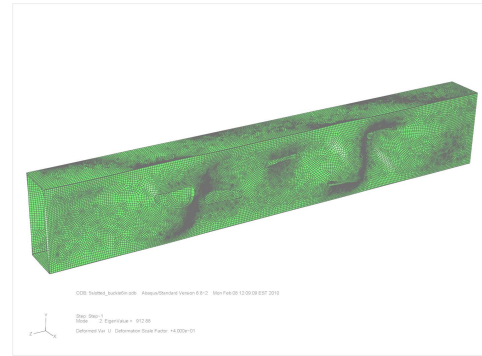


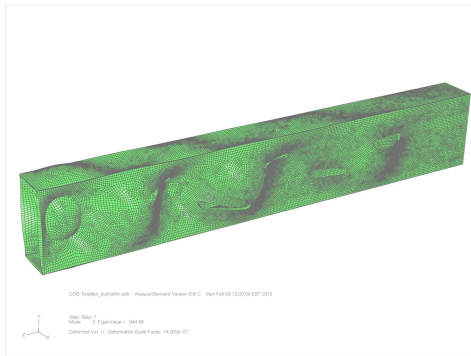
Figure 70 Comparison of Single Broad Wall Plate Buckling Mode with Plain Waveguide



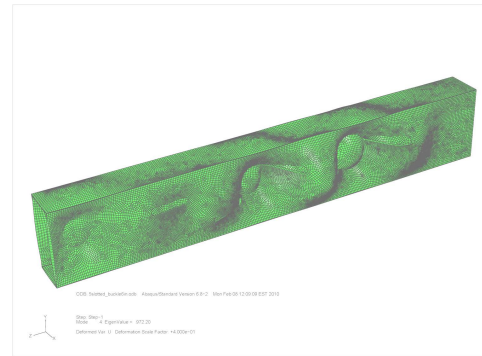
(a) Eigenmode 1



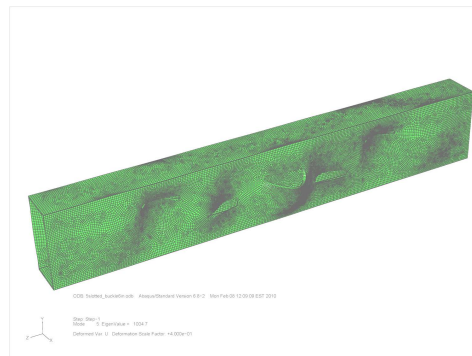
(b) Eigenmode 2



(c) Eigenmode 3



(d) Eigenmode 4



(e) Eigenmode 5

Figure 71 Buckling Eigenvectors for the First Five Eigenmodes of the Slotted Waveguide

4.3 *Nonlinear Instability Results*

The linear bifurcation results from above are valuable to compare performance and get an initial feel for the behavior of the waveguide, however, the nonlinearities present in the slotted waveguide would require a nonlinear analysis for a full representation of the limit load behavior. The results of the Riks instability procedures are presented here for slotted and unslotted waveguides and comparisons are made.

4.3.1 Non-Slotted Waveguide Nonlinear Instability Results. The nonlinear Riks analysis of the plain waveguides was not a straight forward setup. All non-slotted waveguides were required to have an imperfection applied before a Riks analysis could be accomplished. Since the waveguides did not have any nonlinear features to begin with, the nonlinear Riks approach would give poor results without some imperfection. Again the specific imperfection that was applied was equal to 0.01% of the displacements from the first eigenvector as detailed in section 2.5. Figure 73 shows the equilibrium stress displacement path for the plain six inch (0.152 m) waveguide at a node location just inside the top boundary in the middle of the broad wall. Figure 72 shows the node location. The two curves represent the inner and outer layers of the waveguide and since these depart from each other at the instability point, one can say that bending is occurring to produce tensile forces on one side of the wall and compressive forces on the other. Since the inside wall is the wall that sees increased von Mises stress, one can assume that this wall is in compression. The waveguide was already seeing an overall compressive force and so addition of compression would increase the magnitude of the von Mises stress whereas the introduction of a tensile force would act to negate the current compressive stress and restore the waveguide in the

direction of a condition of zero loading. The fact that the stress is greatly increasing without the addition of significant axial displacement also indicates local wall buckling.

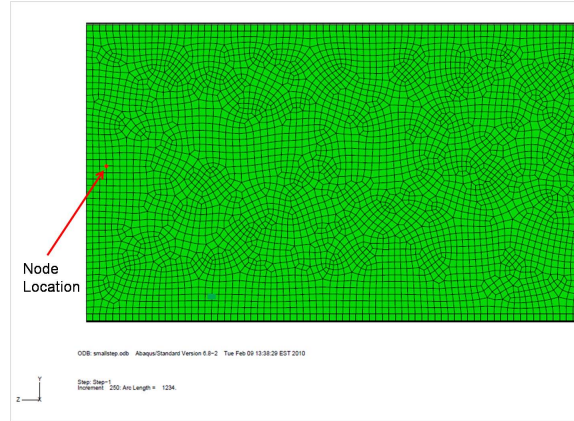


Figure 72 Node Location for Extraction of Stress and Displacement Data

The waveguide is clearly subject to instability just based on the data that is shown in Figure 73 where the curves show good agreement then suddenly snap and diverge from each other. Contour plots of the stress and displacement in the waveguides at key locations show the same result. Figures 74 through 76 below show three important locations along the equilibrium path and they indicate a point where no instability has occurred and only axial compressive stresses and displacements are seen, the point of limit load where buckling begins, and a point near the end of the analysis where full instability has occurred respectively. It is not possible to see in the figures, but all displacements are symmetric as the front and back and both side walls each displace the same as the opposite wall.

The results show many similarities to the bifurcation results in the fact that only local wall buckling is seen and no global column buckling occurs. The plate starts to buckle in the walls similar to the eigenvector buckling, but the buckling shapes seem to have more symmetric features about the waveguide lateral centerline than the first buckling eigenvector.

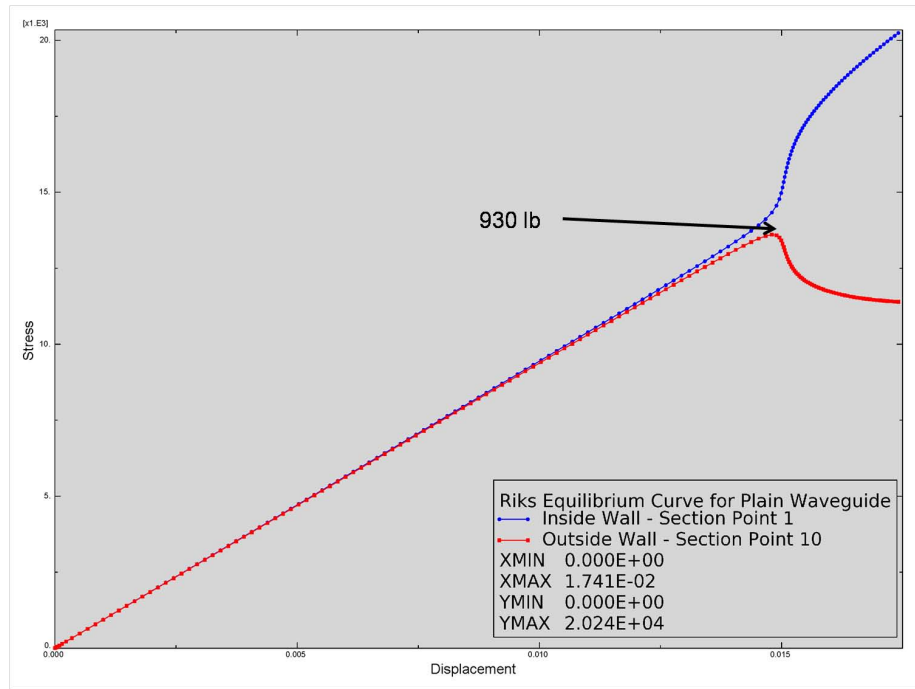


Figure 73 Nonlinear Riks Stress Displacement Curve for Plain Waveguide with Imperfection

This is a more similar shape to the buckling results of the slotted waveguide. Table 13 gives some of the pertinent loading information from the Riks analysis. Figure 77 also shows interesting behavior of the extreme out of plane displacements when instability occurs. The figure shows the out of plane displacement plotted along a path down the centerline of the waveguide. The nearly flat line in the center is the displacement at an early load where the only curvature comes from the initial imperfection applied to the waveguide. The next curve is the displacement plotted along that same path at a load of slightly more than twice the initial load. At this point the load has doubled and the out of plane displacement has increased by about five times. The next curve is the displacement plotted just a few frames after the middle curve where the load has only increased by about 100 pounds (444 N) or 12%, but the displacement has increased by about 300%. This result shows that once

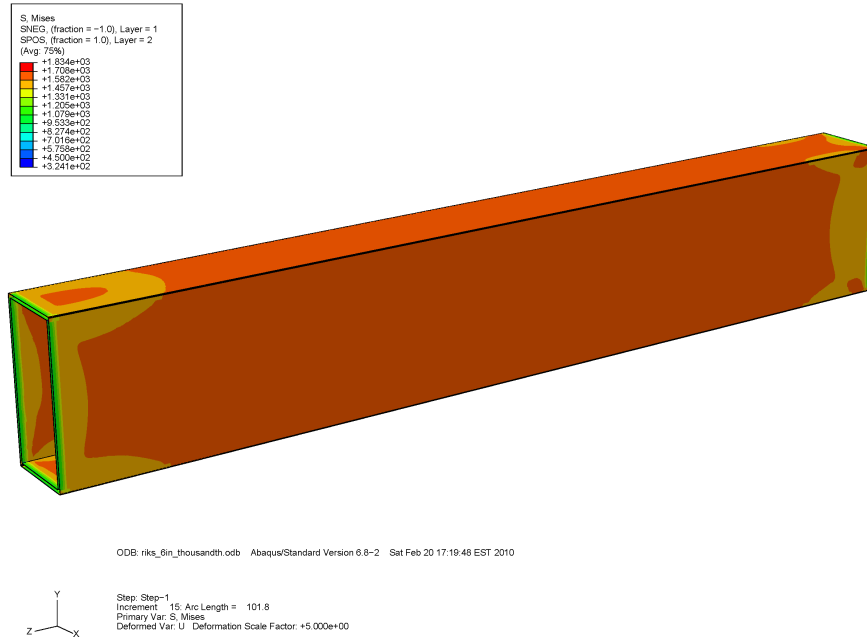


Figure 74 Von Mises Contour Plot on Deformed Waveguide Before Buckling (Load=102 lb[453 N])

the localized instability is reached, the snap through occurs very quickly and very large displacements can be seen with only very small increases in the loads.

Table 13 Plain Waveguide Riks Results

Case	Critical Load (lb)[kN]
Riks Limit Load	930 [4.137]
Compressive Material Failure (von Mises)	1100 [4.893]
Compressive Material Failure (Min Principle)	1170 [5.204]

These results show a couple of interesting features. The limit load is very close to the bifurcation load (1% higher) and so this means that there were not many nonlinearities present which is true since the only imperfection was manually added. The fact that the material fails under compressive stresses after the limit load is also a meaningful result. This shows that the waveguide will experience some buckling before the material eventually fails. This could be important if the waveguide can still emit radar energy in a buckled

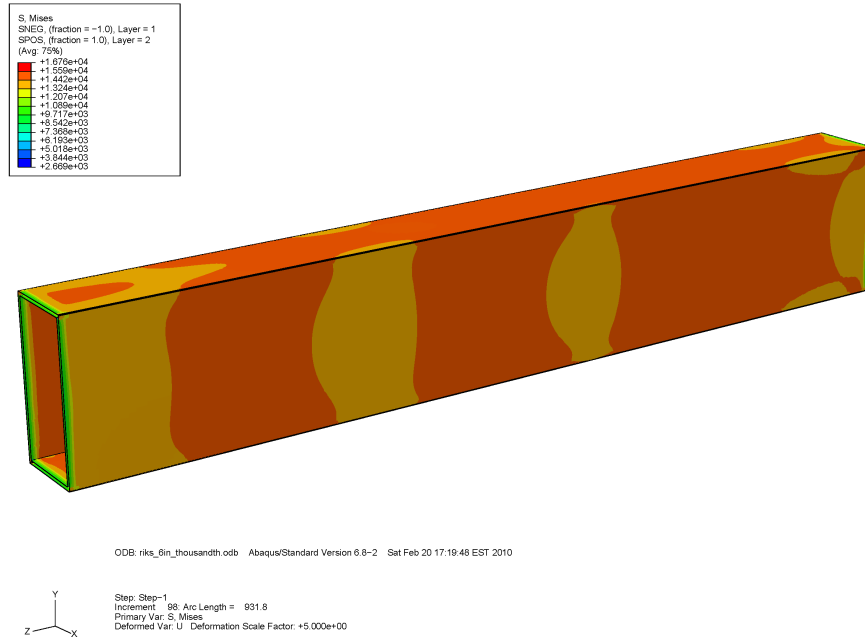


Figure 75 Von Mises Contour Plot on Deformed Waveguide at Point of Buckling (Load=930 lb[4136 N])

state, but can return to a state of no deformation when the load is alleviated. If buckling is allowable, then the operational limit loads of the system can be increased. The fact that all of the loads are so close, however shows that many different behaviors are all affecting the waveguide in a range of loading of about 100 pounds (445 N) or so. Any expectation of the waveguide to carry structural loads in this region of mixed buckling and limit load snapping is not appropriate.

4.3.2 Slotted Waveguide Nonlinear Instability Results. A nonlinear Riks approach was also carried out on the slotted waveguides. No imperfections were added to the slotted waveguide since the slots were only placed in one wall it would create an asymmetric arrangement and create moments and nonlinear geometric effects from the beginning of the analysis. A similar node location as shown in Figure 72 was used for the slotted waveguide.

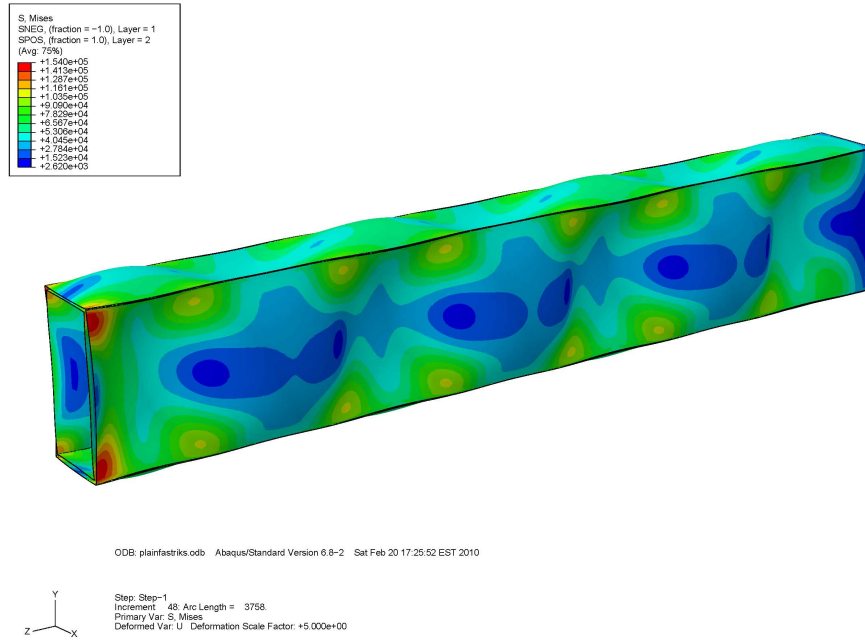


Figure 76 Von Mises Contour Plot on Deformed Waveguide After Significant Buckling (Load=2010 lb[8940 N])

Figure 78 shows the stress displacement equilibrium curve generated from this node location through the Riks analysis. A very similar result is seen when compared with the result from the non-slotted waveguide. The inner and outer walls both absorb compressive forces in the linear elastic region at first, until a snap through buckling event occurs and the walls begin to experience bending. The same feature is seen where the wall seems to be bowing out since the inner wall is seeing greater compressive forces as the solution progresses through the instability. Three figures at similar points to the three figures from above are shown below as Figures 79 through 81. The back wall of the slotted waveguide has sinusoidal buckling shapes very similar to the shapes seen on the plain waveguide.

Again the slotted waveguide nonlinear instability results are very similar to the slotted linear buckling results because the walls exhibit only local plate buckling at the slots and

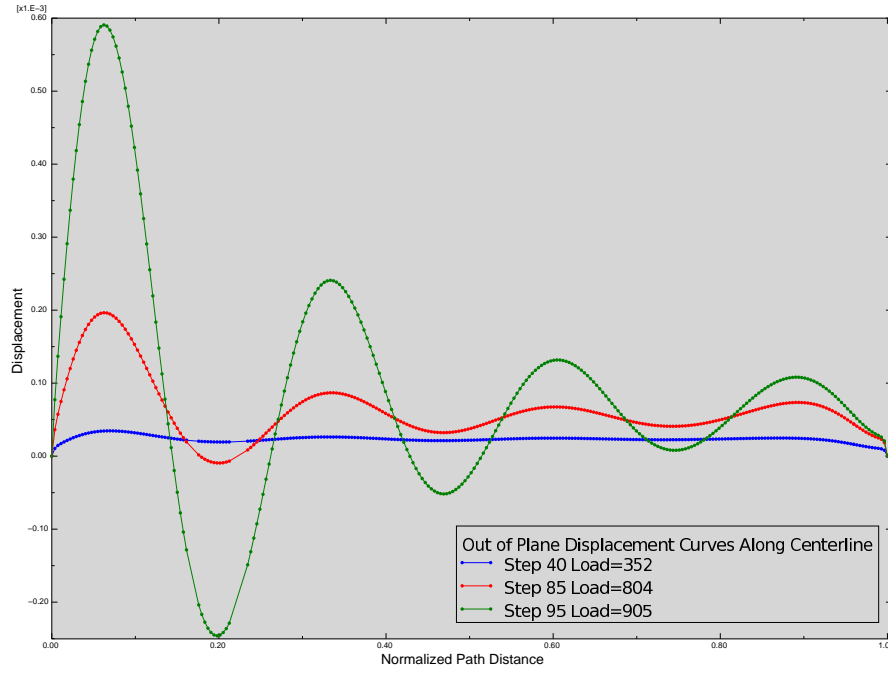


Figure 77 Out of Plane Displacement Curves Showing Large Deformations During Instability

no column buckling is seen. The out of plane displacements occur at the slots once again because that free surface allows for much easier displacement and so when the structure buckles to dissipate the strain energy, this is the easiest way to accomplish it. One interesting difference is that in the buckling simulations, the three slots across the top were bowing outward whereas in the Riks analysis the bulging is the inverse and the two slots on the bottom are the ones that are bowing outward. This could be due to the tendency for the entire slotted wall to crumple inward since the back wall is much stronger without the slots cut in it. This inward buckling motion tilts the three slots towards inward bulging and this crumpling of the waveguide with a concave feature on the slotted wall occurs. Table 14 shows the results of some critical load values from the slotted Riks analysis and a comparison with the plain waveguide values.

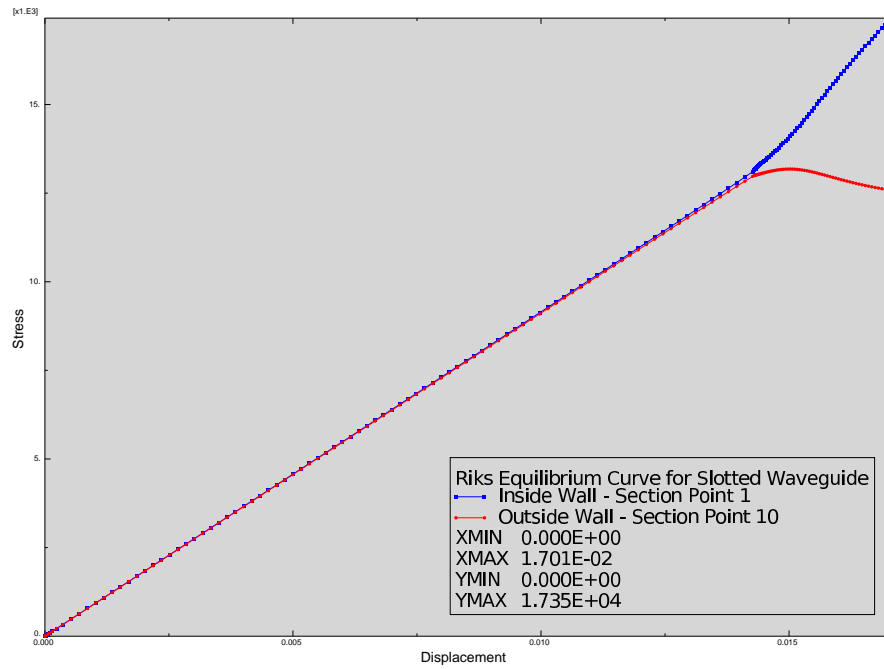


Figure 78 Nonlinear Riks Stress Displacement Curve for Slotted Waveguide

Table 14 Slotted Waveguide Riks Results

Case	Critical Load (lb)[kN]	Percent Drop from Plain Imperfect
Riks Limit Load	864 [3.843]	7.6%
Compressive Material Failure (von Mises)	948 [4.217]	13.8%
Compressive Material Failure (Min Principle)	948 [4.217]	18.9%

The first bit of data that stands out is the large drop in compressive material performance. This has a very simple explanation in the fact that the waveguide walls for the plain waveguide experience bending, but are supported by some boundary condition all around and so the large movements or stresses in those areas are shared throughout the entire waveguide. For the slotted configuration, when the slots displace out of the wall plane then the axial compressive stress is combined with an unrestrained bending stress since the slot walls have an unrestrained surface along their length so larger deformations

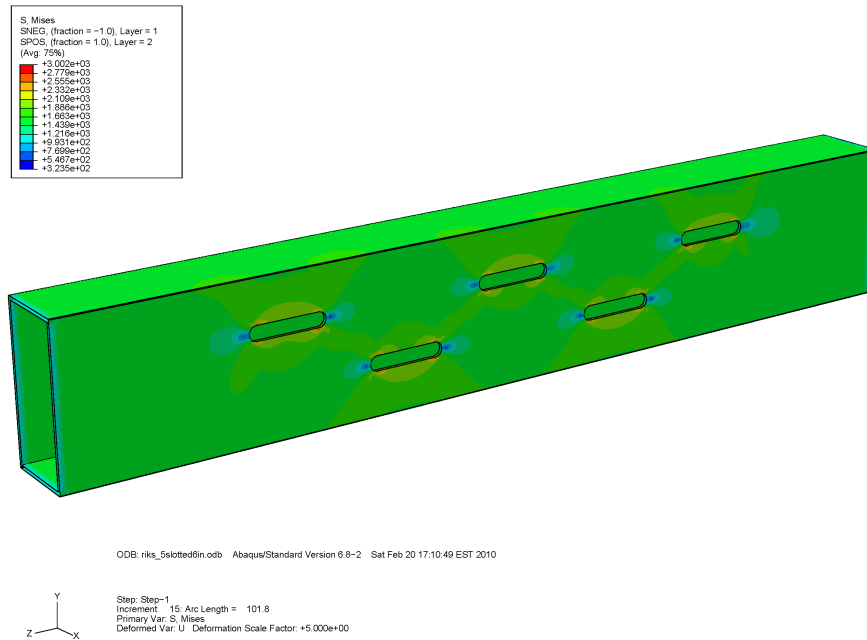


Figure 79 Von Mises Contour Plot on Deformed Waveguide Before Buckling (Load=102 lb[453 N])

are possible and the stress must be absorbed by the material at the slot wall since it cannot flow to any adjacent elements. Figure 82 shows a comparison plot of the Riks equilibrium curves for the slotted and non-slotted waveguide. One can see that the slotted waveguide has a more shallow slope from the beginning, indicating a larger imperfection at the start of the analysis. The fact is that real life waveguides will have inherent imperfections in the material or construction no matter how much care is taken during processing and so the limit loads should be given a cushion and loads in the 850 pound (3.78 kN) range for the slotted waveguide must be avoided.

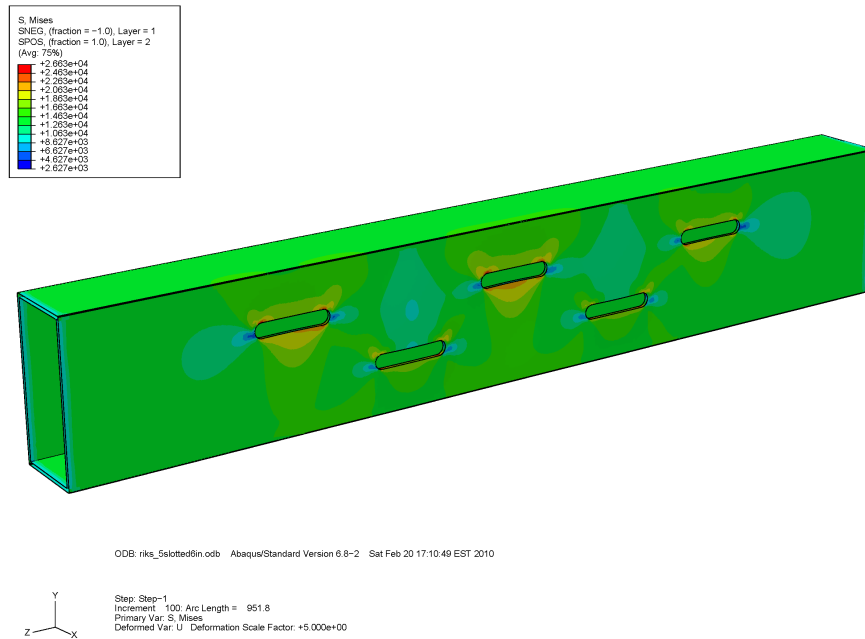


Figure 80 Von Mises Contour Plot on Deformed Waveguide at Point of Buckling (Load=875 lb[3892 N])

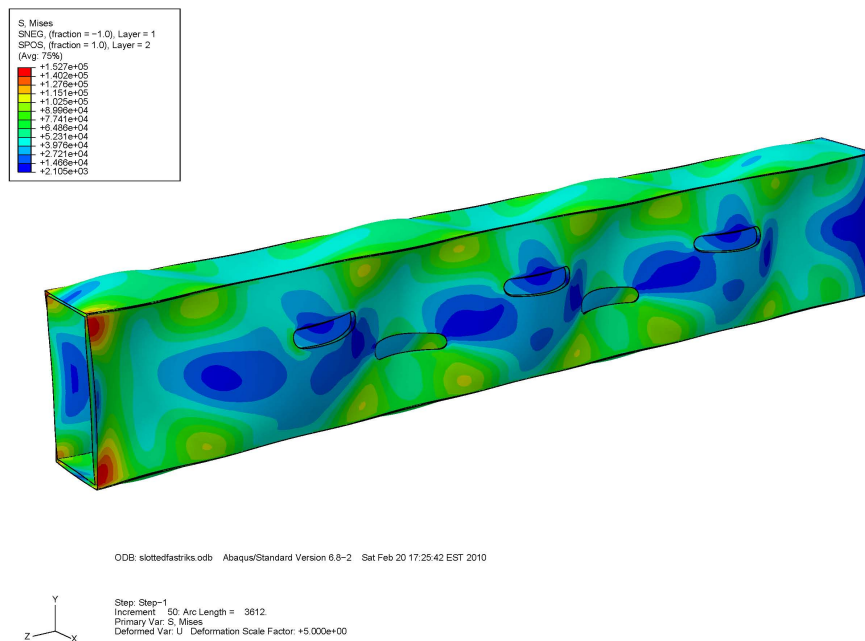


Figure 81 Von Mises Contour Plot on Deformed Waveguide After Significant Buckling (Load=2000 lb[8896 N])

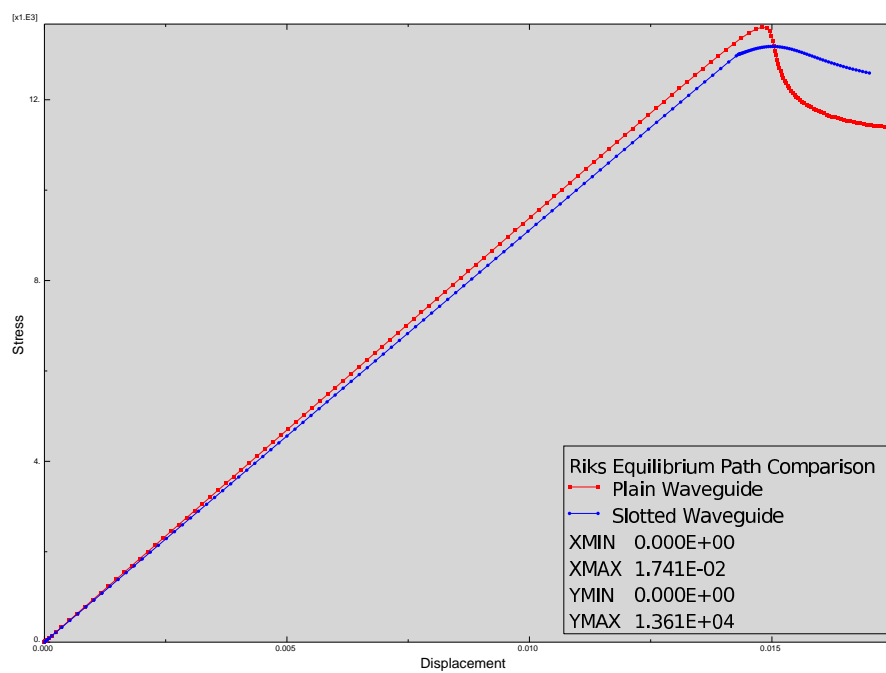


Figure 82 Nonlinear Riks Analysis Curves for Plain and Slotted Waveguide

4.4 Experimental Results

Of the eight specimens built for laboratory testing, seven tests produced meaningful data. When loading specimen nine, an accidental very high load was applied to the specimen for an instant that snapped the waveguide and no strain data was collected. The other seven specimens had meaningful tests and the waveguides were loaded until failure. Table 15 show the limit loads from the lab for the seven tests. The method of failure for all the waveguides was very similar among the groups of slotted and non-slotted.

Table 15 Results from Waveguide Laboratory Tests

Specimen	Instability Load (lb)[kN]	Max Load (lb)[kN]
1 (Slotted)	660 [2.936]	1053 [4.684]
3 (Plain)	720 [3.203]	1077 [4.791]
4 (Plain)	740 [3.292]	1077 [4.791]
5 (Slotted)	680 [3.025]	980.0 [4.359]
6 (Plain)	None	1088 [4.840]
7 (Slotted)	620 [2.758]	980.3 [4.360]
8 (Slotted)	600 [2.669]	1026 [4.564]
Plain Avg	640 [2.847]	1080 [4.804]
Slotted Avg	730 [3.247]	1010 [4.493]

The data compares fairly well with all of the numerical simulations. The average failure point for the plain waveguides was 1080 pounds (4.804 kN) and the predicted material failure value was 1140 (5.071 kN) for a difference of about 5.5% which is a very reasonable value for laboratory experiments. When comparing instability loads, the Riks analysis overpredicted the stability of the plain waveguides by 31%. This is due to the inherent imperfections in the material, loading, and geometry that combine to have a dramatic effect. The lab waveguides experienced unstable shapes far before the ultimate load was reached. The FE models predicted the degradation of the slots to be in the area of 10%, depending on which method of comparison. The lab experiments predicted similar degradation of 14% with

respect to the instability load and 7% with respect to the ultimate load. It is evident that the slots have a stronger effect on instability than ultimate performance again due to the free wall boundary condition at the slot wall.

The wall buckling of waveguides was seen in the lab and the figures below will show some of the lab performance. The plain waveguides showed the local plate buckling features just as predicted by the FE results. Figure 83 shows a plain waveguide in the compression fixture with the sinusoidal deformation on the broad walls just as predicted. Figure 84 shows a side view of the buckling feature on the non-slotted waveguide and again one can see the out of plane deformation of the broad wall clearly.

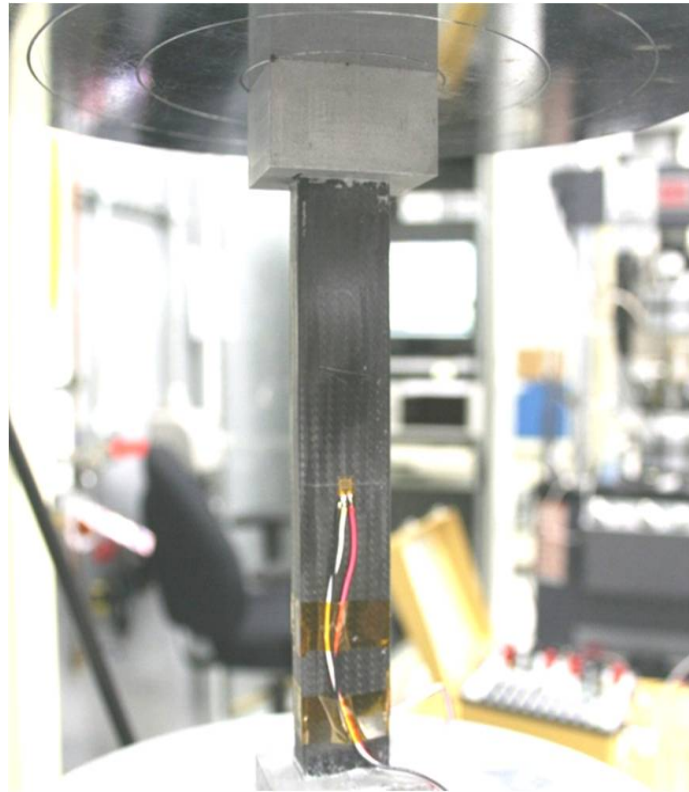


Figure 83 Plain Waveguide in Compression Fixture Showing Wall Buckling



Figure 84 Plain Waveguide Close Up Showing Out of Plane Displacement of Broad Wall

The slotted waveguides also showed buckling and showed mixed results. Some tended toward the Riks analysis where the three slots had the broad side of the slot displace inward and the two slots on the opposite side of the centerline had their broad sides displace out, others had the inverse. Figure 85 shows a slotted waveguide with the outermost slots bulging out. Figure 86 shows the same behavior in a close up of the two slots and Figure 87 shows the top most slot with a strain gage buckling inward.

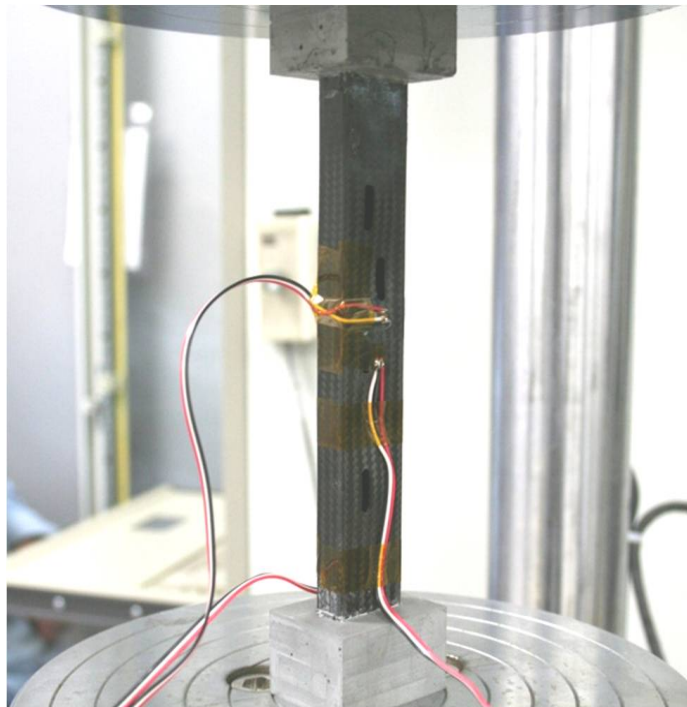


Figure 85 Slotted Waveguide in Compression Fixture with Slot Wall Buckling

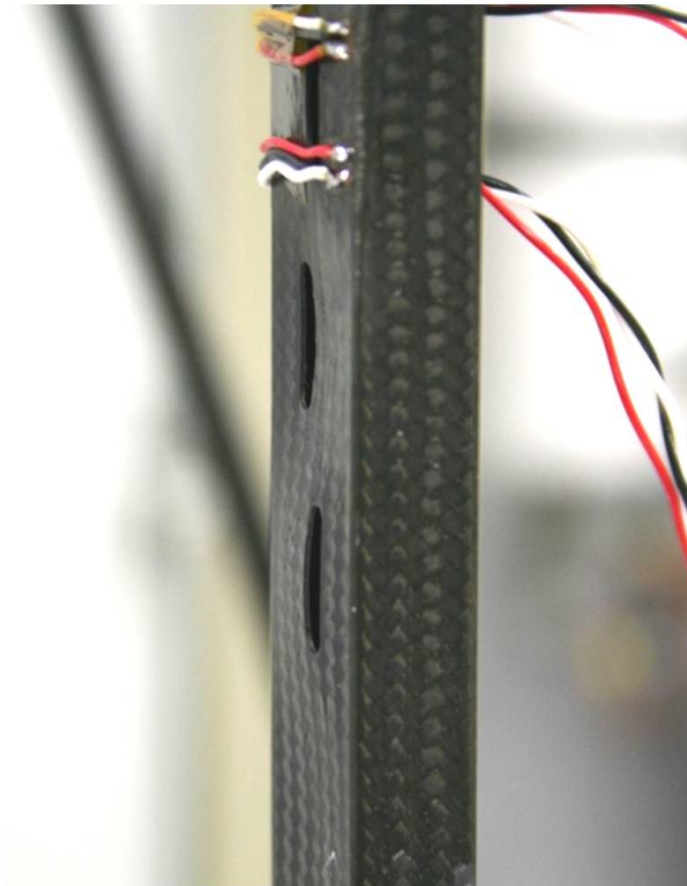


Figure 86 Two Slot Close Up Showing Alternating Concavity of Buckling

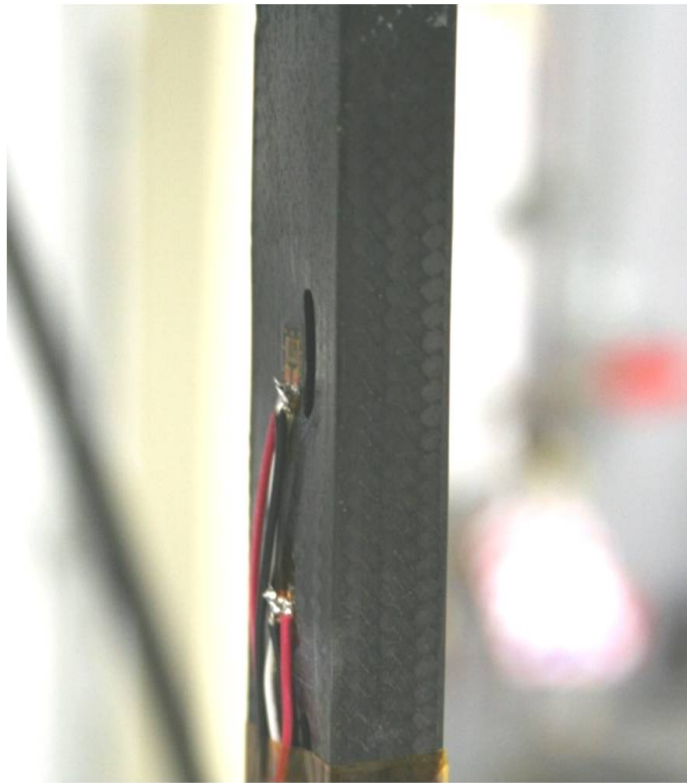


Figure 87 Close Up of Single Gaged Slot with Concave Buckling

As shown earlier in Figure 58, each lab specimen was gaged almost independently so different results can be seen for each waveguide (Figure 58 shows the gage locations for each specimen). The raw strain data is given in Appendix D. Specimen seven is an interesting specimen to analyze. Figure 88 shows the strain gage data from the three gages of specimen seven. Gages one and two are at similar locations near the two slots that are on the opposite side of the centerline of the other three slots. Gage three is near the slot closest to the top of the waveguide on the opposite side of the centerline as one and two. Figure 87 actually shows gage three from specimen seven. The interesting features are that all of the gages follow an identical path for a period of time while the axial compression of the waveguide is occurring and then the first two gages snap to a tensile strain due to the outward displacement of the slot walls and gage three carries greater strain for the same amount of loading indicating compressive strain again from the out of plane local wall bending. This strain gage data shows the same trends as in the Riks stress displacement plots and confirms the compressive nature of the slot wall as seen in Figure 87.

Specimen three is another specimen that shows expected results. The four gages for specimen three were mounted after the first batch of tests. When the sinusoidal waves were observed in the first batch of tests, the strongest displacements were near the ends of the waveguide in the broad walls. For this reason, the strain gages for specimen three were mounted at these locations to try and best capture the bending scenario at hand. Figure 89 shows the strain gage data for the four gages of specimen three. All four gages are in agreement and show instability within a good range. Initially all four gages are in compression according to the general compression of the waveguide. When instability occurs and the walls begin to displace out of plane, the slope of the curves quickly switch directions

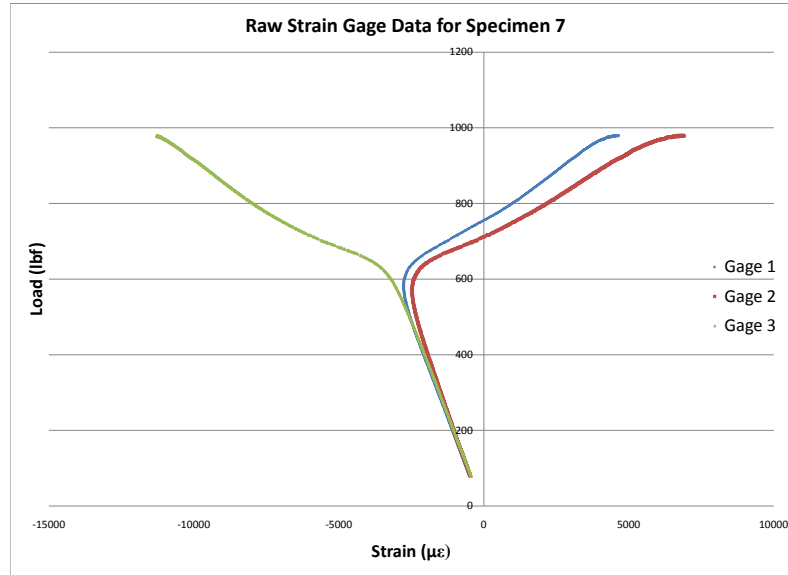


Figure 88 Strain and Load Data from Specimen Seven

and tension begins to overwhelm the strain characteristics seen by the gage. Gages one and three are close to each other and the same trend is seen with gages two and four. These two sets were adjacent to each other, one and three being mounted on the top of the waveguide and two and four being on opposite walls on the bottom. This shows that although the top and bottom out of plane displacements are not perfectly symmetric, they are very symmetric across the front and back walls as seen in the FE results.

Specimen five shows meaningful data from the strain trends as well. Three gages were attached to specimen five. Figure 90 shows the load strain curves. The behavior of gages one and three is similar as expected due to their location. One should note that gage one shows instability at an earlier point than gage three. Gage one is mounted adjacent to the slot and gage three is on the non-slotted back wall. The slot again causes earlier instability

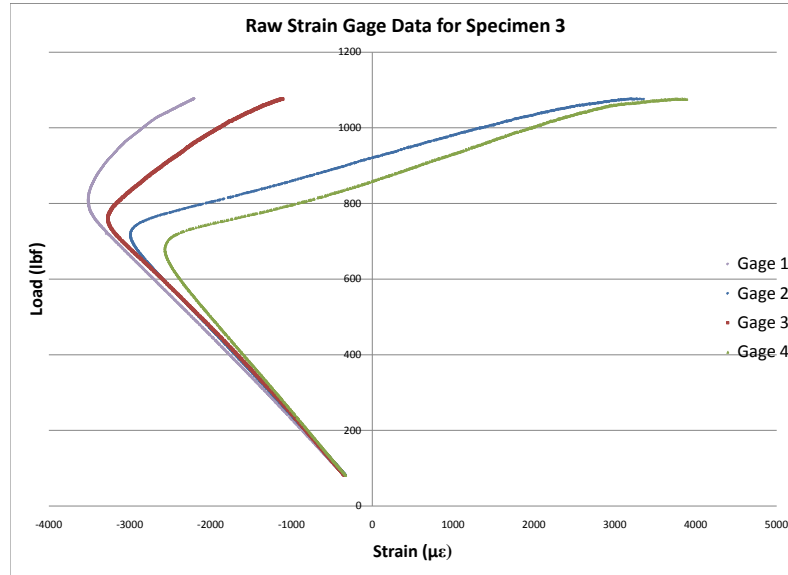


Figure 89 Strain and Load Data from Specimen Three

and starts out of plane displacement causing tensile strains earlier than the plain wall does, even though the two gages are mounted in the same location on opposite walls. Gage two shows the transfer of the stresses from one slot to the next. It is in tension from the start because it is transverse to the load and experiences some Poisson effects as well as transfer stresses as the stress flows from one slot to the next. The region in between the slots under gage two also experiences instability, but at a higher load than the wall adjacent to the slot. This shows that the slot wall out of plane displacement is the first unstable event to be seen and this corresponds well with the data from Figure 80 at the beginning of instability on the slotted FE model.

Other data was collected and can be compared. Most notably, specimen six seems to not have an instability load as shown in Figure 91 shows the data. Even though the curves

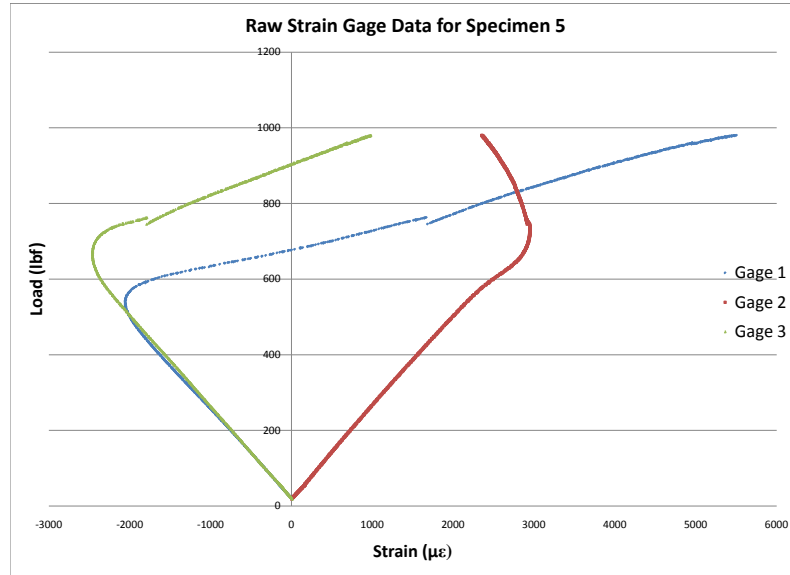


Figure 90 Strain and Load Data from Specimen Five

seem rather linear through the entire test, this is only a coincidence of the gage location. The out of plane displacements for this waveguide did not occur directly underneath the gages, but the gages were placed over transition regions from a concave to a convex displacement so no significant bending strains were noted. This is verified visually through Figure 92, which clearly shows buckling shapes in specimen six, but the gages are not on top of the sinusoidal lobes.

The ultimate failure of all waveguides was due to fiber fracture. Although instability was seen at around the 700 pound (3100 N) point in the tests, the material did not have any macroscopic failures at that point. The test continued through the loading until the material reached a stress limit and failed. The failure paths of all of the cracks in the waveguides was similar, whether slotted or not. The cracks would run perpendicular across the front and

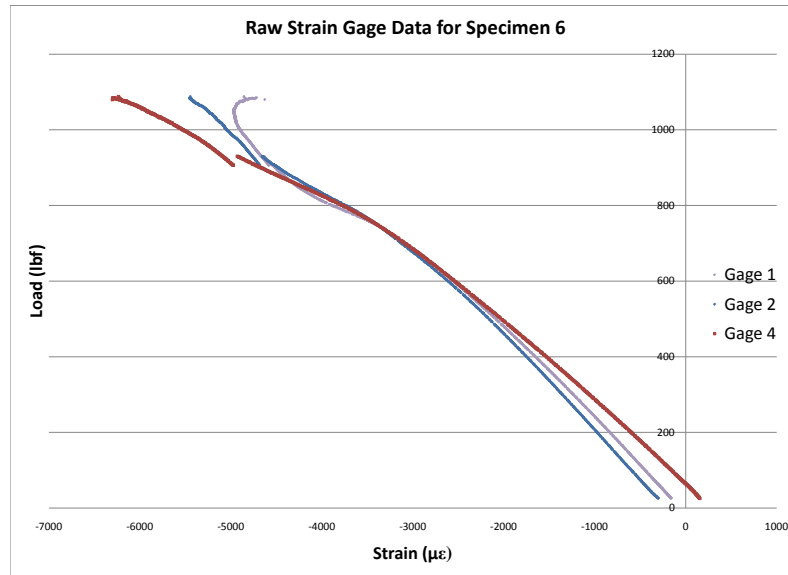


Figure 91 Strain and Load Data from Specimen Six

back broad walls but would be offset by some axial distance. The crack transition from one side to the other on the side walls was along a shear plane at about 45° to the axial direction. Figure 93 shows this crack as well as the perpendicular broad wall crack on specimen three. The material failed all at once as well since all failures were characterized by a single loud snapping sound as opposed to a progressive crackle sound for a slow moving crack. When slots were present in the broad wall, the cracks started somewhere along the straight edge of the crack and moved towards the closest side wall. The same shear plane failures were present on the side walls. Appendix E shows failure images for all seven specimens.

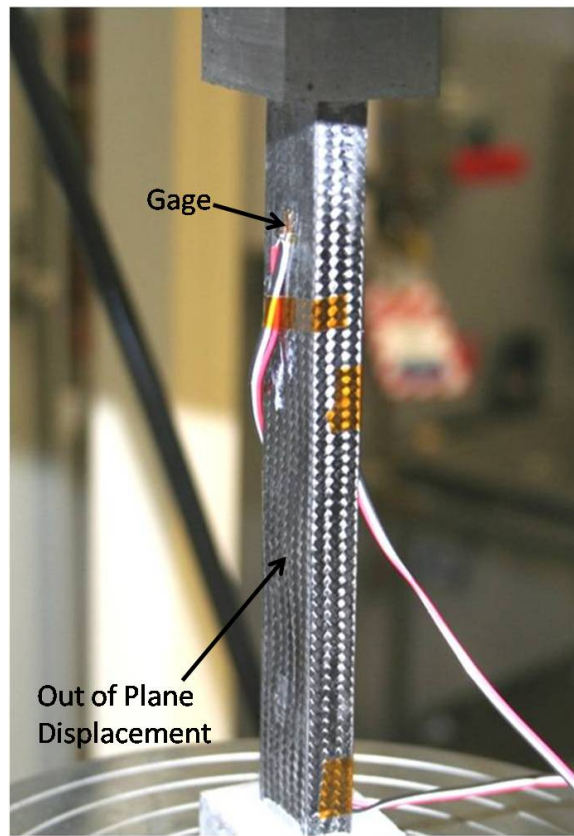


Figure 92 Lab Photo of Specimen Six Showing Out of Plane Wall Displacement

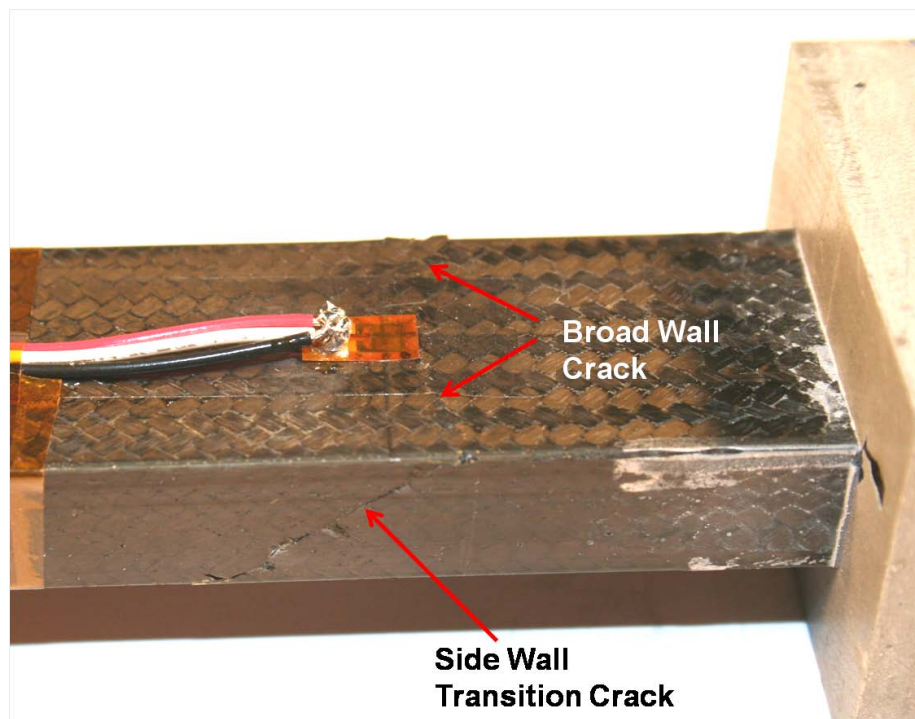


Figure 93 Shear Plane Side Wall Failure and Transverse Broad Wall Failure Cracks on Specimen Three

4.5 *Summary of Results*

Overall, all results from all tests proved meaningful and agreed well. The experimental tests had one faulty test with specimen nine, and many hours were spent configuring the FE models for correct outputs, but an incredible amount of good data was produced. It was shown that the longitudinal slot was by far the best single slot in terms of stress and strain in a representative waveguide. In terms of the maximum von Mises stress at the slot tip, it outperformed every other slot by at least 28% and was only 62% higher than a waveguide with no slots. Through the linear bifurcation analyses of the plain and slotted waveguides, it was shown that the first five buckling loads were within a tight range and so buckling loads should be avoided. Only local wall buckling was observed which was influenced by the slots when present. In terms of linear bifurcation, the slot array produced an 8.7% decrease in the critical load. The nonlinear analyses also showed that instability would be an issue in the waveguides and would occur before material failure. In terms of a limit load from the Riks analyses, the slot array produced a downgrade of only about 7%. The material failure stresses around the slots were more pronounced and would decrease the allowable load of the waveguide by about 15% depending on which failure criteria is used. Experimental results agreed very well with the numerical simulations. The experiments predicted a drop in instability limit load performance of 14% which is a very close result to the analytical considering the possible imperfections and errors in experimental work. All experimental tests showed similar wall instability characteristics to the numerical simulations. Again, on a whole all results compared very well and showed promising structural performance of the slot array.

V. Conclusions

The final results were presented after a multitude of preparation tests and studies were completed. The whole of the material characterization and finite element simulations were prepared to compare to the results of the eight experimental tests. All initial testing goals were met and all data collected appropriately. This chapter will draw overall conclusions from the data and recommend some steps for further research.

5.1 Conclusions

A great deal of testing was accomplished and much can be learned from the results. Along with pieces that seemed promising and should be further investigated comes areas that showed bad results and can be eliminated from further testing. The material properties gathered from the CFRP weave layup show interesting results. The compressive limit strength of this CFRP was found to be less than the compressive limit strength of some ductile aluminums. For example, the yield strength of 2024-T3 aluminum is around 45 ksi (310 MPa), where the compressive limit strength of this weave was found to be only about 38 ksi (262 MPa). This is not typical of all carbon fiber layups and so it is recommended that if the intent of construction is to carry maximum structural loads, a different material or better layup be devised. The choice of this woven fabric was due to ease of construction, but with high performance aircraft composites, a high performance fiber must be used regardless of construction difficulties.

The results of the slot characterization study showed the clearest results of all. For typical non-structural waveguides made from metals, the array is almost always a longitu-

dinal slot array offset from the centerline. This same longitudinal slot showed by far the best results in the stress and strain field characterization. When dealing with multi-variable optimization, it is often the case that tradeoffs need to be made in order to find a balanced solution, but in this case the best scenario for both electrical and structural purposes is the longitudinal slot. This provides a clear cut vision for the way forward and all other data can be used as proof of the performance and possible alternate configurations if other design criteria come into play that would prevent the longitudinal slot from being used. In this case, the H slot is the best option due to its small area and fairly reasonable stress and strain results.

One of the main goals of this thesis was to determine the degradation in compressive limit load performance generated by a slot array. While it may not be extended to a slot array of any number or a waveguide of any length, the five slot array showed very promising results. Structural degradation in compression when considering axial instability was on the order of 10%-15% depending on the specific type of test. This is a very low drop in performance and shows that the SWASS concept has very high potential. Since the thickness of the waveguide walls has a cubic effect on critical loads as shown in Eq (3), increasing the thickness of the slotted waveguide wall by only a small amount should easily make up for the small drop in performance caused by the slots. With enormous amounts of surface area available on the underside of the aircraft fuselage and wings, the performance of the radar system and aircraft in general could greatly increase.

Another goal of this study was to develop an accurate finite element model for the prediction of the compressive performance of the CFRP waveguide. This was successfully accomplished. Differences in the FE and experimental results were only slightly greater

than differences between the experimental specimens themselves. It is not possible to rely on the FE models solely, but as a first cut estimate and parameter analysis tool, it can save great amounts of time and funding.

Overall, a great structural base has been built to allow for further SWASS design and testing. These elemental studies should give any engineer, regardless of specific background, a useful set of data to take advantage of in structural waveguide design. The single slot behavior to the material failure characteristics to the slotted waveguide performance versus the plain waveguide are all valuable tools and can allow for a building block and a shift of the research focus to a more specific and complete SWASS system design.

5.2 Recommendations and Suggestions for Future Research

Although most of the critical data was analyzed, there were massive amounts of data produced and it is probable that much more could be learned from the current data even with no further testing. There is also much more testing that could be accomplished.

The next step in testing would be to integrate the waveguides into a CFRP panel that can demonstrate the two dimensional slot array of the SWASS concept. The boundary conditions of each waveguide will change when integrated into a panel with each other and so the study can make use of this elemental data and compare it with the data attained from a panel study. When panel data has been collected, then integration into an airframe for an initial prototype test would be valuable to catch any issues that may have been overseen in the lower level testing. This process can be continued until a full performing system is designed.

As technology advances in material design, composite materials are increasingly at the forefront of development. With a sight of implementing this panel in a future aeronautical system, the design of an appropriate material is also important. One of the great benefits of composite materials is the tailorability of the properties. With the knowledge of failure mechanisms of the current material and configuration, a specific material or material orientation to counter these effects would be of most value. Technologies in braiding and weaving are ever advancing and the ability to use these latest methods for a SWASS concept would be of great value.

It goes without saying that this is only a structural characterization of the waveguide properties. Much research can happen in parallel with electrical performance studies. When the electrical and structural data has all been collected, a systems approach can be taken to optimize the performance for both functions. There are also many other structural loading situations to consider to include tension and bending performance, fatigue, vibrations, damage tolerance and environmental concerns such as corrosion and many more.

There are many different paths that can be taken from here to demonstrate the value of the SWASS concept, and this study has provided only the first step in the process. The first step is promising and the data shows that the slots would have acceptable performance effects on the structure and continued research, in whatever form, is recommended.

Appendices

Appendix A. Finite Element Model Creation and Analysis

This appendix will lead the reader through a step by step process to create and analyze the waveguide part as completed in Abaqus.

1. Part Module

- (a) The first step will be to create a 3D, deformable, solid extrusion of approximate size 50 for the waveguide part.
 - i. When the sketch opens, sketch the outer dimensions of the waveguide (1in x 0.5in). The sketch should have square corners at this point and the fillet will be applied later.
 - ii. Select done to exit the sketch and create a depth of 6 inches.
- (b) Next cut the center out of the extrusion to create a thin walled tube.
 - i. Create a cut on one of the end faces of the waveguide.
 - ii. Draw the inner dimensions with square corners into the waveguide. Nominally, all walls have a thickness of 0.022 in. It is easiest to create an arbitrary rectangle inside the section then use the dimension tool to apply the proper thicknesses on all four edges.
- (c) Create slots if necessary by an extruded cut on one of the faces as well. Once inside the sketch and one slot has been drawn, it may be beneficial to use the linear pattern tool to create a pattern of the slots.
- (d) In order to allow for smooth transitions in the mesh stacking direction, we need to create round fillets on the inside and outside corners.

- i. Select all the edges that need to be rounded. Figure 94 has these edges highlighted.

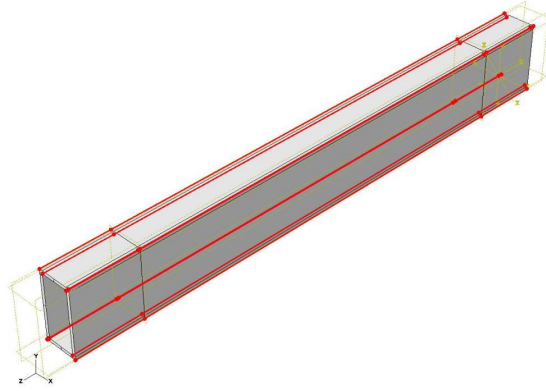


Figure 94 Waveguide Model with Rounded Edges Highlighted

- ii. Create a radius of 0.005 in for all of the edges. This small radius keeps the model as close to reality as possible.
- (e) Create datum planes and partition for later use in meshing.
- i. The first four datum planes will section off the areas where the sweep direction will be straight towards the square sides or at a diagonal on the corners of the waveguide. Figure 95 shows a closeup of the positioning of each plane.
 - ii. Partition the waveguide 4 times by using “Partition Cell: Use Datum Plane” and use the 4 planes created above. When done there should be four cubic side shapes and four 3D curved shapes for each corner.
 - iii. The next step is to create a line to define the sweep path used during meshing. Do this by creating a partition on each of the end faces. The line will be at a 45 degree angle from the center of the inside fillet to the center of the outside fillet. Figure 96 shows this line on one corner.

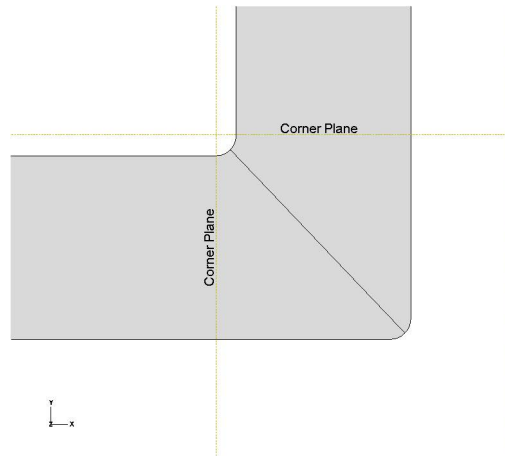


Figure 95 Close Up of Datum Plane Positioning

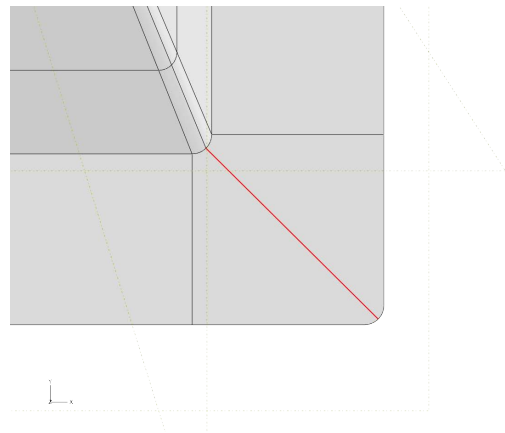


Figure 96 Close Up of Face Partition for Sweep Path

- iv. In order to allow for a better mesh, partition the corner *cells* in half by extruding the diagonal line that was just created along the length of the waveguide. The option for this type of partition is “Partition Cell: Extrude/Sweep Edges”. There should now be a total of 12 cells in the model: 2 halves at each corner and the four rectangular sides.
- v. For easier layup creation, create 8 datum coordinate systems (CSYS).
 - A. Each coordinate system will have its x-y plane in the plane of the waveguide and will have an outward pointing z direction. This will allow for

simple and quick layup orientation definitions in the composite layup editor. Figure 97 shows the CSYS for two sections.

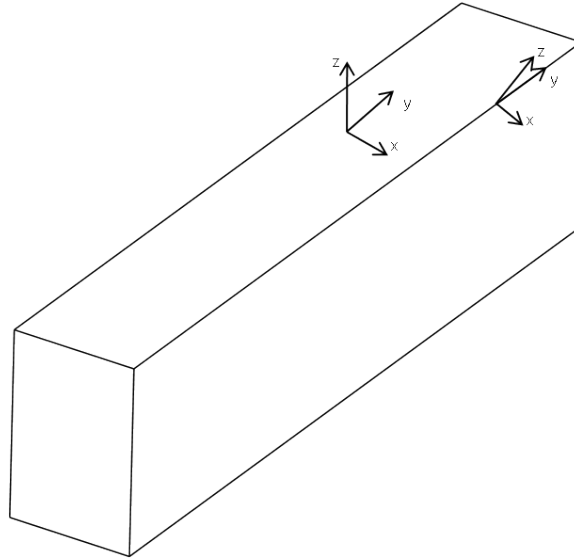


Figure 97 Datum Coordinate Systems for Layup Sections

2. Property Module

- (a) Create the material properties for the carbon fiber in the property module.
 - i. Create a carbon fiber material by selecting lamina as the type and inputting the appropriate properties.
 - ii. Open the composite layup editor to create a composite layup for the waveguide. Start with an initial ply count of 2 and use continuum shell elements.
 - A. In the layup orientation section, choose definition to be coordinate system. Click select and choose appropriate CSYS created before. Ensure that the normal direction is selected as axis 3.
 - B. In the stacking direction box, make sure element direction 3 is chosen.

- C. For section integration, choose during analysis to allow for non-linear effects to take place during deformation and use Simpson as the thickness integration rule.
- D. In the box at the bottom where the properties of the layup are input, double click region and select the region of the waveguide that corresponds to the selected CSYS.
- E. Double click material and select the carbon fiber material that was created in step 2(a)i.
- F. Double click element relative thickness and type in 0.5. This means that each layer will be equal to half of the total element thickness, which is correct with only two layers of carbon fiber.
- G. Double click rotation angle and select appropriate angle. For this case the rotation angle will be set to zero since all material property testing was done with the proper fiber orientation.
- H. Leave the CSYS tab alone.
- I. Double click integration points and select 5 for better accuracy or higher if desired.

iii. Create all 7 other layup sections similarly. When finished, all sections of all parts should be green in color in the property module indicating they have been assigned appropriate properties.

3. Assembly Module

- (a) Create 1 dependent instance of the waveguide.

4. Step Module

- (a) Create the appropriate step for analysis. In this thesis, general static, general riks, and linear perturbation buckle were all used at some point. To change the step go to the step manager and select replace on the appropriate step.
 - i. For the general static step, accept all defaults and turn on nonlinear geometry.
 - ii. For the static riks step, first ensure that nonlinear geometry is on so that the nonlinear effects of the slots or buckling modes can be captured. Click on the incrementation tab and adjust the maximum arc length increment to 100 and adjust the maximum number of increments to 200. This should ensure capture of the limit load region, but the increment size can be increased at first to determine an approximate arc length of interest and then reduced to the 100 value. This value has proven to provide sufficient detail and smoothness in the data.
 - iii. For the buckling analysis, select the Lanczos solver and input a number of eigenvalues requested. Keep in mind that the Lanczos solver becomes less accurate with increased number of eigenvalues and may slow down the analysis greatly.
- (b) Edit the field and history output requests to make sure appropriate data is being recorded. The stress, displacement, strain, and nodal forces are all relevant to these analyses.

5. Load Module

- (a) Create the load on the top surface of the waveguide.
 - i. In order to allow for 1 pound of load, which makes eigenvectors equal to the buckling loads and an LPF equal to the load in the Riks analysis, create a pressure force of 15.6094 psi on the waveguide end face.
- (b) Create the appropriate boundary conditions.
 - i. Create a displacement/rotation boundary condition and apply it to one of the waveguide end surfaces. For the bottom, create no displacement in the 1,2, and 3 directions. This will effectively pin the bottom. Since continuum shell elements do not allow rotation, no rotation boundary conditions are required.
 - ii. Create another displacement/rotation condition and apply it to the top surface. For this condition, allow displacement in the longitudinal direction of the waveguide. In the case of this specific model, only the 1 and 2 displacement directions should be restricted to zero.

6. Mesh Module

- (a) Mesh the waveguide.
 - i. First seed the part with global seeds of 0.022. It is recommended that multiples of the thickness value be used for most accurate representation.
 - ii. For increased detail and accuracy, seed the edges of the slots or create partitions around the edges of the slots or areas of interest and seed the edges to get the desired seed density.

- iii. Assign mesh controls to all regions. The elements should be continuum shell hex elements with a sweep mesh buildup. Click redefine sweep path and select all regions. Make sure the sweep path goes from the inside out for all sections. Each corner region should use the diagonal line created earlier as the sweep path (see Figure 98).

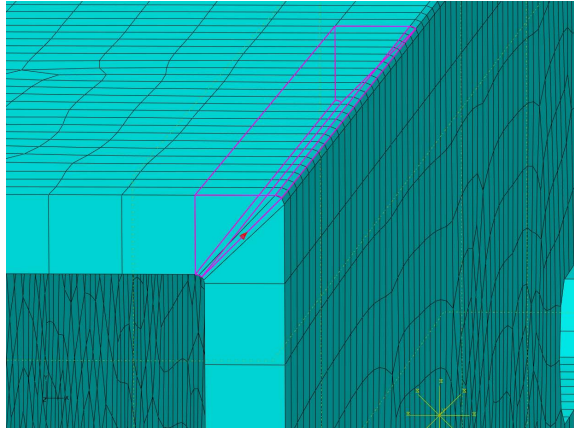


Figure 98 Detail Showing Sweep Path of Corner Cells

- iv. Assign standard, linear continuum shell elements as the element type. This should be the only one available in the hex configuration; an 8 noded element.
 - v. Mesh the part.
- (b) Make sure all the meshing was successfully completed or go back and adjust what needs to be adjusted.

7. Job Module

- (a) Create a job and give it a distinctive name such as “slotted_buckle” or “riks_noslots_1%imperfection”.

- (b) Select the parallelization tab and use as many processors as are available (Only one processor may be used for buckling analyses). Make sure the domain is equal to the number of processors being used.
- (c) Select the precision tab and select double and full.
- (d) For a converged riks solution, it is necessary to add an imperfection to a model without slots to introduce a bending moment at the initial loading point.
 - i. Adding an imperfection is a two step process. The first step is done during the buckling analysis. Abaqus cae does not support the addition of an imperfection, so the keywords will have to be edited manually.
 - ii. Right click on the model in the model tree on the left side of the screen and select edit keywords.
 - iii. Scroll to the bottom and select the “*Restart” entry, select add after and type the following:


```
*Node File, Global=Yes
```



```
U,
```
 - iv. Run the buckling analysis and now there is a file that stores the buckling mode data. It is named after the job that was run, for example “buckle_job.fil”.
 - v. Once the step is changed to a riks analysis, right click on the model again and select edit keywords.

- vi. Remove the node file entry from before. Add an entry just before the “*Step: Step-1” box and type the following:

```
*Imperfection, File=name of buckling file, Step=1  
  
1, 0.01  
  
2, 0.01
```

- vii. The first and second entries with a value of 0.01 mean that 1% of the first and second eigenvectors will be applied as an imperfection to the model before analysis. This number will affect the limit load so a study should be accomplished to minimize the effect.

- viii. The riks analysis is now ready to run as normal.

- (e) Submit the job from the job manager.

8. Visualization Module

- (a) With either the buckling or the static general analysis, the visualization of the results is fairly straight forward. The static riks analysis will require some extra time and effort to collect meaningful data.

- (b) Buckling and general static results.

- i. Right click on the job that was run and choose results to display the results in the visualization module. Click on the contour button to display contours of the field of interest. Usually the default is the von Mises stress. To change this field, click on results, field output and select the appropriate value.

ii. For the buckling results, the eigenvalue displayed at the bottom will be the buckling load associated with that buckling shape if the correct pressure was applied as described in 5(a)i. To cycle eigenvalues and eigenvectors, use the arrows in the top right part of the window.

iii. To save any picture from the screen, use the print option and print to a file. The easiest file to save is a *.png* file, but the resolution is poor. Save a file as *.eps* to have better resolution then convert the file using an appropriate program to a better format.

(c) Static riks results.

i. The static riks results can be opened in the same method. To be able to save plots to the results file, open it using File, Open and make sure the read only check box is off.

ii. To get an overall feel for the behavior under loading, select the “Animate: Time History” option and it will cycle through all the frames.

iii. If the deformation of the model is too large or not noticeable, it may be beneficial to change the deformation scale factor by selecting Options, Common, and specifying the scale factor by clicking the uniform button.

iv. There is a multi step process to create a plot of the stress vs. displacement.

A. Select create XY data and choose “ODB field output”.

B. For position, select unique nodal and then check a stress value and a displacement value. Typical selections for this model would be the mises stress and the displacement in the 3 direction.

- C. Click the Elements/Nodes tab and click edit selection to select the node from the viewport. The node selected must be outside of the boundary conditions to get accurate data. Figure 99 shows the node selected just to the right of the boundary condition end.

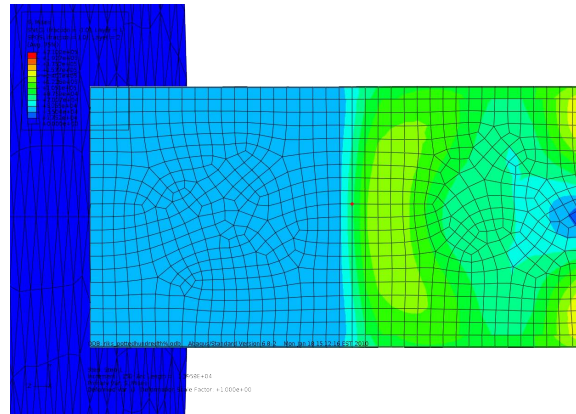
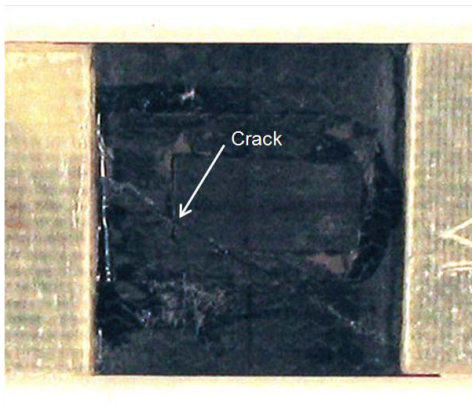


Figure 99 Node Selection for XY Data

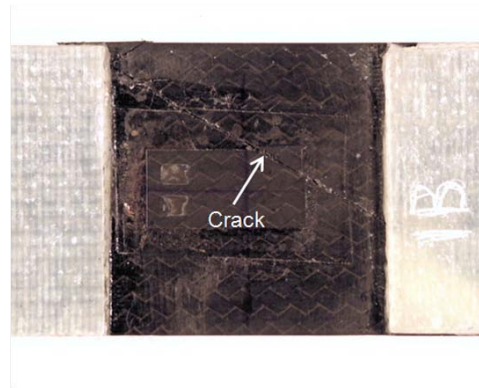
- D. Click save and accept the default values.
- E. Again click create XY data and this time select “Operate on XY data”.
- F. In the right hand box, click once on the “combine(X,X)” option.
- G. Since the displacement is negative in compression, type a minus sign before the first comma and double click the “U3” data to place it as the x-axis.
- H. Move the cursor to the right side of the comma and double click the appropriate stress data. Usually it is section point one mises stress. The final expression should look similar to “combine(–“U:U3 Pl:PART-1-1 N:1481”, ”S:Mises(Avg: 75%) SP:1 Pl:PART-1-1 N:1481”)”.
- I. Click plot and “save as” to plot and save the data.

- v. The next step is to find the load at a step of interest. Most of the time the step of interest will be where a principal stress exceeds the material limits or where the limit load of the buckling analysis occurs.
 - A. Find the step of interest by right clicking on the stress displacement data and finding the step of maximum stress. Open the job's *.sta* file and look at the LPF number at that step. This is the load on the waveguide at that step since the model had a load of one pound applied through the pressure.
- vi. The only other significant method of data capturing is creating a video file that displays the time history deformation. To do this select animate, save as and proceed with the options best suited for the display of interest.

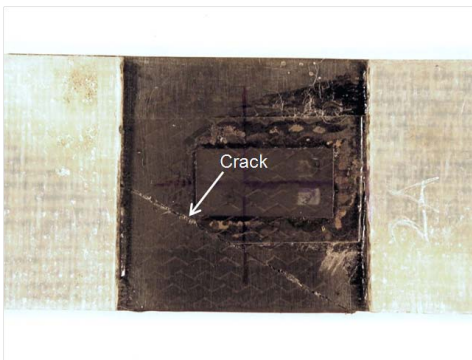
Appendix B. D3410 Compression Specimen Failure Images



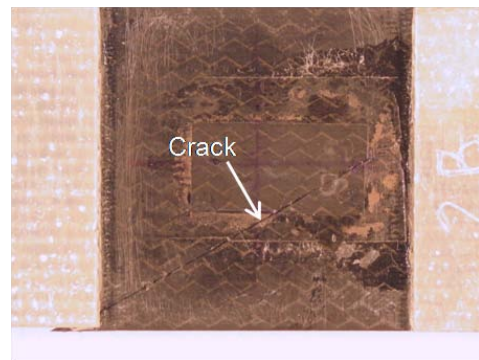
(a) Specimen 1A



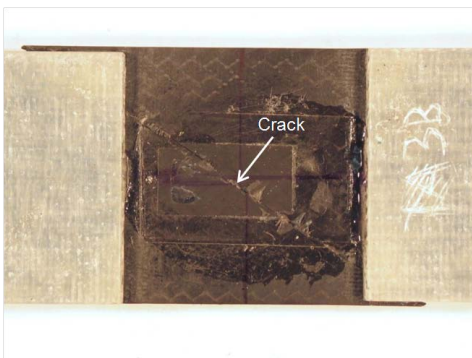
(b) Specimen 1B



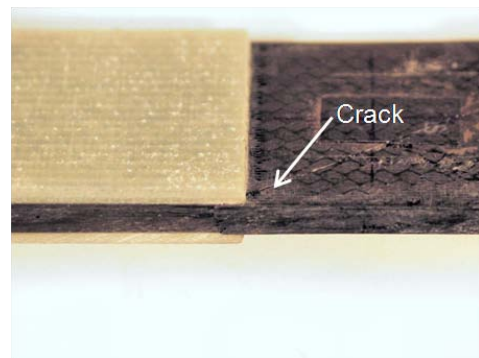
(c) Specimen 2A



(d) Specimen 2B



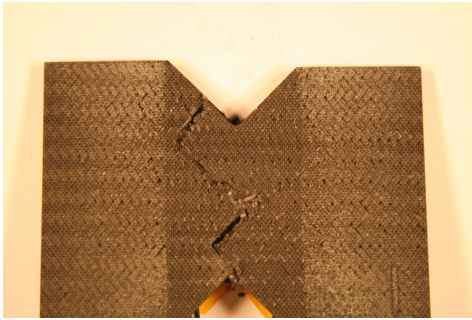
(e) Specimen 3B



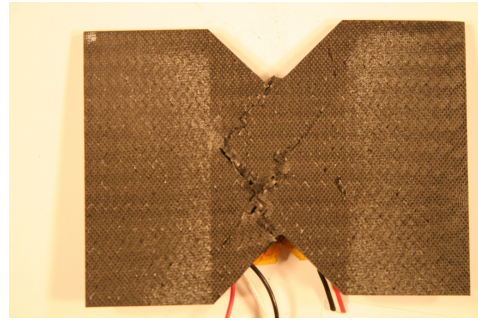
(f) Specimen 2B Detail

Figure 100 Compression Specimen Failure Images

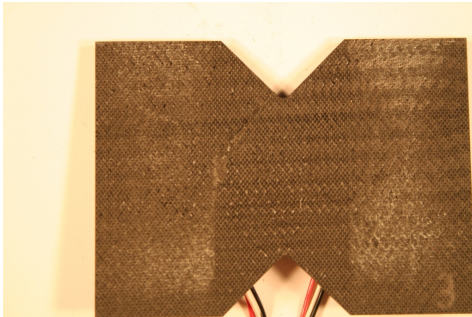
Appendix C. D7078 Shear Specimen Failure Images



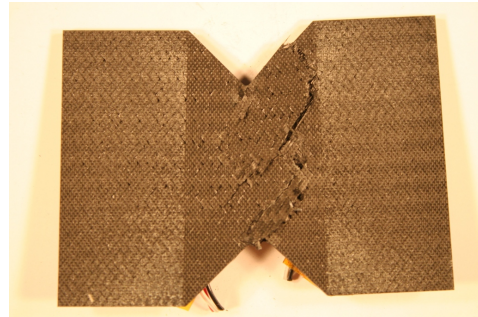
(a) Specimen 1



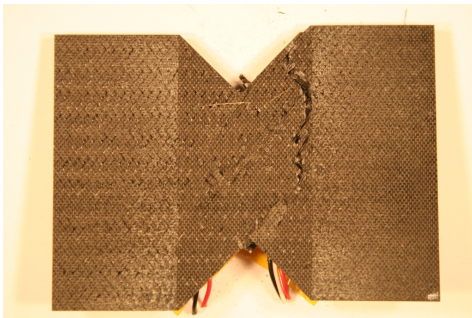
(b) Specimen 2



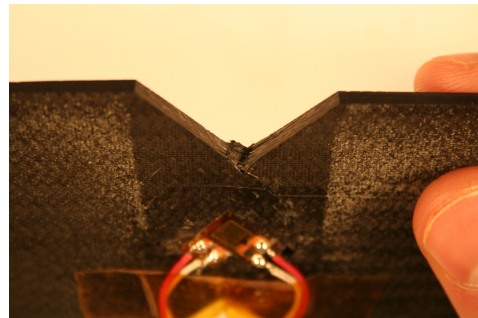
(c) Specimen 3



(d) Specimen 4



(e) Specimen 5



(f) Through Thickness Failure Detail

Figure 101 Shear Specimen Failure Images

Appendix D. Experimental Waveguide Raw Strain Gage Data

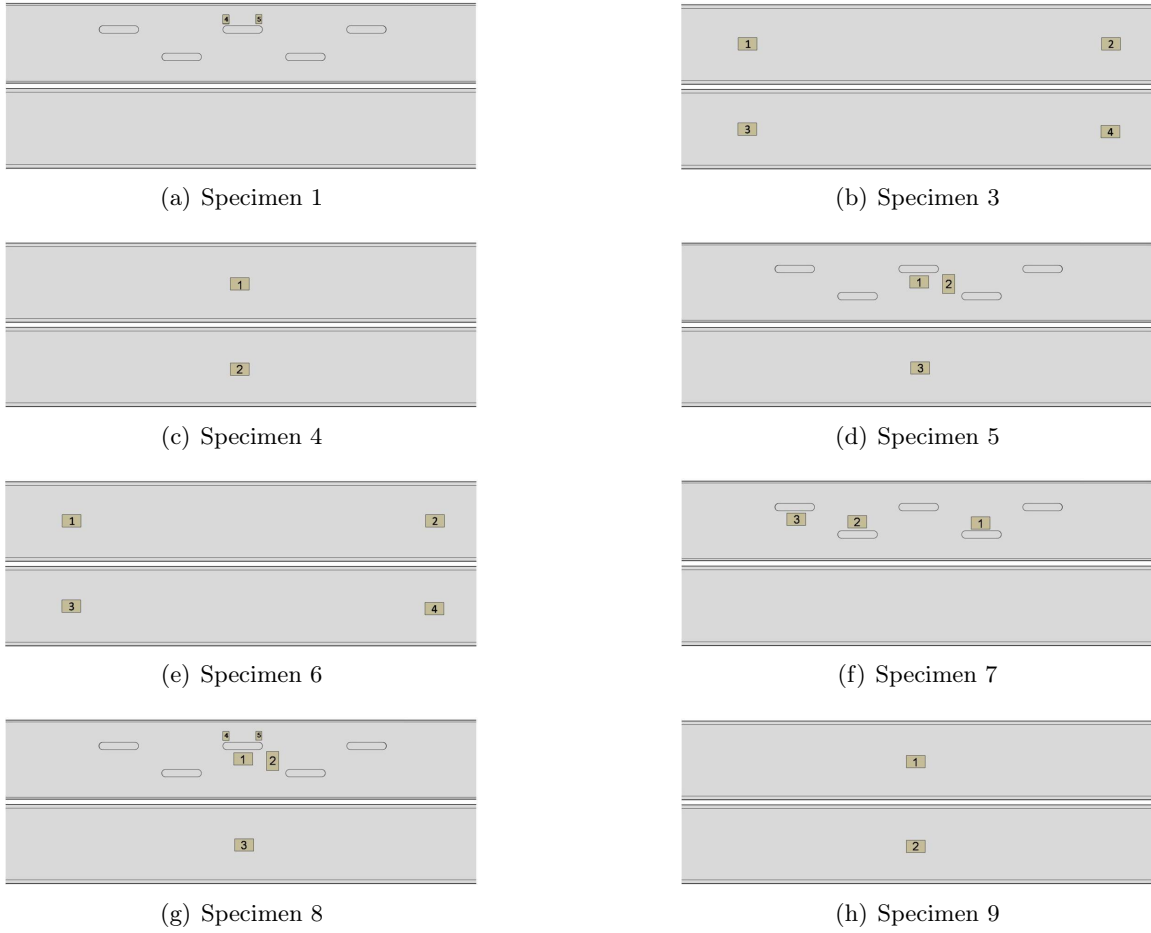


Figure 102 Strain Gage Locations for Eight Waveguide Specimens

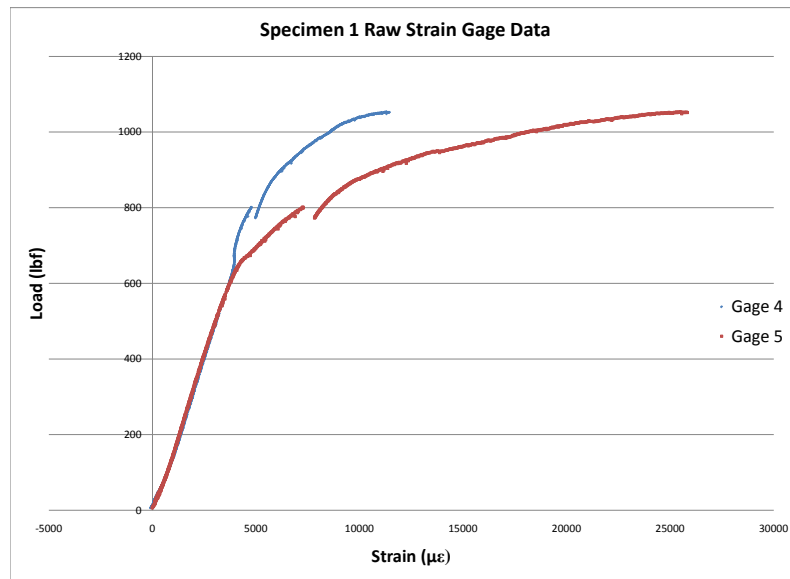


Figure 103 Raw Strain Gage Data for Specimen 1

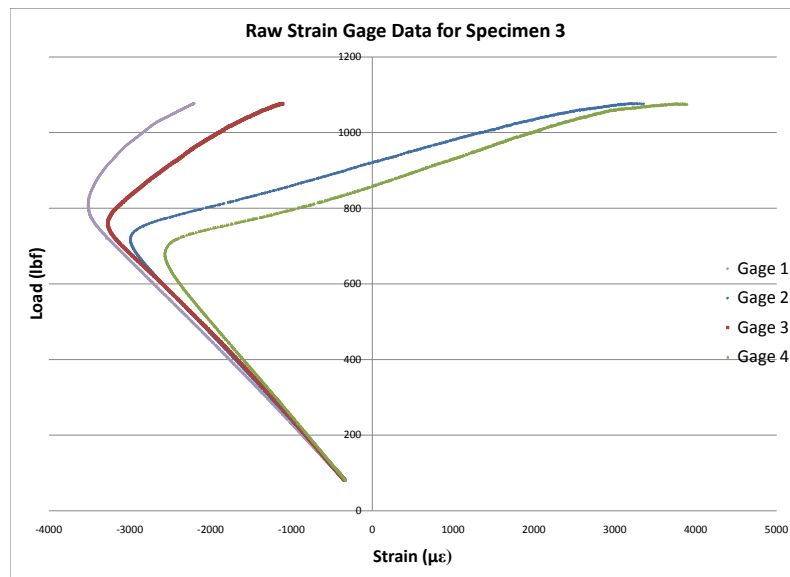


Figure 104 Raw Strain Gage Data for Specimen 3

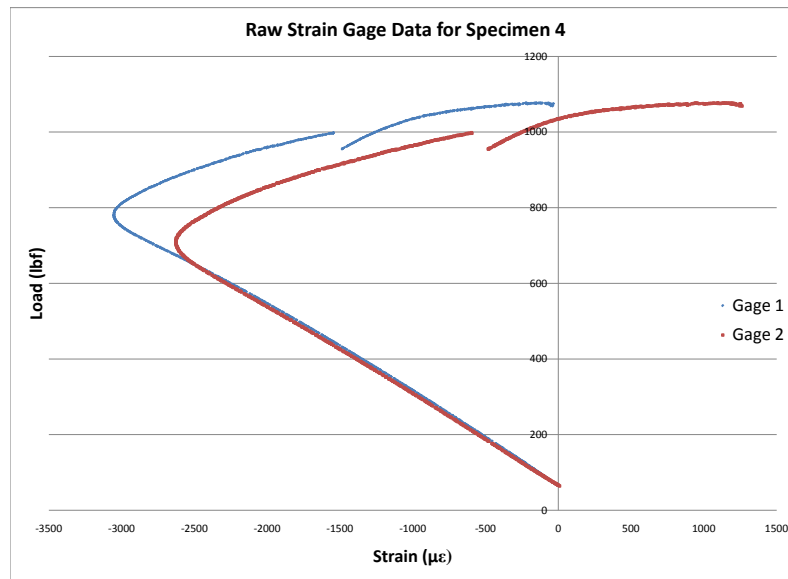


Figure 105 Raw Strain Gage Data for Specimen 4

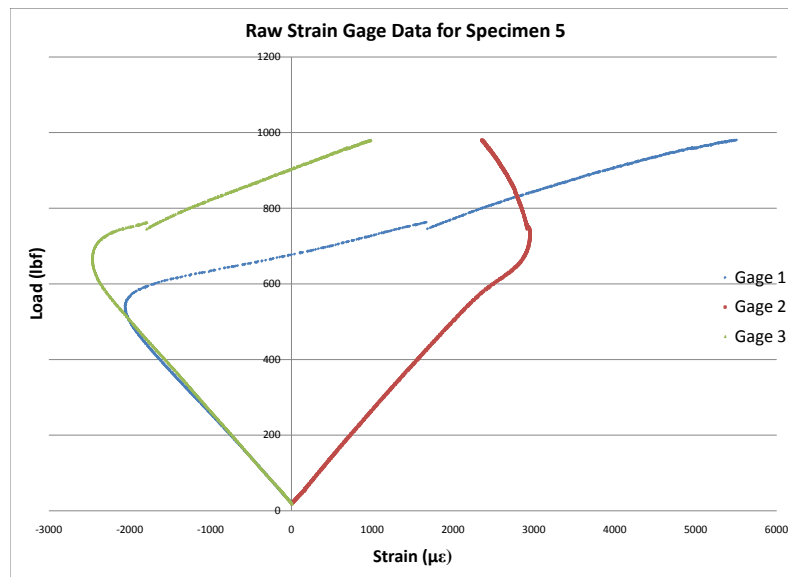


Figure 106 Raw Strain Gage Data for Specimen 5

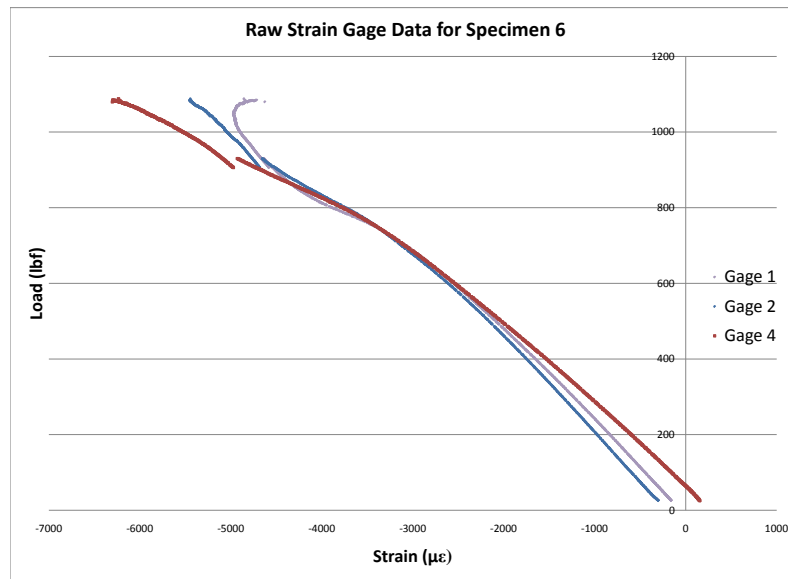


Figure 107 Raw Strain Gage Data for Specimen 6

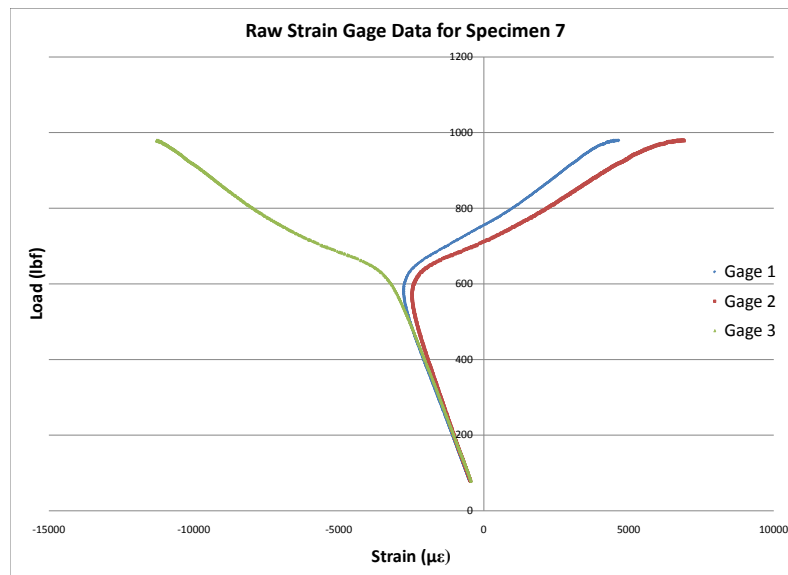


Figure 108 Raw Strain Gage Data for Specimen 7

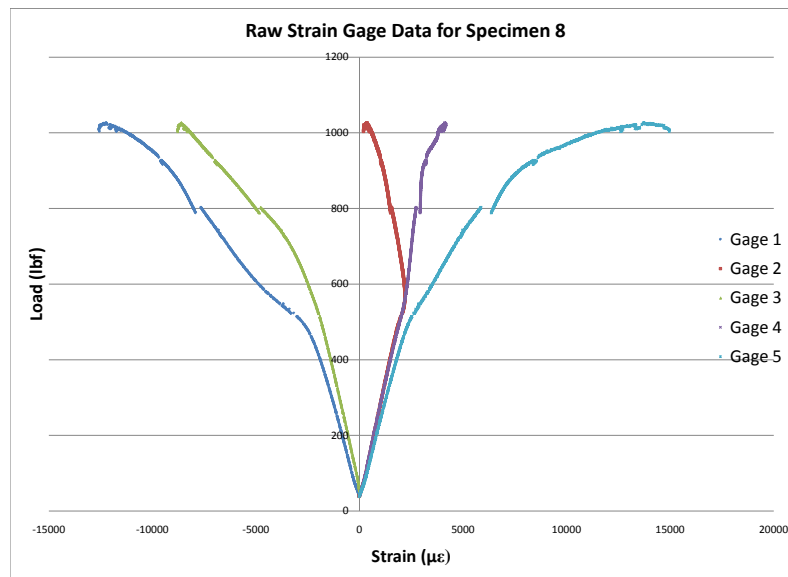


Figure 109 Raw Strain Gage Data for Specimen 8

Appendix E. Experimental Waveguide Failure Images

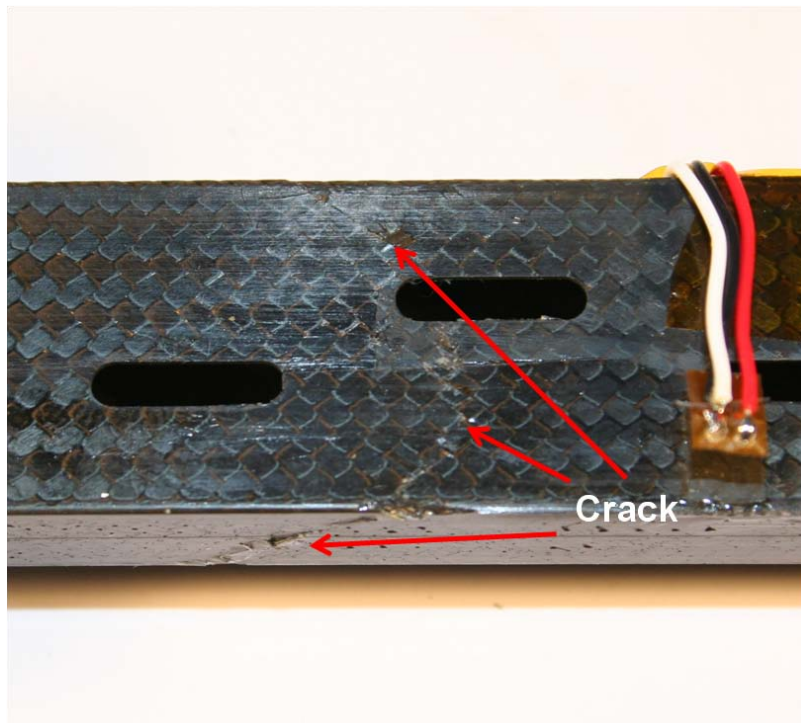


Figure 110 Specimen 1 Waveguide Failure Image

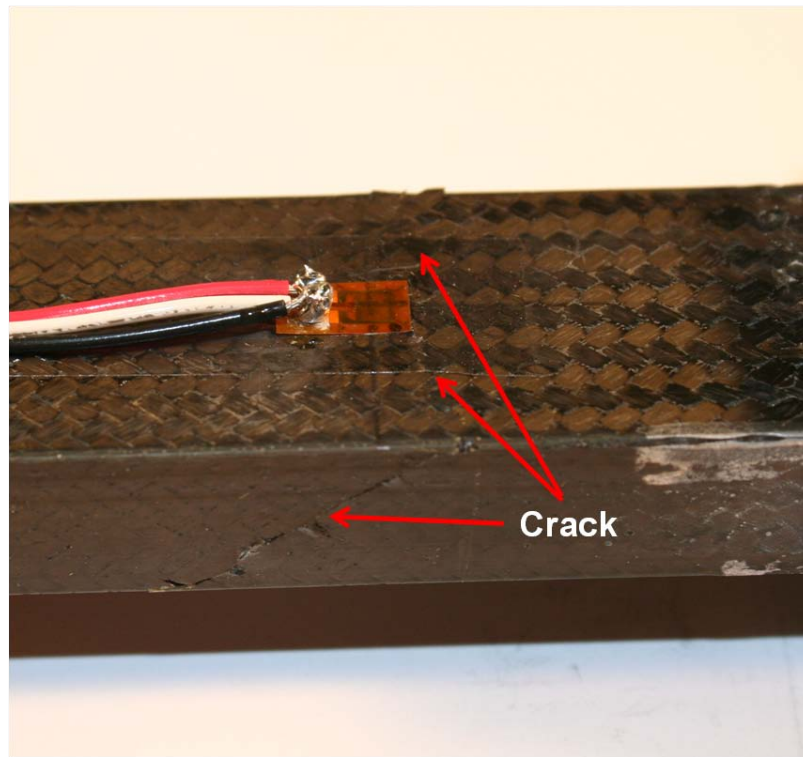


Figure 111 Specimen 3 Waveguide Failure Image

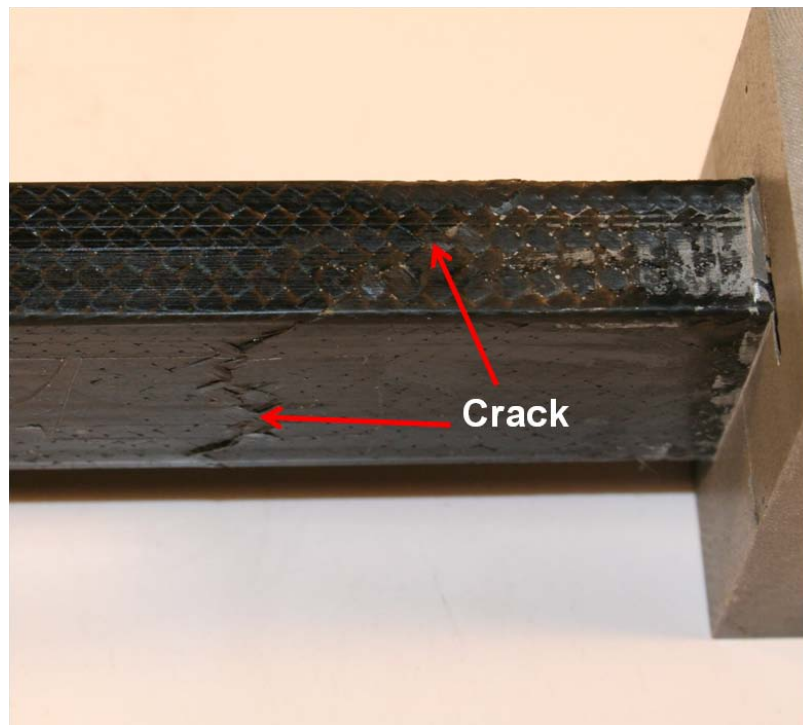


Figure 112 Specimen 4 Waveguide Failure Image

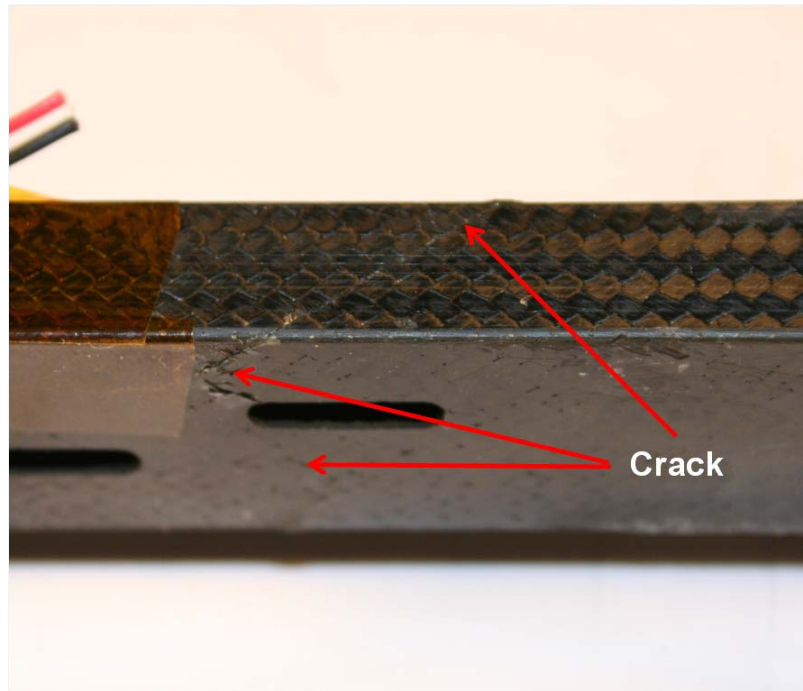


Figure 113 Specimen 5 Waveguide Failure Image

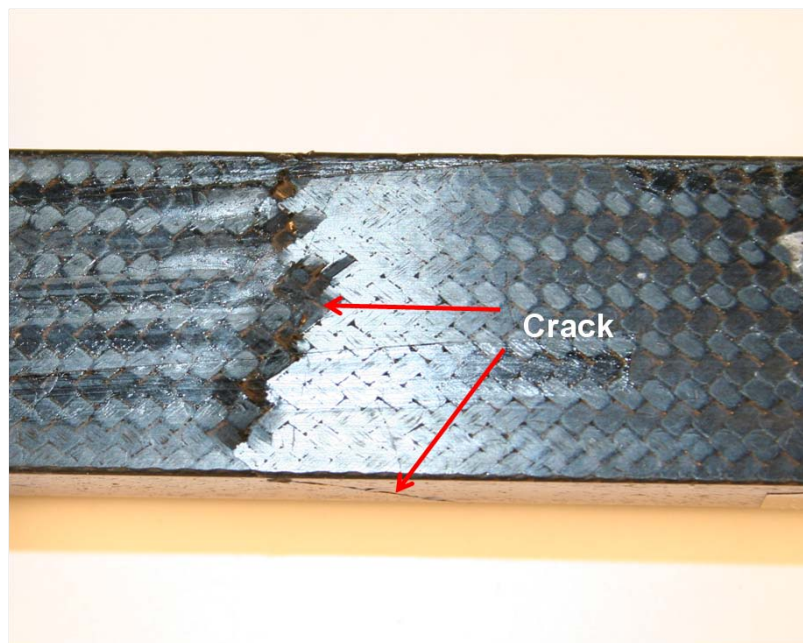


Figure 114 Specimen 6 Waveguide Failure Image

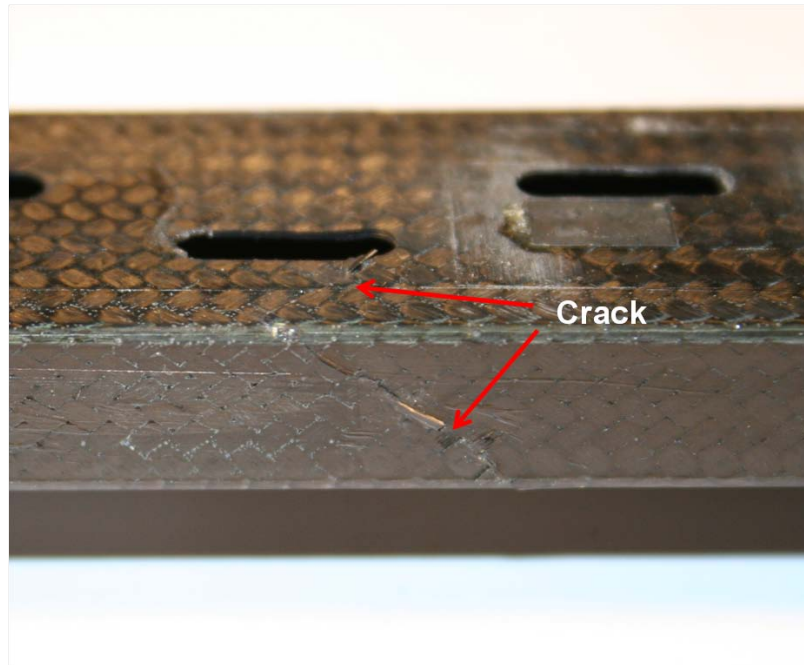


Figure 115 Specimen 7 Waveguide Failure Image

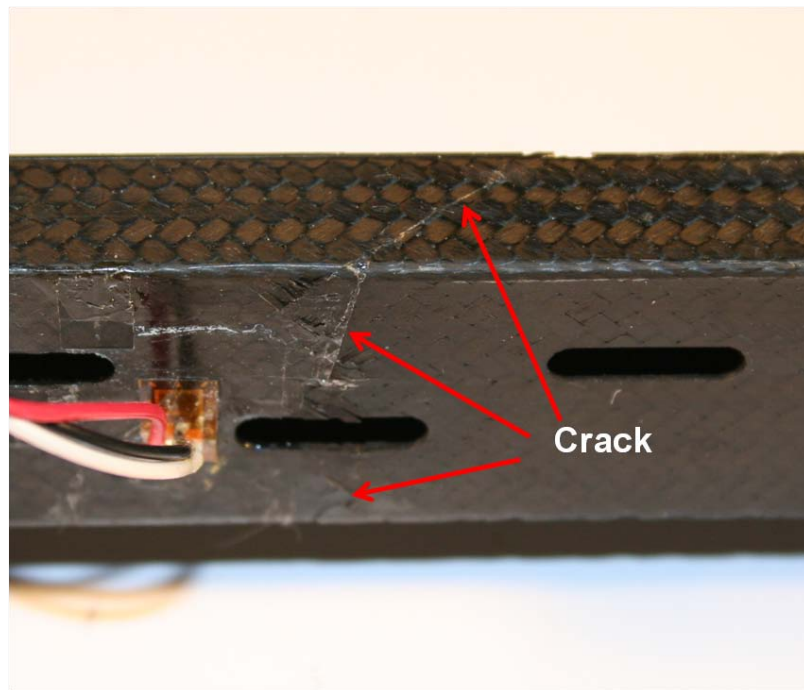


Figure 116 Specimen 8 Waveguide Failure Image

Bibliography

1. Gates, R., 2009. Defense Budget Recommendation Statement. <http://www.defense.gov/speeches/speech.aspx?speechid=1341>.
2. Wagner, R., and Ingvarson, P., 1982. "Synthetic Aperture Radar from CFRP." In Digest - International Geoscience and Remote Sensing Symposium (IGARSS), Vol. 1, Dornier Systems GmbH and Ericsson, IEEE, pp. 4.1–4.6.
3. Callus, P. J., 2007. Novel Concepts for Conformal Load-bearing Antenna Structure. Tech. rep., Air Vehicles Division, DSTO.
4. Wagner, R., and Braun, H., 1981. "A Slotted Waveguide Array Antenna from Carbon Fibre Reinforced Plastics for the European Space SAR." *Acta Astronautica*, **8**(3), pp. 273–282.
5. ERS-1 Overview. Information from http://www.esa.int/esaEO/SEMGWH2VQUD_index_0_m.html.
6. Knutsson, L., Brunzell, S., and Magnusson, H., 1985. "Mechanical Design and Evaluation of a Slotted CFRP Waveguide Antenna." In Conference Proceedings of the Fifth International Conference on Composite Materials (ICCM-V), Ericsson Radio Systems AB, The Metallurgical Society, Inc, pp. 475–481.
7. Rosker, M. Integrated Sensor Is Structure (ISIS). Information from <http://www.darpa.mil/mto/programs/isis/>.
8. Vosilla, J. A., 2004. Northrop Grumman Reaches Milestone in Development of Embedded Antennas. Information from http://www.irconnect.com/noc/press/pages/news_releases.html?d=57261.
9. Callus, P. J., 2006. Conformal Load-Bearing Antenna Structure for Australian Defence Force Aircraft. Version 0.1, Australian Defense Science and Technology Organisation, Fishermans Bend, Victoria, Australia.
10. Silhouette Antennas. Information from <http://www.ballaerospace.com/page.jsp?page=177>.
11. Yao, L., and Qiu, Y., 2009. "Design and fabrication of microstrip antennas integrated in three dimensional orthogonal woven composites." *Composites Science and Technology*, **69**(7-8), pp. 1004 – 1008.
12. Antenna and Video Technologies. Information from <http://www.ballaerospace.com/page.jsp?page=70>.
13. Hayward, G., McNab, A., Gachagan, A., Farlow, R., Hailu, B., Atkinson, D., Girma, D., Smith, D. G., and Whiteley, S., 2001. "Embedded ultrasonic sensors for monitoring structural integrity." In REVIEW OF PROGRESS IN QUANTITATIVE NONDESTRUCTIVE EVALUATION: Volume 20, D. O. Thompson, D. E. Chimenti, and L. Poore, eds., Vol. 557, AIP, pp. 1771–1778.

14. Shaikh, N., 1992. Smart Structural Composites with Piezoelectric Micro-Constituents. Tech. rep., U.S. Army Research Office.
15. Thomas, J., Qidwai, M., Baucom, J., and Pogue, W., 2006. Multifunctional Structure-Power for Electric Unmanned Systems. Tech. rep., U.S. Naval Research Laboratory, Multifunctional Materials Branch.
16. Uozumi, T., and Kito, A., 2007. "Carbon fibre-reinforced plastic truss structures for satellite using braiding/resin transfer moulding process." *Proceedings of the Institution of Mechanical Engineers, Part L: Journal of Materials: Design and Application*, **221**(2), pp. 93–101.
17. Dahlsjo, O., 1992. "Antenna Research and Development at Ericsson." *IEEE Antennas and Propagation Magazine*, **34**(2), pp. 7–17.
18. Volakis, J. L., 1984. *Antenna Engineering Handbook* McGraw Hill Professional, New York.
19. Toi, Y., Harada, A., Tanaka, S., Amaoka, K., and Kikukawa, H., 2004. "Development of Affordable Composite Wing Structure." *Advanced Composite Materials*, **12**(4), pp. 321–329.
20. Bucci, A., and Mercurio, U., 1994. "CFRP stiffened panels under compression." *Composite Structures*, **27**(1-2), pp. 181 – 191 Special Issue Advances in Fiber Reinforced Composites Technology.
21. Mamalis, A., Manolakos, D., Ioannidis, M., and Papapostolou, D., 2006. "The static and dynamic axial collapse of CFRP square tubes: Finite element modelling." *Composite Structures*, **74**(2), pp. 213 – 225.
22. Ochoa, O. O., Roschke, P., and Bafrali, R., 1991. "Damage Tolerance of Composite Tubes Under Compressive Loading." *Journal of Composite Structures*, **19**(1), pp. 1–14.
23. Bathe, K. J., 1996. *Finite Element Procedures* Prentice Hall.
24. Riks, E., 1979. "An Incremental Approach to the Solution of Snapping and Buckling Problems." *International Journal of Solids and Structures*, **15**(7), pp. 529–551.
25. Analysis of Composite Materials with Abaqus. Slide Handouts from Abaqus Seminar.
26. Cook, R. D., Malkus, D. S., Plesha, M. E., and Witt, R. J., 2002. *Concepts and Applications of Finite Element Analysis* John Wiley and Sons.
27. Soller Composites. 1" Std material from <http://www.solarcomposites.com/composites/carbon%20fiber%20sleeves.html>.
28. Grafil 34-700 Material Properties. <http://www.grafil.com/images/newpdf/grafil/34-700.pdf>.
29. RS-36: 350°F Cure, Low Moisture Absorbing Toughened Epoxy Resin. http://www.tencate.com/TenCate/Aerospace_composites/documents/TCAC%20USA%20docs/TCAC%20USA%20Datasheets/DataSheet/RS-36_PB_DS_Web.pdf.

30. Standard Test Method for Compressive Properties of Polymer Matrix Composite Materials with Unsupported Gage Section by Shear Loading. Designation: D3410/D3410M - 03.
31. Standard Test Method for Shear Properties of Composite Materials by V-Notched Rail Shear Method. Designation: D7078/D7078M - 05.
32. Daniel, I. M., and Ishai, O., 2006. *Engineering Mechanics of Composite Materials*, second ed. Oxford University Press.
33. Strain Gage Installations with M-Bond 200 Adhesive. http://www.vishay.com/docs/11127/11127_b1.pdf Instruction Bulletin B-127-14.
34. The Three-Wire Quarter-Bridge Circuit. http://www.intertechnology.com/Vishay/pdfs/TechNotes_TechTips/TT-612.pdf Application Note TT-612.

Vita

Lieutenant Sabat graduated High School in 2004 and attended the United States Air Force Academy. Graduating in 2008 with a Bachelor of Science in Engineering Mechanics, he had a first assignment at AFIT. Lieutenant Sabat arrived at AFIT in August 2008. He completed the Masters in Aeronautical Engineering program in March 2010, and reported for duty at the Air Force Research Labs at Eglin AFB, FL.

REPORT DOCUMENTATION PAGE				Form Approved OMB No. 074-0188	
<p>The public reporting burden for this collection of information is estimated to average 1 hour per response, including the time for reviewing instructions, searching existing data sources, gathering and maintaining the data needed, and completing and reviewing the collection of information. Send comments regarding this burden estimate or any other aspect of the collection of information, including suggestions for reducing this burden to Department of Defense, Washington Headquarters Services, Directorate for Information Operations and Reports (0704-0188), 1215 Jefferson Davis Highway, Suite 1204, Arlington, VA 22202-4302. Respondents should be aware that notwithstanding any other provision of law, no person shall be subject to a penalty for failing to comply with a collection of information if it does not display a currently valid OMB control number.</p> <p>PLEASE DO NOT RETURN YOUR FORM TO THE ABOVE ADDRESS.</p>					
1. REPORT DATE March 25 2010		2. REPORT TYPE Master's Thesis		3. DATES COVERED (From – To) Sept 2008 – Mar 2010	
4. TITLE AND SUBTITLE Structural Response of Slotted Waveguide Antenna Stiffened Structure Components Under Compression				5a. CONTRACT NUMBER	
				5b. GRANT NUMBER	
				5c. PROGRAM ELEMENT NUMBER	
6. AUTHOR(S) Sabat Jr, Joseph W., 2LT, USAF				5d. PROJECT NUMBER	
				5e. TASK NUMBER	
				5f. WORK UNIT NUMBER	
7. PERFORMING ORGANIZATION NAMES(S) AND ADDRESS(S) Air Force Institute of Technology Graduate School of Engineering and Management (AFIT/ENY) 2950 Hobson Way, Building 640 WPAFB, OH 45433-8865				8. PERFORMING ORGANIZATION REPORT NUMBER AFIT/GAE/ENY/10-M19	
9. SPONSORING/MONITORING AGENCY NAME(S) AND ADDRESS(ES) AFRL/RBSA – Mr. Jim Tuss (James.Tuss@wpafb.af.mil) 2130 8 th St. Suite #1 WPAFB, OH 45433 (937) 986-5753				10. SPONSOR/MONITOR'S ACRONYM(S)	
				11. SPONSOR/MONITOR'S REPORT NUMBER(S)	
12. DISTRIBUTION/AVAILABILITY STATEMENT APPROVED FOR PUBLIC RELEASE; DISTRIBUTION UNLIMITED.					
13. SUPPLEMENTARY NOTES					
14. ABSTRACT <p>The Slotted Waveguide Antenna Stiffened Structure (SWASS) is an aircraft system that can provide the capabilities of a stiffened panel skin structure and a slotted waveguide radar antenna simultaneously. The system made from carbon fiber reinforced polymers is designed around a 10 GHz radar frequency in the X-band range and uses a WR-90 waveguide as a baseline for design. The system is designed for integration into fuselage or wing sections of intelligence, surveillance, and reconnaissance (ISR) aircraft and would increase the system performance through the availability of increased area and decreased system weight. Elemental parts of the SWASS structure were tested in compression after preliminary testing was completed for material characterization of a resin reinforced plain woven carbon fiber fabric made from Grafil 34-700 fibers and a Tencate RS-36 resin with a resin mass ratio of 30%. Testing included finite element stress and strain field characterization of seven single slot configurations, and results showed the longitudinal 90° slot was the best structural slot by about 30% in terms of maximum von Mises stress. Single waveguides were tested in the non-slotted configuration and a configuration including a five longitudinal slot array in one waveguide wall. Finite element results were compared with experimental results and showed good comparisons in all areas. The slot array was determined to have a decrease in nonlinear limit load of 8% from the finite element simulations and 12% from the experimental results. All waveguides showed the characteristics of local wall buckling as the initial failure mechanism and had significant buckling features before ultimate material failure occurred. Nonlinear limit load values were only slightly lower than linear bifurcation values, by less than 1% for both the slotted and non-slotted configurations. The imperfections from laboratory preparation caused a drop in the predicted limit load by about 30% showing the need for extreme care in advanced composite construction. Overall, results proved meaningful and the degradation in compressive performance due to the slot array is acceptable and promising. Future research is encouraged in the form of material tailoring, panel integration, and system optimization among others.</p>					
15. SUBJECT TERMS slotted waveguides; SWASS ; composite tubes; compression; bifurcation; Riks;					
16. SECURITY CLASSIFICATION OF:			17. LIMITATION OF ABSTRACT UU	18. NUMBER OF PAGES 170	19a. NAME OF RESPONSIBLE PERSON Dr. Anthony Palazotto, AFIT/ENY
a. REPORT U	b. ABSTRACT U	c. THIS PAGE U			19b. TELEPHONE NUMBER (Include area code) (937) 255-3636 ext 4599